Josephson Inductance Thermometry in Resonantly-Coupled Van-der-Waals Heterostructures

Thesis by
Raj Michael Katti

In Partial Fulfillment of the Requirements for the
Degree of
Doctor of Philosophy

CALIFORNIA INSTITUTE OF TECHNOLOGY
Pasadena, California

2022
Defended November 4, 2021

Raj Michael Katti
ORCID: 0000-0002-7942-0504

ACKNOWLEDGEMENTS

I would like to thank the following people who supported me in the course of this PhD work:

- To my advisor Michael Roukes, for his dedication to the pursuit of elegance in experimental design and the presentation of technical ideas.
- To Keith Schwab, for his mentorship and friendship. May this not be the last collaboration!
- To Stevan Nadj-Perge, for his oversight of much of this project and determination to see it to completion.
- To Olli Saira, Matt Matheny, Ewa Rej, Azadeh Ansari, HP Arora, for their technical expertise, guidance, and/or partnership.
- To my parents Romney and Michele, for preparing me for the road ahead.
- To my sister Alyna, for her, alternately, support and sarcasm.
- To Maria Spiropulu and Tom Tombrello, for their steady guidance through times of uncertainty.

And to all those who gave their friendship and support:

M. Horton, T. Hemo, B. Lieber, E. Patterson, J. Ziac, K. Zemlianova, A. Bouman, A. Bouman, T. Shankar, S. Reese, L. Card, A. Blachowicz, A. Lui, L. Cleary, I. Saberi, B. Zhang, K. Mauser, L. Dajose, J. Strohm, J. Denly, A. Doran, M. Von Korpff, L. Risse, S. Kang, J. Cham, Z. Abbott, and M. Boutilier.

ABSTRACT

A promising strategy for pushing single-shot energy-resolving detection to the level of individual microwave photons, thermal phonons, and single k_BT heat pulses is the development of thermal detectors with miniscule heat capacities. Graphene, with its vanishing heat capacity and diminished electron-phonon coupling at cryogenic temperatures, is an enticing material platform for achieving heat capacities at the level of single-k_B in solid-state systems at dilution refrigerator temperatures. Key to the design and operation of a thermal detector is the readout method employed to monitor the temperature of the thermal element. However, to date, existing thermometry methods for Van-der-Waals materials have typically been slow and ill-suited for single-shot calorimetry, limited either by long averaging times, sweep repetition rates, or resetting times of switched Josephson junctions.

This dissertation presents Josephson inductance thermometry, a method we have demonstrated for probing the electron temperature of Van-der-Waals materials at milli-Kelvin temperatures. The technique relies upon the inductive loading of a superconducting resonator by a graphene-based Josephson junction, in which increases in electron temperature of the graphene flake are transduced to shifts of the resonant frequency. This technique brings with it many of the benefits of resonant readout, such as fast response times, ease of frequency-division multiplexing, and operation at the lowest temperatures available to a dilution refrigerator where the device parameter regime yields the greatest detector sensitivities. Such a device design is well-suited, for example, to the serving as the fundamental pixel architecture of next-generation dark matter searches.

This thesis derives all thermal detector performance metrics and fundamental noise sources from first principles and provides a pedagogical introduction to the superconducting phenomena and low-temperature physics exploited by the detector. Subsequently, a thorough discussion is presented of the device architecture, fabrication procedures, measurement chain, physical characterization via carrier density sweeps, physical characterization via Joule heat sweeps, and noise measurement characterization. It is our hope that researchers interested in pushing the limits of ultrasensitive thermal detectors and calorimetry can use this thesis to delve into details of Josephson inductance thermometry as well as the field of cryogenic thermal detection broadly.

PUBLISHED CONTENT AND CONTRIBUTIONS

[1] Raj Katti et al. *Broadband Radiation Sensor Based On A Resonantly-Coupled Graphene SNS Junction*. US Patent, in review with USPTO. [*R.M.K. conceived of patent. R.M.K. contributed to writing patent application.*]

[2] Raj Katti et al. "Hot Carrier Thermalization and Josephson Inductance Thermometry in a Graphene-based Microwave Circuit". In: (2021, in review). [*R.M.K. performed measurements and physical characterization. R.M.K performed data analysis. R.M.K. contributed to writing and editing the manuscript.*]

[3] Olli-Pentti Saira et al. "Nonequilibrium thermodynamics of erasure with superconducting flux logic". In: *Phys. Rev. Research* 2 (1 Mar. 2020). [*R.M.K. assisted in measurement and physical characterization.*], p. 013249. URL: https://link.aps.org/doi/10.1103/PhysRevResearch.2.013249.

TABLE OF CONTENTS

Acknowledgements . . . iii
Abstract . . . iv
Published Content and Contributions . . . v
Table of Contents . . . vi
List of Illustrations . . . viii
Chapter I: Introduction . . . 1
Chapter II: Thermal Detectors: Physical Model and Fundamental Performance Limits . . . 4
2.1 Introduction . . . 4
2.2 Linear Model of a Thermal Detector . . . 4
2.3 Fluctuation Dissipation Theorem . . . 8
2.4 Fundamental Noise Sources and Detection Limits . . . 20
2.5 Conclusion . . . 31
Chapter III: Graphene-based Superconducting Detectors Background . . . 33
3.1 Principles of Superconductor-Normal-Superconductor Junctions . . . 33
3.2 Graphene Background . . . 43
3.3 Resistively- and Capacitively-Shunted Junction (RCSJ) Model . . . 49
3.4 Cryogenic Graphene Thermal Detectors . . . 51
3.5 Applications of Ultrasensitive Calorimetry: Measurement of the Landauer Limit . . . 63
3.6 Conclusion . . . 67
Chapter IV: Measurement Setup . . . 69
4.1 Principles of Dilution Refrigeration . . . 69
4.2 BlueFors LD-400 Dilution Refrigerator . . . 78
4.3 S_{21} Measurement Circuit . . . 81
4.4 Amplifier Chain . . . 84
4.5 Sample Box . . . 86
4.6 Metal Powder Filters . . . 90
4.7 Conclusion . . . 91
Chapter V: Nanofabrication . . . 93
5.1 Fabrication Procedure . . . 93
5.2 Graphene/Resonator Device . . . 100
5.3 Transmission Line Resonator . . . 103
5.4 Conclusion . . . 110
Chapter VI: Device Characterization . . . 111
6.1 Benefits of Resonantly-Coupled Graphene Device . . . 111
6.2 Resonance vs. Backgate Voltage . . . 114
6.3 Heater Port Resistance Measurement . . . 118
6.4 Impedance Model . . . 124

6.5 Discussion of Extracted Parameters from Resonance Fits and RSJ Model . . . 127
6.6 Conclusion . . . 129
Chapter VII: Heating Measurements . . . 130
7.1 Introduction . . . 130
7.2 Electron-Phonon Coupling in Normal Metals . . . 130
7.3 Electron-Phonon Coupling in Monolayer Graphene . . . 135
7.4 Heater Measurements . . . 137
7.5 Power/Temperature Scaling . . . 141
7.6 Conclusion . . . 143
Chapter VIII: Noise Equivalent Power . . . 144
8.1 Introduction . . . 144
8.2 Theory . . . 144
8.3 Experimental Design . . . 145
8.4 Sideband Spectrum . . . 148
8.5 Sideband Scaling . . . 148
8.6 **NEP** vs. $\mathbf{P_{heater}}$ . . . 148
8.7 **NEP** vs. Carrier Frequency and Carrier Power . . . 148
8.8 Detection Limits . . . 150
8.9 Conclusion . . . 150
Chapter IX: Summary . . . 151

LIST OF ILLUSTRATIONS

Number *Page*

2.1 **Linear Model of a Thermal Detector.** A device schematic (left) and equivalent circuit model (right) of a thermal detector. Shown are physical parameters heat capacity C_{th} and thermal conductance G_{th}, applied heat power $P(t)$, bath temperature T_0, and temperature rise ΔT. 6

2.2 **Thermal Response of a Single Absorption Event.** In response to the absorption of energy quantum δE, the temperature of a thermal detector increases by $\Delta T = \frac{\delta E}{C_{th}}$ and subsequently decays to bath temperature T_0 over a time $\tau_{th} = \frac{C_{th}}{G_{th}}$. 7

2.3 **Emission and Absorption Rates.** Two energy levels $|m\rangle$ and $|n\rangle$ with energies $E_m > E_m$ are shown. Absorption of energy quanta (red) allows transitions from $|n\rangle$ to $|m\rangle$, while emission of energy quanta (blue) allows the reverse transitions from $|m\rangle$ to $|n\rangle$. In the presence of a thermal bath, the ratio of the emission and absorption rates is set by the ratio of Boltzmann factors $\rho_n = e^{-E_n/k_BT}/\mathcal{Z}$. 17

2.4 **Signal and Noise at the *Output* of the Measurement Chain.** Signal $P(f)$ and noise spectral densities $NEP_{th}(f)$ and $NEP_{Johnson}(f)$ at the measurement output. Both $P(f)$ and $NEP_{th}(f)$ experience a one-pole roll off above the thermal cut off $\omega_{th} = \frac{1}{\tau_{th}}$, producing a signal-to-noise ratio SNR_{th} which does not roll-off above the thermal cut off. By contrast, $NEP_{Johnson}$ is flat at the output, so the signal-to-noise ratio $SNR_{Johnson}$ *does* roll off above ω_{th}. 29

3.1 **Quasiparticle Energy Bands for Normalconducting and Superconducting States.** (left) In the normal state, the superconducting gap energy vanishes ($\Delta = 0$) and the BdG equations decouple into two different energy bands. The concavity of the electron band (red) implies that electrons have a positive group velocity $\frac{\partial\omega}{\partial k} \geq 0$, whereas the hole band (blue) implies that holes have a negative group velocity $\frac{\partial\omega}{\partial k} \leq 0$. (right) In the superconducting state ($\Delta \neq 0$), the presence of the superconducting gap Δ couples electron and holes to produce quasiparticles, where a quasiparticle of a given k-vector is composed of a linear combination of an electron and hole of the same k-vector. The relative magnitude of the electron and hole contributions depend on the proximity of k to k_F. In the case of the $E > 0$ band, excitations deep within the Fermi-sea are hole-type, excitations far above the Fermi-sea are electron-type, and excitations close to the Fermi sea are of mixed character. This can also be understood from the two quasiparticle energy bands, where the sign of the group velocity of the quasiparticle changes as k sweeps across k_F, indicating a cross-over from hole-type to electron type (blue trace) or vice-versa (red trace). 36

3.2 **Andreev Reflection**. **a.** Scattering Processes at a Superconductor-Normalconductor Interface, with permission from Blonder, Tinkham, and Klapwijk [15]. In the case of an electron in a normal metal *(0)* incident upon a superconductor, the following processes are considered. Quasiparticle transmission into the left branch *(2)* or right branch *(4)*. Reflection as a normal electron *(5)* or *(6)* Andreev-reflection as a hole **b.** Andreev Reflection coefficients as a function of incident electron energy E (with permission from Heikkilä [49]). For an incident electron, $|r_{he}|^2$ corresponds to the probability of Andreev electron-hole reflection, while t_+ corresponds to the transmission into the superconductor as a quariparticle of equal energy. We see that for electron energies below the superconducting gap $E < \Delta$ only electron-hole reflection may occur. Above the gap, the probability of electron-hole reflection decreases and quasiparticle transmission increases with energy. **c.** Andreev Bound State Energy E^{ABS} vs. the phase difference between the superconductors ϕ (with permission from Heikkilä [49]). For finite transmission coefficients $\tau < 1$, the bound state energy is 2π-periodic, while for perfect transmission it is 4π-periodic. 39

3.3 **Thermal Excitations of a Fermi Electron Gas**. (**left**) Fermi-Dirac Distribution. At $T = 0$, the Fermi-Dirac distribution is brick-wall occupation function in which all electrons are at their lowest possible energies prescribed by Pauli repulsion. As the temperature is increased to a finite T, a smearing of the distribution occurs over a width k_BT. In other words, only those electrons with in a k_BT of the Fermi energy are thermal excited. (**right**) The Fermi Sea. This diagram is meant to demonstrate that only a small fraction of the total electrons in the Fermi sea are thermally excited, accounting for a suppression of C_{th} by a factor of $\frac{T}{T_F}$ relative to the classical case. . . 43

3.4 **Heat Capacity C_{th} Scaling with Temperature in a Suspended Nanostructure, from Roukes [96]**. In the case of an electron gas on a suspended nanostructure with galvanic contact via superconducting leads, Roukes considered the relative contributions to the total heat capacity. At low temperatures, the electronic heat capacity, which scales as $\sim T$ typically dominates over the other sources of heat capacity, which possess a stronger temperature scaling. Due to the energy gap between the ground state and the excited states, the heat capacity of the superconducting leads are exponentially suppressed as $\sim e^{-\Delta/k_B T}$. Since the phononic contributions to the heat capacity go as the dimensionality of the phonons, with freeze-out occurring when the phonon wavelength exceeds the device size. 45

3.5 **Projected Thermal Detector Specifications for a graphene 2DEG, from Walsh et al. [115].** (**left**) C_{th} vs. Flake Temperature for a graphene 2DEG. For temperatures below 100 mK, it should be possible to achieve heat capacities below $10k_B$, where the C_{th} can be further reduced by shrinking the flake area A, reducing the carrier density n_A, or lowering the flake temperature T. (**right**) Energy resolution vs. Flake Temperature for a graphene 2DEG. It is assumed that the energy resolution of graphane 2DEG operated as a thermal detector is limited by a measurement bandwidth set by the thermal roll-off τ_{th}. 49

3.6 **Resistive Readout of Dual-Bilayer Gated Graphene Flake Temperature at 5K, from Yan et al. [123]**. **a.** A bilayer graphene sample is gated with a global top gate and bottom gate. **b.** A heat map of the resistance is shown as function of top gate and bottom gate. **c.** The temperature-dependent resistance $R(T)$ is shown down to 5K. 52

3.7 **Graphene Josephson Junction Switching Detector, from Lee et al. [69] a.** SEM image of a graphene Josephson Junction. The graphene flake is the long, thin the center of the image surrounded by four contacts and a gate to control carrier density. The contacts are composed of edge-contacted NbN superconductors, where the contacts at the top and bottom of the image comprise the Josephson junction leads, and the contacts at the left and right of the image comprise the heater leads. **b.** IV curve of the graphene Josephson Junction. The zero-voltage supercurrent region has a maximum value $Is(T)$ of the switching current which demonstrates a clear temperature dependence. There is a clear hysteresis in the IV curve between the positive and negative bias due the positive-to-negative I_{bias} sweep direction, where Joule heating of the flake in the normal regime suppresses the retrapping current I_r relative to the switching current I_s. **c.** Temperature dependence of the average switching current. Clearly, the switching current exhibits a temperature dependence down to 200 mK, which allows operation of the threshold detector down to these temperatures. **d.** Switching probability of I_s. Variance of the switching current $\sigma^2_{I_S}$ about the mean value $\langle I_s \rangle$ can be explained in the RCSJ model either by thermal excitation or macroscopic quantum tunnelling. 54

3.8 **A Brief Introduction to MKIDs (borrowed with permission from Day et al. [28]). a. Detection Principle of an MKID.** Pair breaking radiation ($h\nu > 2\Delta$) breaks Cooper pairs, alters the surface inductance of the superconducting film, and shifts the resonant frequency of the resonantor. **b. Resonant Frequency Shift.** Accompanying the absorption of radiation, the resonant frequency and quality factor shift. This shift can be monitored by the scattering of a microwave tone at a frequency within the linewidth of the resonance. Tones outside the linewidth will not be scattered. **c. Top-down Image of Superconducting Resonator.** Example of a CPW-style quarter-wavelength resonator patterned from superconducting aluminum on a sapphire substrate. **d. Absorption of an X-ray photon.** Phase the transmitted scattered signal upon absorption of an X-ray photon. . . . 60

3.9 **Resonantly-coupled Graphene Josephson Junction Qubits (from Wang et al. [117] and Schmidt et al. [101]). (left)** In their graphene JJ/microwave circuit, [117] show resonance tuning over a range of 6-12 GHz and p-n-p Fabry-Perot type oscillations with an effective Fabry-Perot cavity length of $L_c = 110$nm **(right)** Schmidt et al. [101] show resonance tuning over a range of 6.8-8.2 GHz and Fabry-Perot type oscillations in a cavity length of $L_c = 390$nm. 61

3.10 **Bolometer Operating at the Threshold of QCD, from Kokkoniemi et al. [63]. a.** Examples of resonance position at different backgate voltages and applied powers. **b.** Differential thermal conductance G and measured NEP as a function of bath temperature T_b. **c.** Time trace showing device response for quick turn-on and turn-off of applied power. Exponential fits determine rising and falling time constants. 62

3.11 **Modern Landauer Erasure Experiments a.** Bistable potential realized by the laser trap, from Bérut et al. [13]. The erasure protocol allows the silica bead to start initially in either the left or the right well, but ensures that at the end of the procedure, the bead will only be on the right well. **b.** Schematic of a calorimetric measurement of the heat dissipation of a logical element. Here, the logic element takes the form of a nanoelectomechanical system (NEMS), though any controllable logic element will suffice. The logical element is integrated into a suspended low-C_{th} island, where local thermometry is performed to monitor the island's temperature. If $\Delta Q = k_B T \log(2)$ is dissipated locally in a control protocol upon the logic element, the suspended structure will have sufficient energy resolution and measurement bandwidth to resolve the associated temperature increase.**c** Impedance diagram of flux qubit, from Saira et al. [99] (along with d,e). Back-to-back Josephson junctions are shown, along with flux bias lines for controlling barrier height and tilt. **d** Activation rate vs. stage temperature shows crossover from thermal activation to macroscopic quantum tunneling (MQT) at $T_{mxc} \approx 100$ mK. **(e)** Probability ratios of trajectory-level work W for forward and reverse processes follows Crook's relation [27], as realized by a superconducting flux logic platform. 66

4.1 **Helium-4 Liquid-Gas Phase Coexistence**. A vat of helium-4 held at temperature T will have coexisting liquid and gas phases. The gas phase has an equilibrium vapour pressure P_{vap} and entropy S_{gas} and the liquid has entropy S_{liquid}. A He-4 atom can transition from the liquid to the gas phase upon absorption of latent heat $L = T(S_{gas} - S_{liquid})$. 71

4.2 **Dilution Cooling in Mixing Chamber**. Schematic shows the flow of helium-3 in the mixing chamber of a dilution refrigerator, where the blue circles refer to He-3 atoms and the gray region refers to the inert superfluid He-4 background. He-3 is pumped into the chamber to the low-density He-3 rich phase. As each He-3 atom crosses into the He-3/He-4 phase, it takes up a heat ΔH from its surroundings, producing a cooling power. He-3 is then pumped out of the mixing chamber to be re-circulated and pumped back into the mixing chamber. Dilution cooling can achieve temperatures below $T_{mxc} = 10$ mK due to the finite (6.6%) concentration of He-3 in the He-3/He-4 phase. 73

4.3 **Phase Diagram of Helium-3/Helium-4 Mixture, from [92]**. Phase diagram is shown as a function of temperature (y-axis) and He-3 mole fraction (x-axis). Below $T = 870$ mK, the hatched "two-phase region" is not physically accessible and the mixture has two distinct accessible phases along the phase-separation line, with different He-3 mole fractions x. One phase is He-3 rich ($x > 70\%$) and approaches $x = 100\%$ as $T \to 0$ K. The other ($x < 70\%$) is a dilute mixture of He-3 in superfluid He-4 and approaches $x = 6.6\%$ as $T \to 0$ K. This finite concentration of helium-3 is the source of the cooling power of a dilution refrigerator. Diagram taken from [92]. 75

4.4 **LD400 Dilution Refrigerator Insert, borrowed with permission from BlueFors Oy.** Image showing the cryogenic plates of an LD400 dilution refrigerator. Descending plates achieve lower temperatures with the lowest mixing chamber plate achieving the minimum temperatures of the dilution refrigerator. At the top of the image is shown the coldhead of the pulse-tube used for pre-cooling the system without liquid He-4. 79

4.5 S_{21}**.** a. Gas Handling System. b. High-Pressure Lines and Compressor c. Water Chiller d. Control Unit e. Cryostat 80

4.6 S_{21} **Circuit Diagram.** The circuit diagram shows both the S_{21} readout of the resonance feature and the application and readout of P_{heater}. In the S_{21} measurement, a signal is sourced from the PicoVNA2 vector network analyzer (VNA) and passes through a series of attenuators down to the resonator/graphene device held at T_{mxc}. The transmitted portion of the signal is amplified by an amplification chain with a first-stage 4K LNA and read out by the VNA. Application of P_{heater} proceeds by sourcing a current I generated by a voltage sourced by the Agilent 33221A AWG and dropped over a 1 MΩ ballast resistor. After passing through a two stages of filters, the sourced current flows through the normal resistance R_{heater} of the heater port of the graphene sample and dissipates Joule heat power in the flake. The voltage drop V across graphene heater is amplified by a SR560 preamp and read out by a 32201A digital multimeter (DMM). In this way, the $P_{heater} = I \times V$ delivered to the graphene flake is measured in a 4-wire measurement. 83

4.7 S_{21}**. a.** DL 1201 Low Noise Voltage Preamp, used for amplifying output of heater port. **b.** Model SR844 RF Lock-In Amplifier. **c.** Breakout box used for sending signals on twisted-pair lines. **d.** +44 dB Narda-MITEQ AU-1578 Room Temperature Amplifier **e.** +15 dB Narda-MITEQ AFS1 and +20 dB Mini-Circuits ZX60-83LN12+ Room Temperature Amplifiers. **f.** PicoVNA 106, 300 kHz– 6 GHz Vector Network Analyzer. 85

4.8 S_{21} **Room Temperature Amplifier Cascaded Gain Profile.** For an input -100 dBm signal, the gain (S_{21} mag) of the thee room temperature amplifiers is approximately 80 dB over 500 MHz- 1 GHz. 86

4.9 **Sample Holder.** Here we have a view of the inside of the sample holder, with two chips adhered to the holder with wirebonds to the lines responsible for carrying DC or RF signals to the sample. At the bottom, 16 quasi-DC filtered twisted pair lines are available to wirebond to the samples. From the sides and top, 6 RF lines are available for wirebonding, here shown as coplanar waveguides with the central conductor clearly separated from the aluminum ground plane and 6 connectors visible. 87

4.10 **Sample Box Photos (courtesy of Olli Saira). a.** CAD diagram of sample box. **b.** DC twisted pair lines prior to immersion in copper powder/Stycast mixture. **c.** Sample box coplanar waveguide grooves. **d.** Coplanar waveguide grooves in opposite plate, with Eccosorb regions. **e.** Sample box installed on mixing chamber stage. **f.** Installed sample box with magnetic shield and thermalizing copper sheet 89

5.1 **Patterning the NbTiN Resonator. a)** A cross-section schematic of the NbTiN film sputtered on a SiO_2 chip is shown. **b)** To form the etch mask for patterning the NbTiN resonator, an electron beam resist is spin, baked, patterned in an EBPG and developed. **c)** A reactive ion etch etches away that portion of the NbTiN which is not covered by the electron beam resist mask. **d)** The resist is removed according to standard procedures, leaving behind the patterned NbTiN resonator, shown in cross section. 94

5.2 **Stamping Procedure. a)** The stamping procedure is performed using a glass slide covered by a silicone elastomer (PDMS) and adhesive polycarbonate (PC), **b)** The glass slide and polymers are lowered until the PC layer contacts the hexagonal boron nitride (hBn) layer. **c)** With the PC layer adhered to the hBn layer, the glass slide is raised, lifting the hBn layer off of the substrate. **d)** This procedure is repeated on all layers of the Van-der-Waals material stack, where Van-der-Waals forces create a sufficient attraction between the layers to allow stacking without any additional adhesive beyond the PC layer. The final material stack is shown and the SiO_2 wafer, in contrast to the SiO_2 substrate denoted previously, refers to the SiO_2 NbTiN chip upon which the Van-der-Waals stack will be stamped. **e)** The full stack is lowered onto the SiO_2 NbTiN chip for final placement. **f)** The glass slide is heated to melt the PC layer and lifted away, leaving behind the material stack covered in a layer of molten PC. The material stack is now ready to be contacted with metallic electrodes. 96

5.3 **Deposition of Aluminum Electrodes. a**. From the prior stamping step, the Van-der-Waals material stack is stamped on the NbTiN resonator chip. **b**. A PMMA mask is spun and baked on the chip. The mask will be used both as an etch mask and for a liftoff procedure to define the metallic contacts. **c**. Using electron beam lithography, the electrode pattern is inscribed into the PMMA and developed in a standard PMMA developer, removing the PMMA mask in those regions of the chip where aluminum contacts will be placed. **d**. An RIE CHF_3/O_2 etch is performed to etch into the Van-der-Waals stack and reveal the 1D edge of the graphene flake, in order to make a low-resistance Ohmic contact. **e**. Aluminum is evaporated onto the chip using an electron beam evaporator free of magnetic materials which may inhibit superconductivity. A thin titanium layer can be included to promote adhesion between the evaporated aluminum and substrate. **f**. The PMMA mask is removed in a standard liftoff procedure, leaving behind the aluminum electrodes patterned by the etch mask. The nanofabrication procedure is now complete and the sample is ready for measurement. 97

5.4 **Optical Image of Patterned Electrodes in a PMMA Mask on a Graphene-based Material Stack.** Visible is a developed PMMA etch mask with an inscribed electrode pattern. The aqua-colored region is the bottom hBn, the yellow region within the aqua region is the top hBn, and the darkened region overlapping both colored regions is the graphite backgate. Brown finger-like projections correspond to electrode designs patterned into the PMMA etch mask. 99

5.5 Electrical circuit schematic. A resonator designed for low characteristic impedance made of Niobium Titanium Nitride (NbTiN) is coupled to the external microwave line via coupling capacitor and terminated by the S-G-S junction. Characterization of the device is performed by sending in a microwave tone and measuring transmission coefficient S_{21}. Changes in the junction's electrical impedance shift the resonant frequency of the NbTiN resonator. A dedicated heater port allows application of Joule heat to the graphene flake, thereby electrically isolating the heating and readout ports while maintaining a thermal link between them. The resistance between heater port and the ground is ∼1 kΩ. We model the S-G-S junction electrically as the parallel sum of a dissipationless branch of inductance $L_J = \frac{\Phi_0}{2\pi I_c}$ and a dissipative branch of resistance R_{SG}. . . . 100

5.6 **Optical Image of Graphene Flake.** Optical image showing the graphene flake encapsulated in hexagonal boron nitride (blue-green) and contacted by aluminum electrodes (light blue). Two ground wires span the entire length of the flake. The top contact is placed in close proximity to the ground wires to form gJJ. The bottom contact placed far from the ground electrodes and can be used to apply Joule heating via heater current (I_{heater}). The inset shows the partial cross-section across the gJJ. Encapsulated graphene is contacted at the edges to form the superconductor-graphene-superconductor (S-G-S) junction. The metallic contacts consist of superconducting Al and a thin (5 nm) adhesion layer of titanium (not shown). Tuning the global carrier density in the graphene flake is achieved by applying a DC voltage V_{BG} to a graphite backgate. 102

5.7 **Unit Cell of Transmission Line, from M. Pozar [75]** 104

5.8 **Van-der-Waals Stack and NbTiN Resonator, borrowed with permission from Arora [4].** 107

5.9 **Impedance Model** The electrical impedance model of the resonator-graphene device consists of the graphene Josephson junction in the RSJ model, a NbTiN transmission line resonator characterized by parameters in Table 5.1, a coupling capacitor C_c, and 50 Ω microwave ports. 108

6.1 **Schematic of Frequency-Domain Multiplexed Graphene Detectors**. Here we show a schematic for frequency-domain multiplexed readout of graphene detectors. As indicated by the differing lengths of transmission line resonators, each resonator has a different resonant frequency, with a frequency profile indicated in the inset. Since the resonances are separated in frequency space by more than a linewidth, a tone sent down the feedline initialized within the linewidth of a given resonant frequency will be loaded only by that resonator and will pass by all others. Thus, an array of detectors can load the same feedline and be read out with a single, wideband cryogenic amplifier. 113

6.2 **a**, Representative $|S_{21}|$ data and fits for electron and hole doping. Color and labels denote backgate voltage V_{BG}. Arrows show the direction of resonant frequency shifts as V_{BG} is swept from positive voltage (electron doped) to negative voltage (hole doped) through charge-neutrality. Green arrow shows the resonant frequency approaching 500 MHz as electron-doping decreases to charge neutrality. Blue arrow shows that the resonant frequency increases away from 500 MHz as hole-doping increases. 116

6.3 **c**, $|S_{21}|$ vs. V_{BG} shows the resonant frequency of the device as a function of electron density as tuned by the back gate. Near the charge neutrality point (CNP; $V_{CNP} = -0.3$ V), the gJJ maximally loads the resonator and consequently minimizes the value of resonant frequency. Far from the CNP, the gJJ acts as a low-inductance termination to the resonator and the resonant frequency approaches its maximum. On the hole-side ($V_{bg} < V_{CNP}$), Fabry-Perot type oscillations are visible due to formation of the regions of different doping in the graphene (hole doping; p-type) and in vicinity of contacts (electron doping n-type)[101]. 117

6.4 **Fermi Level Shift At Metal/Graphene Interface, from Giovannetti et al. [45]**. Plotted is the Fermi level shift as a function of displacement between surfaces for different graphene/metal interfaces. A negative Fermi level shift corresponds to n-doping of the graphene, and a positive Fermi level shift corresponds to p-doping of the graphene. For the entire range of displacements, aluminum is expected to n-dope the graphene flake. Figure taken from [45] 118

6.5 **Heater Port Resistance**. Measured resistance of the heater port (via the 4-wire measurement) is shown as a function of the backgate voltage (proxy for carrier density). The charge neutrality point exists at approximately $V_{BG} = 0.3$ V. The resistance of the hole side is larger than that of the electron side, in agreement with a non-negligible contact resistance resulting from p-n junctions on the hole-side. . . . 121

6.6 **(Left)** Hole side I_c vs. V_{BG}. Blue trace is hole side I_c data for $T_{mxc} = 160$ mK. Red trace is the slowly-varying background as fit to a 7^{th}-order polynomial. **(Middle)** Background-subtracted ΔI_c vs. k_F. ΔI_c is obtained by subtracting the two traces in 6.6(left). **(Right)** Power spectral density of ΔI_c. The large peak is consistent with an effective Fabry-Perot cavity length of $L_{cav} = 361.51$ nm. 123

6.7 **Impedance Model** The electrical impedance model of the resonator-graphene device consists of the graphene Josephson junction in the RSJ model, a NbTiN transmission line resonator characterized by parameters in Table 5.1, a coupling capacitor C_c, and 50 Ω microwave ports. 124

6.8 **Resonance Fits and Extracted Parameters. Top Left**, f_0 as a function of V_{BG} for representative $T_{mxc} = 160, 210, 260, 310, 360, 410, 460$ mK. Extracted resonant frequency f_0 as a function of V_{BG} shows a characteristic lineshape consistent with Fig 1c. As T_{mxc} increases, f_0 decreases for all backgate voltages. Near charge neutrality and for higher temperatures, the device becomes undercoupled to such an extent that fitting is unreliable. Fit parameters in these regions are not included in the plots. **Top Right**, Q_i as a function of V_{BG} and T_{mxc}. **Bottom Row**, RSJ model parameters I_c (**Bottom Left**), and R_{SG} (**Bottom Right**) as a function of V_{BG} and T_{mxc}. I_c and R_{SG} are determined using a numerical impedance model of the resonator/gJJ device with resonance parameters (f_0, Q_i) as inputs. 125

6.9 **Extracted Parameters from Resonance Fits and Impedance Model** **a.** Q_i vs. V_{BG}. The internal quality factor Q_i is extracted from the S_{21} fit function. **b.** Q_i/Q_c vs. V_{BG}. Ratio of internal quality factor Q_i and coupling quality factor Q_c (also extracted from the S_{21} fit function) shows that the device is in the undercoupled limit for all backgate voltages. **c.** $\omega L_J/R_{SG}$ vs. V_{BG}. Ratio of the inductive branch impedance to resistive branch impedance in the RSJ model. **d.** $\tau = Q_0/\omega_i$ vs. V_{BG}. The resonator time constant τ is expected to set the system time constant for all measured backgate voltages and temperatures. **e.** L_J vs. V_{BG}. The Josephson inductance $L_J = \frac{\Phi_0}{2\pi I_c}$. **f.** f_0 vs. V_{BG}. The red line corresponds to the projected unloaded ($L_J = 0\,\mathrm{nH}$) resonance frequency. Δf corresponds to the loaded ($L_J \neq 0\,\mathrm{nH}$) resonance frequency at $T_{mxc} = 160\,\mathrm{mK}$. δf corresponds to further shift in the resonance frequency due to the increase in flake temperature. 126

6.10 **(left)** I_c vs. T. An example fit of I_c vs. T for $V_{BG} = -2.01$ V with extracted fit parameters $I_c(0)$ and Δ. **(center)** Fit parameter $I_c(0)$ vs. V_{BG}. $I_c(0)$ fit parameter is shown for both electron and hole doping. **(right)** Fit parameter Δ vs. V_{BG}. A coarse estimate of induced gap $\Delta \approx 80\,\mu\mathrm{V}$. Fine features are discussed in the text. 128

7.1 **Heat Transfer via Electron-Phonon Coupling, from Wellstood, Urbina, and Clarke [120].** (**Left**) In a standard model of thermal transport in solid-state systems, heat flow typically has two dominant sources of thermal resistance. Electron-phonon thermal resistance R_{ep} is typically limited by the slow rate of scattering between electrons and thermal phonons. The Kapitza boundary resistance R_K between thermal phonons of the solid-state system and the substrate arises from the acoustic impedance mismatch of the solid-state lattice and the environment [93]. At sub-500 mK temperatures, it is often the case that $R_{ep} > R_K$, which allows the electron temperature to rise above the phonon temperature and yield 'hot-electron' effects. (**Right**) Two key scattering processes occur between electrons and thermal phonons, as indicated by the two energy- and momentum-conserving Feynman diagrams. In one, an electron emits a thermal phonon and relaxes to lower energy. In the other, electrons can absorb a thermal phonon and be excited to a higher energy. 131

7.2 **Experimental Demonstration of the Hot Electron Effect, from Roukes et al. [97]. (Left)** Example of the dependence of copper film resistance on temperature, with resistance saturating below ~50 K. **(Right)** Electron Temperature vs. Applied Bias Voltage. The power law dependence is in agreement with electron-phonon scattering calculations for 3D electrons and phonons in metal films under the deformation potential approximation. Inset shows that the electron temperature is elevated relative to the phonon temperature up to approximately the $R_{ep} \sim R_K$ crossover. 134

7.3 **Measurement Circuit for Johnson Noise Thermometry of Monolayer Graphene, from Fong and Schwab [39].** Circuit diagram shows the impedance matched $\sim$ 30 kΩ to the 50Ω measurement circuit and HEMT via the LC-tank circuit. Additional plots show measurements of the circuit, including the noise PSD which peaks at approximately 1.16 GHz. 136

7.4 **Thermal Measurements of Monolayer Graphene, from Fong and Schwab [39]. (left)** Integrated Noise Power vs. Temperature. Dependence is agreement with the Johnson Noise Formula. The inset plot shows that the measured precision of the temperature is in agreement with the Dicke radiometer formula. **(center)** Thermal conductance G_{th} vs. Temperature exhibits a temperature dependence consistent with $P \propto T_e^4 - T_{ph}^4$. Inset shows that a heater current applied at ω yields a temperature modulation at 2ω. **(right)** Electron temperature vs. Applied Joule heat power. 137

7.5 **Electron-side and Hole-side Heating and Calibration. a-c,** Electron-side ($V_{BG} = 1.1\,V$) and **f-h,** hole-side ($V_{BG} = -1.8\,V$) $|S_{21}(f)|$ vs. I_{heater} for three representative mixing stage temperatures **a, f)** $T_{mxc} = 170\,mK$ **b, g)** $T_{mxc} = 280\,mK$ **c, h)** $T_{mxc} = 400\,mK$. Applying a DC heater current I_{heater} to the designated heater port decreases the resonant frequency of the device. As expected, the shifts are symmetric with respect to the polarity of I_{heater}. **d,** Electron-side and **i,** hole-side I_c as a function of I_{heater}. Fitting **a-c** and **f-h** allows extraction of resonance parameters (f_0, Q_i) which are subsequently used to estimate the junction parameters (I_c, R_{SG}) via a numerical impedance model). I_c is plotted as a function of I_{heater} for several mixing chamber temperatures T_{mxc} (color). The dashed line at $I_{heater} = 0\,nA$ corresponds to the data cut plotted in **e** and **j**. **e,** Electron-side and **j,** hole-side calibration curve, the unheated I_c as a function of T_{mxc}. Since I_c monotonically decreases with increasing T_{mxc}, there is a one-to-one correspondence between I_c and T_{mxc}, so shifts in I_c can be transduced into shifts of graphene flake temperature. 140

7.6 **Power-Temperature Curves. a,** Electron-side flake temperature as a function of heat power. From the injected DC current I_{heater} and measured voltage drop V across the heater port, the injected heater power can be determined $P_{heater} = I_{heater} \times V$. From the I_c vs. I_{heater} traces in Fig. 3d,i and the I_c vs. T_{mxc} calibration in Fig. 3e,j, flake temperature can be determined as a function of applied P_{heater}. Color corresponds to the mixing chamber stage temperature. **b,** G_{th} vs. T_{mxc}. Taking the numerical derivative $\frac{\partial P}{\partial T}$ of Fig. 4a allows the data to be plotted on a single line. Fit line is to the power law $G_{th} = \partial P/\partial T = n\Sigma A T^{n-1}$ where n is the scaling exponent and ΣA is the multiplicative factor. **c,** Electron and hole G_{th} vs. T_{mxc} (log-log scale). Hole and electron doping both show power law scaling with an $n = 5$ scaling exponent. The units of the ΣA electron-phonon coupling prefactor in the label are $\mathrm{W/K^5}$. The factor of ~ 2 difference between the electron and hole prefactors is discussed in the main text. 142

8.1 **Schematic of Measurement Chain** First panel shows a pure carrier tone sent down the microwave line. Second panel shows that an applied ω heater current and subsequent 2ω modulation of the heat power and temperature of the graphene flake yields a 2ω modulation of the transmission function (S_{21} parameter) between unheated (blue) and heated (red) states. The pure tone (dashed line) is placed within the bandwidth of the transmission function, such that it will be amplitude modulated at 2ω with a modulation index that depends on the magnitude of the S_{21} dip. Third panel shows the amplitude-modulated signal with sidebands at 2ω as readout on the spectrum analyzer. The measured signal-to-noise ratio of the sideband is used to determine the NEP. **b,** Circuit Diagram. A continuous-wave carrier tone at ω_c is sent down a microwave line to the graphene device, amplified, and read out by a spectrum analyzer. An AC heater current at frequency $\omega = 2\pi \times 337$ Hz injects a 2ω heat power P_{heater} in the graphene flake and produces 2ω amplitude modulation of the carrier tone, as discussed in **a**. 146

8.2 **NEP Measurement Procedure. Left Panel,** Representative spectrum at output of measurement chain. Spectrum as read out by spectrum analyzer (RBW = 1 Hz) for applied heat power off (blue) and on (red). The primary effect of the applied heat is to produce sidebands spaced at 2ω from the the carrier tone. Other peaks in the spectrum exist at multiples of the line frequency. A peak at ω is consistent with a DC offset in the applied heat power. Inset shows the 2ω sideband. **Center Panel,** Sideband Power vs. P_{heater}. In the low-P_{heater} linear-response regime, the sideband voltage $V_{sb} \propto P_{heater}$. Since the spectrum analyzer reads out the sideband power, $P_{sb} \propto P_{heater}^2$, which is consistent with the slope at low P_{heater}. **Right Panel,** NEP vs. P_{heater}. The linear-response regime is characterized by a regime of constant NEP, before rising as the amplitude modulation saturates to its maximal value. The NEP plotted in **g,f** corresponds to the linear response regime (green dashed line). 147

8.3 **Noise Equivalent Power (NEP) Measurement. e,** NEP vs. P_{heater}. The linear-response regime is characterized by a regime of constant NEP, before rising as the amplitude modulation saturates to its maximal value. The NEP plotted in **g,f** corresponds to the linear response regime (green dashed line). **f, g,** NEP vs. carrier power P_c and carrier frequency f_c for **f)** electron-side ($V_{BG} = 1.0\,\mathrm{V}$) and **g)** hole-side ($V_{BG} = -2.75\,\mathrm{V}$). Minimal NEP occurs near the resonance dip minimum where amplitude modulation is largest. As carrier power P_c is increased, the resonance dip downshifts to lower frequencies and is driven into nonlinearity, as characterized by an asymmetric resonance lineshape with steep falling edge and shallow rising edge. The minimum NEP tracks the steep falling edge where amplitude modulation is greatest. 149

Chapter 1

INTRODUCTION

A promising strategy for pushing single-shot energy resolution to the level of individual microwave photons, thermal phonons, or single k_BT heat pulses [96, 102] is the development of thermal detectors with miniscule heat capacities. Graphene, with its vanishing heat capacity and diminished electron-phonon coupling at cryogenic temperatures, is an enticing material platform for achieving heat capacities at the level of single-k_B in solid-state systems at dilution refrigerator temperatures [40, 39]. Key to the design and operation of a thermal detector is the readout method employed to monitor the temperature of the thermal element. However, to date, existing thermometry methods for Van-der-Waals materials have been slow and ill-suited for single-shot calorimetry, limited either by long averaging times, sweep repetition rates, or resetting times of switching Josephson junctions [69].

This dissertation presents Josephson inductance thermometry, a method we have demonstrated for probing the electron temperature of Van-der-Waals materials at milli-Kelvin temperatures. The technique relies upon the inductive loading of a superconducting resonator by a graphene-based Josephson junction, where increases in electron temperature are transduced to shifts of the resonant frequency. This technique brings with it many of the benefits of resonant readout, such as increased measurement bandwidth, fast response times, ease of frequency-division multiplexing, and operation at the lowest temperatures available to a dilution refrigerator where the device parameter regime yields the greatest detector sensitivities [28]. Such a device design is well-suited, for example, to the serving as the fundamental pixel architecture of next-generation dark matter searches [7, 50, 58, 81].

Thermal characterization of the device shows a power/temperature scaling law which disagrees with standard electron-phonon coupling in monolayer graphene [49], but which is in agreement with a novel thermalization mechanism in which defects in the graphene lattice mediate thermal phonon emission by ballistic hot electrons [47]. Signatures of such a mechanism have been observed previously in high-resolution scanning-SQUID measurements, and our thermal characterization presents a power law dependence between applied Joule heat power and electron temperature which is in agreement with predictions of this theory.

In this dissertation, we derive all key performance and noise metrics of a thermal detector, introduce the relevant background for recent superconducting graphene detectors, and provide a detailed discussion of all steps of the experimental apparatus, including nanofabrication and design, device characterization and relation to fundamental properties of ballistic graphene, Joule heating measurements, and noise analysis. This work suggests that graphene-based thermal detectors utilizing resonator readout are a promising route for pushing the limits of detectable single-shot energy resolution to the regime of low-GHz quanta.

This thesis is organized as follows:

In Chapter 2, we introduce the small-signal model of a thermal detector and derive fundamental performance metrics, including the noise-equivalent power arising from thermal fluctuations and the fluctuation-limited energy resolution of a thermal detector operated as a calorimeter.

In Chapter 3, we present important background on the relevant superconducting and cryogenic phenomena which are employed in the design of ultrasensitive graphene-based thermal detectors, including the origin of the temperature-dependent supercurrent in S-N-S junctions, the resistively- and capacitively-shunted junction (RCSJ) impedance model of a Josephson junction, the diminished heat capacity of two-dimensional electron gases at cryogenic temperatures, and a brief review of important types of cryogenic graphene thermal detectors developed over the last decade.

In Chapter 4, we present our measurement setup used for simultaneous microwave reflectometry and AC/DC Joule heating of the graphene flake, including a discussion of the physical mechanisms underlying dilution refrigeration and a full electrical impedance model of the measurement circuit.

In Chapter 5, we detail the nanofabrication procedure for making the resonantly-coupled graphene-based device, including procedures for mechanical exfoliation of the Van-der-Waals material stack and coupling to a superconducting resonator, and key parameters for the superconducting NbTiN resonator employed to perform readout.

In Chapter 6, we demonstrate device operation, in which shifts in the carrier density and mixing stage temperature are transduced into shifts of the resonant frequency. Carrier density sweeps are used to reveal physical properties of the device, including the presence of Fabry-Perot-type oscillation for *n-p-n* doping.

In Chapter 7, we present heating measurements in which Joule heat is applied to the graphene flake and the resulting temperature rise is subsequently measured. A measured power-temperature is presented and a possible mechanism by which hot electrons emit thermal phonons in ballistic graphene is discussed.

In Chapter 8, we present measurements of the noise equivalent power of our device, which is based upon amplitude modulation of a carrier tone via applied AC Joule heat power. From the measured noise equivalent power, we estimate device performance limits.

It is our hope that researchers interested in pushing the limits of ultrasensitive thermal detectors and calorimetry can use this thesis to delve into details of Josephson inductance thermometry as well as the field of cryogenic thermal detection broadly.

Chapter 2

THERMAL DETECTORS: PHYSICAL MODEL AND FUNDAMENTAL PERFORMANCE LIMITS

2.1 Introduction

Of great importance in the use and development of thermal detectors is determining fundamental limits on detector performance. Toward this end, we will undertake the following in this chapter:

- First, we will introduce a physical model of a thermal detector and discuss its operation in several limits.
- Second, we will introduce an important calculational tool called the Fluctuation-Dissipation Theorem (FDT), sketch its derivation from quantum mechanics, and discuss its consequences in the quantum and classical regimes.
- Third, we will use the FDT to derive fundamental noise floors, including the Johnson noise formula and fluctuation-limited noise equivalent power of a thermal detector NEP_{th}.
- Finally, we will derive the energy resolution $\sqrt{\langle E^2 \rangle}$ of thermal detector and show that, in principle, it can be made arbitrarily small when limited by thermal fluctuations.

Having completed this chapter, the reader will be equipped to understand key performance metrics for many state-of-the-art cryogenic detectors, which we will survey in the next section. Additionally, they will be well-equipped to understand the measured figures-of-merits of our graphene Josephson junction-based detector.

2.2 Linear Model of a Thermal Detector

What is a thermal detector?

Of the myriad types of detectors in use today, the thermal detector is particularly simple. Radiation is absorbed by the detector, converts to heat, and induces a temperature rise which is measured out through some experimental setup. From this measured temperature rise, the magnitude of the incident radiation can be

determined, sometimes by employing an additional calibration step. Assuming low absorption loss, the detector temperature rises in proportion to the energy contained in the radiation, such that the detector will experience a larger temperature rise as the incident photon energy is increased $\Delta T \propto E_{photon}$ or as the flux of incident photons are increased $\Delta T \propto E_{photon}\dot{n}_{photon}$. The former mode of operation is termed 'calorimetry' or 'single-photon detection' while the latter is called 'bolometry'. In calorimetry, the fact that the detector temperature rises in proportion to the incident photon energy means that it is possible to measure not just the photon time-of-arrival but also the energy of the incident photon. For this reason, thermal detectors are said to possess 'native energy spectroscopy'.

We note here that we have referred to energy quanta as 'photons', though the thermal detector is agnostic to the type of incident energy quantum, provided that such an energy quantum can induce a measurable temperature rise in the detector.

Linear Model of Thermal Detectors

We now describe a linear model of thermal detectors [82]. We note a few assumptions:

- The model exists in the limit in which all equilibration times are short relative to all control and measurement time scales, so that the system always has a well-defined temperature. This is a good assumption for populations of electrons, where the electron-electron scattering takes place on the order of picoseconds, even at cryogenic temperatures when the thermal link between such electrons and the thermal bath phonons becomes weak.
- The model exists in the limit of small deviations in temperature ΔT from the thermal bath T_0, so that we may assume that all nonlinear terms are small and may be ignored.

Under these assumptions, we describe the basic operation of a thermal detector in response to the absorption of incident energy.

The detector is composed of a small island of heat capacity C_{th} connected to a thermal bath fixed at temperature T_0 by a thermal link G_{th}. Initially, the temperature of the island T is in thermal equilibrium with the bath, i.e. $T = T_0$. When heat energy is absorbed by the island, the temperature of the island increases to $T = T_0 + \Delta T$.

We now discuss a few limits:

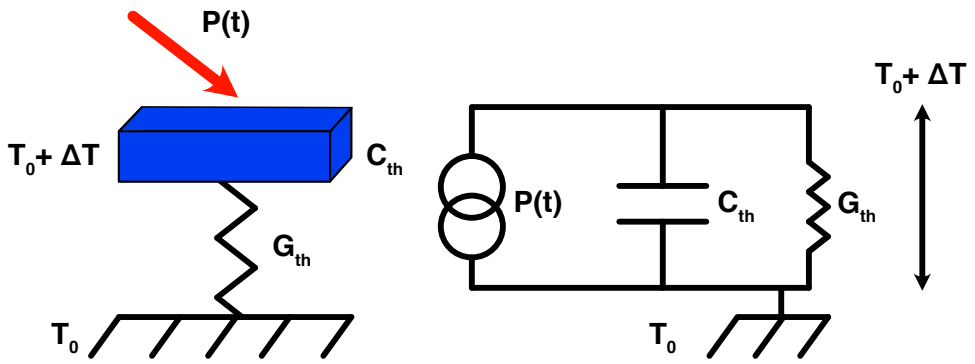

Figure 2.1: **Linear Model of a Thermal Detector.** A device schematic (left) and equivalent circuit model (right) of a thermal detector. Shown are physical parameters heat capacity C_{th} and thermal conductance G_{th}, applied heat power $P(t)$, bath temperature T_0, and temperature rise ΔT.

Isolated Detector, $G_{th} = 0$

Suppose the thermal link between the island and the bath vanishes, i.e. $G_{th} = 0$. This corresponds to the case in which the detector is isolated from its environment. Upon absorption of heat energy Q, the detector temperature will rise according to

$$Q = C_{th}\Delta T \tag{2.1}$$

Applied DC Power P_0

Suppose that a DC heat power $\dot{Q} = P_0$ is incident upon the thermal detector. The temperature of the island will rise until ΔT drives an equal heat power through the thermal link G_{th} to the bath

$$P_0 = G_{th}\Delta T \tag{2.2}$$

Applied Time-dependent Power $P(t)$

Suppose a time-dependent heat power $P(t)$ is incident upon the island. Then, both of the above processes will occur, i.e. the temperature of the island will increase in proportion to C_{th} and heat power will flow through the thermal link G_{th}.

$$P(t) = G_{th}\Delta T(t) + C_{th}\frac{d\Delta T(t)}{dt} \tag{2.3}$$

Applied AC heat power $P(\omega)$

Suppose an AC heat power $P(\omega) = P_0 e^{i\omega t}$ is incident upon the island. We can Fourier transform the above equation to obtain the following

$$P(\omega) = G_{th}\Delta T(\omega) + i\omega C_{th}\Delta T(\omega) \tag{2.4}$$

This can be rearranged to

$$\Delta T(\omega) = \frac{\Delta P(\omega)/G_{th}}{1 + i\omega\tau_{th}} \tag{2.5}$$

for $\tau_{th} = \frac{C_{th}}{G_{th}}$. We see immediately that the thermal response of an applied AC $P(\omega)$ will experience a 1-pole roll-off for $\omega > \frac{1}{\tau_{th}}$. As we will show later in this chapter, this roll-off has several interesting implications for the character of the thermal fluctuations across an island-bath system, the fluctuation-limited noise equivalent power (NEP), and fundamental energy resolution δE_{rms} of thermal detectors.

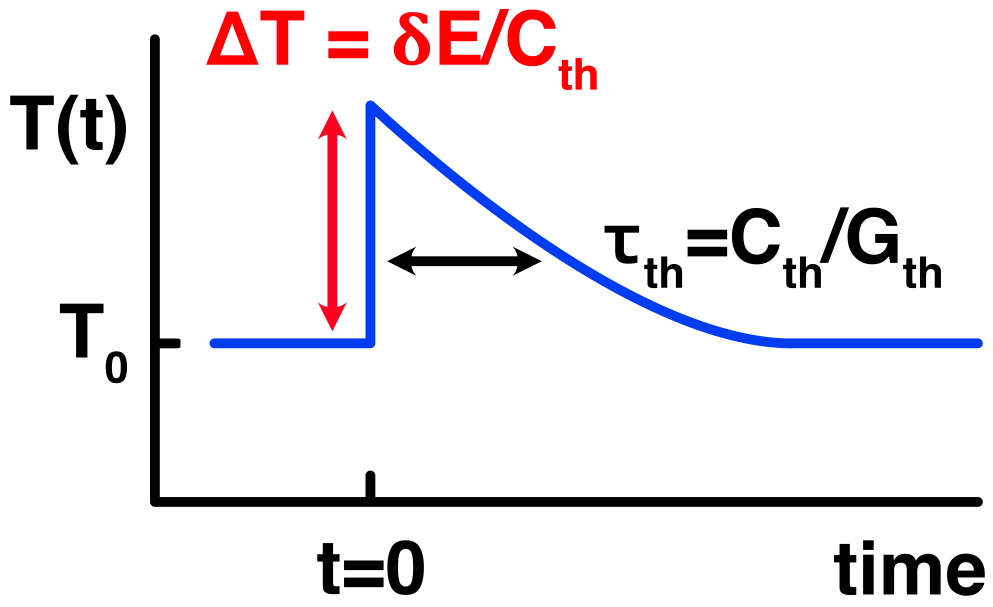

Figure 2.2: **Thermal Response of a Single Absorption Event.** In response to the absorption of energy quantum δE, the temperature of a thermal detector increases by $\Delta T = \frac{\delta E}{C_{th}}$ and subsequently decays to bath temperature T_0 over a time $\tau_{th} = \frac{C_{th}}{G_{th}}$.

Example: Thermal response of a single absorption event

We now consider the response of a thermal detector to an absorption of a single energy quantum, i.e. a thermal detector used as a calorimeter. This example will illustrate several important features of a thermal detector, including its response time and native energy spectroscopy.

Suppose an energy quantum δE is absorbed at time $t = 0$. Then, we may place a boundary condition upon the temperature response of the detector

$$\Delta T(t = 0) = \Delta T_0 = \frac{\delta E}{C_{th}} \tag{2.6}$$

Allowing the detector to evolve according to the equation [], we determine

$$\Delta T = \Delta T_0 e^{-t/\tau_{th}} \tag{2.7}$$

where the thermal response is a decaying exponential with time constant $\tau_{th} = \frac{C_{th}}{G_{th}}$, in agreement with the one-pole roll-off of ΔT in frequency space.

From this example, we determine three important properties of a thermal detectors.

- First, ΔT_0 is proportional to δE, demonstrating a means of determining the energy of an incident energy quantum providing the C_{th} of the detector is known (or can be estimated). It is clear that pushing down the energy sensitivity of a calorimeter/single-photon detector will require minimizing C_{th}. This is one motivation for building graphene-based thermal detectors.

- Second, although we have stated that the photon arrives at $t = 0$, this of course is a proxy for time-of-arrival of an incident photon. Thus, we can determine the photon time-of-arrival by observing the time-domain thermal response of a thermal detector.

- Third, the thermal time constant τ_{th} provides an important response time for comparison to the arrival rate of incident photons. Calorimeters operate in the limit of few photon arrivals in time τ_{th} while bolometers operate in the limit of many photon arrivals in time τ_{th}.

2.3 Fluctuation Dissipation Theorem

One of the most useful applications of quantum mechanics for the experimental physicist is the fluctuation-dissipation theorem (FDT), which can be used to derive

the Johnson noise relation and other fundamental noise floors. It is surprising, then, that few undergraduate quantum mechanics courses treat this theorem. To illustrate this important tool, we will sketch the derivation of the FDT from quantum mechanics, discuss classical and quantum mechanical limits, and use this relation to derive the Johnson noise formula and the noise-equivalent power arising from temperature/entropy fluctuations of a small island connected to a thermal bath. The latter is often the fundamental noise floor of a thermal bolometric or calorimetric device.

A Brief Overview of the Fluctuation Dissipation Theorem

Before delving into the details of the derivation, we give a brief overview of the FDT in the classical and quantum regimes [67], [23].

FDT in the Classical Picture

Suppose you have a physical system with a linear relation between a drive f and a response x

$$x = \alpha f$$

The susceptibility α is the transfer function between the drive and response and has real (in-phase) and imaginary (quadrature) components:

$$\alpha = \alpha' + i\alpha''$$

We will show that the imaginary component of the susceptibility α'' refers to the dissipation, i.e. rate of energy loss, of the system. Note that in the above equations we have omitted time t and frequency ω dependence of the variables for clarity, though this will be rectified in the subsequent discussion.

If the drive f can be interpreted to have a random, fluctuating component, the drive and the response have associated variances about their mean values, i.e. $\langle x^2 \rangle$ and $\langle f^2 \rangle$, respectively. We will show for thermodynamic systems that

$$\langle x^2 \rangle \propto \alpha''$$

In other words, the variance of the response is proportional to the degree to which the response is 90°-out-of-phase with the drive.

FDT in the Quantum Picture

Suppose you have a quantum mechanical system with quantized energy levels $|n\rangle$, $|m\rangle$ (where $E_m > E_n$) that is subjected to a linear periodic perturbation $\hat{V} = -\hat{x} f_0 \cos\omega t$, which can be interpreted as the quantum mechanical analog of a classical drive. If the perturbing frequency is at the energy difference of the two levels $\omega = (E_m - E_n)/\hbar \equiv \omega_{nm}$ and the perturbing potential $\hat{V}$ contains off-diagonal terms x_{nm} that allow transitions between $|n\rangle$ and $|m\rangle$, then there will be two rates of interest, the rate of emission of $\hbar\omega$ (the system loses energy) and the rate of absorption of $\hbar\omega$ (the system gains energy). We will show that

$$\langle \hat{x}^2 \rangle \propto \left(\overbrace{\rho_n}^{\substack{\textbf{Absorption} \\ \omega_n+\omega=\omega_m}} + \overbrace{\rho_m}^{\substack{\textbf{Emission} \\ \omega_m-\omega=\omega_n}} \right) \times |x_{nm}|^2 \delta(\omega + \omega_{nm}) \tag{2.8}$$

$$\alpha'' \propto \left(\overbrace{\rho_n}^{\textbf{Heat In}} - \overbrace{\rho_m}^{\textbf{Heat Out}} \right) \times |x_{nm}|^2 \delta(\omega + \omega_{nm}) \tag{2.9}$$

where $\langle \hat{x}^2 \rangle$ measures the degree of fluctuations, $\alpha'' = \frac{Q}{\omega |f_0|^2}$ is the normalized energy flow Q into ($\alpha'' > 0$) or out of ($\alpha'' < 0$) the system, and ρ_n and ρ_m refer to the number occupation of states $|n\rangle$ and $|m\rangle$, respectively.

For equal occupation of $|n\rangle$ and $|m\rangle$, i.e. $\rho_n = \rho_m$, the variance $\langle \hat{x}^2 \rangle$ will be finite, but α'' will vanish since the rates of incoming and outgoing energy cancel. However, if the quantum mechanical system is connected to a thermal bath, the occupation of the energy levels follow a Boltzmann distribution, i.e. $\rho_m/\rho_n = e^{-(E_m - E_n)/k_B T}$. This implies that the rate of absorption is larger than the rate of emission. It follows that the system will absorb energy from the drive ($\alpha'' > 0$), which is interpreted as an uptake of heat. This picture will be used to derive the relation

$$\langle \hat{x}^2 \rangle \propto \alpha'' \times \underbrace{\left\{ \overbrace{\frac{1}{2}}^{\substack{\text{Zero Point} \\ \text{Motion}}} + \overbrace{\frac{1}{e^{E/k_B T} - 1}}^{\text{B-E Distribution}} \right\}}_{\text{Average Occupation Number}}$$

where the two terms in braces show that the FDT smoothly interpolates between the quantum and classical regimes.

In short, when a quantum system is connected to a thermal bath and subjected to a periodic linear perturbation, transitions between different states will produce both

a finite $\langle \hat{x}^2 \rangle$ and a net uptake of heat. Taking the limit of large temperature T will recover the classical FDT.

What is dissipation?

Dissipation is the net rate of energy loss from a physical system. To quantify the dissipation of a driven classical system, we start with a relation from Hamiltonian mechanics for a conservative Hamiltonian $H = H(t, p_i, q_i)$ and mean energy E

$$\frac{dE}{dt} = \left\langle \frac{\partial H}{\partial t} \right\rangle \tag{2.10}$$

This relation tells us that the time derivative of the mean energy of the system equals the mean of the partial derivative of the Hamiltonian with respect to time.

Why is $\frac{dE}{dt}$ related only to the partial derivative of the Hamiltonian $\frac{\partial H}{\partial t}$ instead of the total derivative $\frac{dH}{dt}$? Ultimately, the other terms in the total derivative will cancel out. Consider the expression for the total derivative

$$\frac{dH}{dt} = \frac{\partial H}{\partial t} + \sum_i \left\{ \frac{\partial H}{\partial q_i} \dot{q}_i + \frac{\partial H}{\partial p_i} \dot{p}_i \right\} \tag{2.11}$$

$$\tag{2.12}$$

For a Hamiltonian system, we know that

$$\dot{q}_i = \frac{\partial H}{\partial p_i} \qquad \dot{p}_i = -\frac{\partial H}{\partial q_i} \tag{2.13}$$

It follows that

$$\frac{dH}{dt} = \frac{\partial H}{\partial t} + \sum_i \left\{ \frac{\partial H}{\partial q_i} \frac{\partial H}{\partial p_i} - \frac{\partial H}{\partial p_i} \frac{\partial H}{\partial q_i} \right\} \tag{2.14}$$

$$= \frac{\partial H}{\partial t} \tag{2.15}$$

where it follows that that a time-independent Hamiltonian conserves mean energy.

However, this derivation applied to the case of a conservative Hamiltonian system. In order to take into account dissipation, we include the so-called Rayleigh dissipation function

$$f = \frac{1}{2}\sum_i \gamma \dot{q_i}^2 \tag{2.16}$$

which yields the updated Hamilton equations

$$\dot{q_i} = \frac{\partial H}{\partial p_i} \qquad \dot{p_i} = -\frac{\partial H}{\partial q_i} - \frac{\partial f}{\partial \dot{q_i}} \tag{2.17}$$

If we have only one coordinate $q_i = x$, including this dissipation function in the previous derivation gives us the following relation

$$\frac{dE}{dt} = \left\langle \frac{\partial H}{\partial t} - \gamma \dot{x}^2 \right\rangle \tag{2.18}$$

We will show that when the Hamiltonian contains a time-dependent linear drive term, the first term corresponds to the heat energy taken up by the system from the applied drive while the second term corresponds to the rate of energy dissipated out of the system, $P = F \times v = -\gamma v^2$. We will show that these two terms have equal magnitude and opposite sign, implying that any net energy taken up from the drive will be dissipated from the system.

For a time-dependent linear drive, we include the energy term

$$\hat{V} = -\hat{x} f(t) = -\hat{x}(f_0 e^{-i\omega t} + f_0 e^{i\omega t}) \tag{2.19}$$

Then, using the susceptibility relation between the drive and response $x(\omega) = \alpha(\omega) f(t)$, we have

$$x = \alpha(\omega) f_0 e^{-i\omega t} + \alpha(-\omega) f_0 e^{i\omega t} \tag{2.20}$$

For the purpose of concreteness, we will assume here that our system is a driven-damped harmonic oscillator with damping γ and spring constant k, so that the susceptibility is

$$\alpha = \frac{1}{i\omega\gamma + k} \tag{2.21}$$

Using the above relations, and taking the time average (which has the effect of averaging away oscillatory terms), we can show that

$$\frac{dE}{dt} = \left\langle \frac{\partial H}{\partial t} - \gamma \dot{x}^2 \right\rangle \tag{2.22}$$

$$= \frac{-i\omega f_0^2}{4}\Big(\alpha(\omega) - \alpha(-\omega)\Big) + \frac{\gamma\omega^2 f_0^2}{4}\Big(- 2\alpha(\omega)\alpha(-\omega)\Big) \tag{2.23}$$

We can further simplify this equation by expanding $\alpha(\omega) = \alpha'(\omega) + i\alpha''(\omega)$ into real and imaginary parts,

$$\frac{dE}{dt} = \frac{\omega f_0^2}{2}\alpha''(\omega) - \frac{\omega\gamma f_0^2}{2}\Big(\alpha'(\omega)^2 + \alpha''(\omega)^2\Big) \tag{2.24}$$

$$= \frac{\omega f_0^2}{2}\frac{\omega\gamma}{\omega^2\gamma^2 + k^2} - \frac{\omega f_0^2}{2}\frac{\omega\gamma}{\omega^2\gamma^2 + k^2} \tag{2.25}$$

$$= 0 \tag{2.26}$$

Here we see that the rate of uptake of heat energy by the system from the drive is given by

$$Q = \frac{\omega f_0^2}{2}\alpha''(\omega) \tag{2.27}$$

which is subsequently dissipated out of the system by the damping term. They key takeaway from this expression is that the rate of heat uptake by the system Q is proportional to $\alpha''(\omega)$, the degree to which the response x is out-of-phase with the drive.

What are fluctuations?

Since elementary classical physics, e.g. kinematics, is presented as a set of deterministic processes, it is reasonable to ask why a finite variance $\langle x^2 \rangle$ should be associated with a physical parameter x.

In thermodynamics, the proper description of a physical observable is a probability distribution over accessible values. While a given thermodynamic variable ($\mathcal{S}$, $\mathcal{P}$,

$\mathcal{U}$ . . .) in equilibrium will take a mean value, there should be an associated variance about that mean value. In particular, the appropriate description of a thermodynamic variable x is a probability distribution which peaks about a mean value $\langle x \rangle$ and possesses a variance $\langle x^2 \rangle$

$$p(x)dx = \frac{1}{\sqrt{2\pi\langle x^2 \rangle}} \exp\Big(- \frac{x^2}{2\langle x^2 \rangle}\Big) dx \tag{2.28}$$

where it is assumed in this expression that $\langle x \rangle = 0$. The variance $\langle x^2 \rangle$ will be associated with the dissipation of a physical system in the following derivation.

The Derivation of the FDT from Quantum Mechanics

We now seek to sketch the derivation of the fluctuation-dissipation theorem from quantum mechanics. We follow the treatment in Chapter XII of Landau and Lifshitz Vol. 5 "Statistical Physics" [67] and the original paper by Callan and Welton [23].

The Quantum Mechanical Picture of Fluctuations

We now look to derive the FDT from quantum mechanics. Suppose we have a quantum mechanical system with a series of energy eigenstates $\{... \, |n\rangle \, ... \, |m\rangle \, ...\}$ with corresponding energies $\{...E_n...E_m...\}$. Without loss of generality, suppose the system is initialized to state $|n\rangle$ and (for the moment) we will not assume any relative sizes of E_n and E_m. Let $\hat{x}$ be an operator upon these eigenstates (we will discuss shortly the importance of non-zero off-diagonal terms $\langle m| \, \hat{x} \, |n\rangle$). Since we wish to define a quantum mechanical analog of fluctuations, we look to the operator

$$\frac{1}{2}(\hat{x}_\omega \hat{x}_{\omega'} + \hat{x}_{\omega'} \hat{x}_\omega) \tag{2.29}$$

which can be expanded in Fourier modes

$$(\hat{x}_\omega)_{nm} = \int_{-\infty}^{\infty} \langle m| \, \hat{x} \, |n\rangle \, e^{i(\omega_{nm}+\omega)t} dt = 2\pi \, \langle m| \, \hat{x} \, |n\rangle \, \delta(\omega_{nm} + \omega) \tag{2.30}$$

for $\omega_{nm} = (E_n - E_m)/\hbar$ to obtain

$$(\hat{x}^2)_\omega = \pi \sum_m |x_{nm}|^2 [\delta(\omega + \omega_{nm}) + \delta(\omega + \omega_{mn})] \tag{2.31}$$

where we write $x_{nm} = \langle m| \hat{x} |n\rangle$ for simplicity. The above expression stands for the ω-th Fourier component of the spectral density of $\hat{x}^2$. We see that this quantity will be non-zero only when we consider a Fourier component at the difference of two energy eigenvalues, e.g. $\omega = \omega_{mn} = \omega_m - \omega_n$ or $\omega = \omega_{nm} = \omega_n - \omega_m$. We will see that since $\omega > 0$ and the system is initialized in state ω_n, the former process refers to energy transitions up ($\omega_n + \omega = \omega_m$) while the latter process refers to energy transitions down ($\omega_n - \omega = \omega_m$).

In the above expression, we also see the importance of off-diagonal terms x_{nm} for $n \neq m$. If the energy eigenstates $\{... |n\rangle ... |m\rangle ...\}$ are also eigenstates of $\hat{x}$, i.e. if $\hat{x}$ is diagonal, all $|x_{nm}|^2$ will vanish for $n \neq m$, and the system will remain in $|n\rangle$ for all time.

The Quantum Mechanical Picture of Heat

Now we turn to the quantum mechanical analog of a driving force. Suppose the system is subject to a periodic perturbation at frequency ω

$$\hat{V} = -\frac{1}{2}(f_0 e^{-i\omega t} + f_0^* e^{i\omega t})\hat{x} \tag{2.32}$$

Under this perturbation, Fermi's Golden Rule tells us that there will be a transition rate from $|n\rangle \rightarrow |m\rangle$ of

$$R_{mn} = \frac{\pi |f_0|^2}{2\hbar^2} |x_{mn}|^2 \{\delta(\omega + \omega_{nm}) + \delta(\omega + \omega_{mn})\} \tag{2.33}$$

where $|x_{nm}|^2 = |x_{mn}|^2$. As before, the first term refers to transitions up in energy ($\omega_n + \omega = \omega_m$) while the latter process refers to energy transitions down in energy ($\omega_n - \omega = \omega_m$). Another way of saying this is that in the former case, the system absorbs an energy quantum $h\omega$ from the drive, while in the latter it emits an energy quantum $h\omega$. We also note that the strength of the rate R_{nm} is proportional to $|x_{nm}|^2$ which immediately suggests a correspondence between the rate of energy transitions and the magnitude of the fluctuations $(\hat{x}^2)_\omega$ found in the previous section.

Using the above transition rate, we can now define a quantity analogous to classical heat

$$Q = \sum_m R_{nm}\hbar\omega_{mn} \tag{2.34}$$

which refers to the mean energy absorbed by the body per unit time. For positive Q, the system absorbs a net positive mean energy from the drive, which is subsequently dissipated in the body. Using the expression for R_{nm}, standard algebraic manipulations show that

$$Q = \frac{\pi\omega|f_0|^2}{2\hbar}\sum_m |x_{mn}|^2\{\delta(\omega+\omega_{nm}) - \delta(\omega+\omega_{mn})\} \tag{2.35}$$

Normalizing this quantity, we can obtain an expression for

$$\alpha'' = \frac{Q}{\omega|f_0|^2/2} = \frac{\pi}{\hbar}\sum_m |x_{mn}|^2\{\delta(\omega+\omega_{nm}) - \delta(\omega+\omega_{mn})\} \tag{2.36}$$

Here we see that, up to factors of $\hbar$, this expression differs from the expression for $(\hat{x}^2)_\omega$ only in that this one is a *difference* of the terms in braces, while that one was the *sum* of the terms in braces.

The Competing Rates of Absorption and Emission

So far we have assumed that the system starts in state $|n\rangle$. However, to determine the total rate of energy flow and the total amount of fluctuations, we must relax this condition and allow the system to start in any eigenstate. Accordingly, we sum over all starting energy eigenstates and weight each eigenstate by a weighting parameter ρ_n, as follows:

$$(\hat{x}^2)_\omega = \pi\sum_n\sum_m \rho_n|x_{nm}|^2\{\delta(\omega+\omega_{nm}) + \delta(\omega+\omega_{mn})\} \tag{2.37}$$

$$\alpha'' = \frac{\pi}{\hbar}\sum_n\sum_m \rho_n|x_{mn}|^2\{\delta(\omega+\omega_{nm}) - \delta(\omega+\omega_{mn})\} \tag{2.38}$$

For both quantities of interest, we can reorder the sums as follows

$$(\hat{x}^2)_\omega = \pi\sum_n\sum_m (\rho_n+\rho_m)|x_{nm}|^2\{\delta(\omega+\omega_{nm})\} \tag{2.39}$$

$$\alpha'' = \frac{\pi}{\hbar}\sum_n\sum_m (\rho_n-\rho_m)|x_{mn}|^2\{\delta(\omega+\omega_{nm})\} \tag{2.40}$$

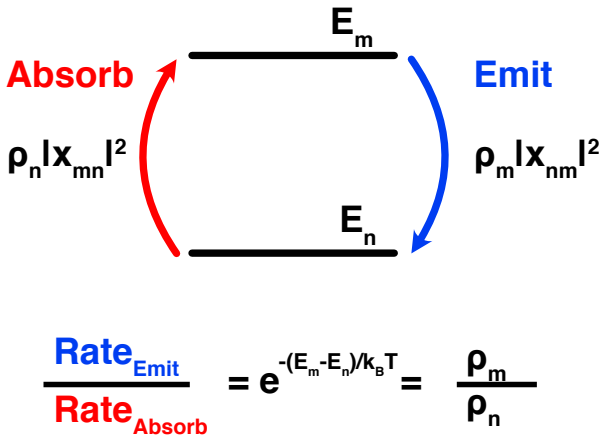

Figure 2.3: **Emission and Absorption Rates.** Two energy levels $|m\rangle$ and $|n\rangle$ with energies $E_m > E_m$ are shown. Absorption of energy quanta (red) allows transitions from $|n\rangle$ to $|m\rangle$, while emission of energy quanta (blue) allows the reverse transitions from $|m\rangle$ to $|n\rangle$. In the presence of a thermal bath, the ratio of the emission and absorption rates is set by the ratio of Boltzmann factors $\rho_n = e^{-E_n/k_BT}/\mathcal{Z}$.

The above expressions are useful when we consider transitions between two energy eigenstates $|n\rangle, |m\rangle$ where $\omega_n + \omega = \omega_m$ as enforced by the delta function. The ρ_n term refers to the transitions which start in $|n\rangle$, absorb a quantum $\hbar\omega$, and transition up to $|m\rangle$. The ρ_m term refers to the reverse processes which start in $|m\rangle$, emit a quantum $\hbar\omega$, and fall to $|n\rangle$. It is evident that both the absorption and emission rates add to the amount of fluctuations $(\hat{x}^2)_\omega$ while the normalized rate of heat flow α'' depends on the difference between these two processes.

However, here arises a problem. We know from the second law of thermodynamics that a system subjected to an applied drive should absorb a net positive quantity of heat, i.e. $\alpha'', Q > 0$. However, nowhere in our description have we introduced an asymmetry between the absorption and emission rates. If we assume an equal weight for all energy levels, i.e. $\rho_n = \rho_m$, this will force $\alpha'' = 0$ no matter the magnitude of the drive, which clearly violates the second law.

The solution to this problem is that we connect our quantum system to a thermal bath held at temperature T. This enforces the condition that the probability of being in a given energy levels is Boltzmann distributed, i.e. $\rho_n = e^{-E_n/k_BT}/\mathcal{Z}$. It follows that higher energy states will be less populated than low energy states, i.e. $\rho_m/\rho_n = e^{-(E_m-E_n)/k_BT}$, and, therefore, that the rate of energy absorption will be

larger than the rate of emission.

Exploiting a property of the delta function, we can bring the factors of ρ_n, ρ_m outside of the sum

$$(\hat{x}^2)_\omega = \pi(1 + e^{-\hbar\omega/k_BT}) \sum_n \sum_m \rho_n |x_{nm}|^2 \{\delta(\omega + \omega_{nm})\} \tag{2.41}$$

$$\alpha'' = \frac{\pi}{\hbar}(1 - e^{-\hbar\omega/k_BT}) \sum_n \sum_m \rho_n |x_{mn}|^2 \{\delta(\omega + \omega_{nm})\} \tag{2.42}$$

where we see that the sums are now equal for both quantities. Thus, we can relate the two quantities

$$(\hat{x}^2)_\omega = \hbar\alpha'' \frac{1 + e^{-\hbar\omega/k_BT}}{1 - e^{-\hbar\omega/k_BT}} = 2\hbar\alpha'' \left\{ \frac{1}{2} + \frac{1}{e^{\hbar\omega/k_BT} - 1} \right\} \tag{2.43}$$

The terms in braces can be interpreted as the zero-point motion and Bose-Einstein occupation factor, respectively.

We have successfully derived the fluctuation-dissipation theorem from quantum mechanics. Let us now interpret this result in the quantum (low-temperature) and classical (high-temperature) limits.

Quantum Limit of the FDT

We consider the limit in which $\frac{\hbar\omega}{k_bT} >> 1$. For this argument, we shall assume there is a minimum energy level $E_0 = \hbar\omega_0$ and keep terms of order $\frac{1}{Z_0} e^{-\hbar\omega_0/k_BT}$, so that

$$(\hat{x}^2)_\omega = \pi \sum_m |x_{0m}|^2 \times \delta(\omega + \omega_{0m}) \tag{2.44}$$

$$\alpha'' = \frac{\pi}{\hbar} \sum_m |x_{0m}|^2 \times \delta(\omega + \omega_{0m}) \tag{2.45}$$

The interpretation is that the system sits in its lowest energy state E_0 and can absorb photons $\hbar\omega$ from the drive that excite it to higher energies with a rate determined exclusively by the off-diagonal terms $|x_{0m}|^2$. Since the system can absorb, but not emit, energy it follows that $Q > 0$. Since there is a non-zero probability of

transitions, $(\hat{x}^2)_\omega > 0$. In this low-temperature limit, the Bose-Einstein occupation term of the FDT vanishes and we are left with

$$(\hat{x}^2)_\omega = \hbar\omega \times \frac{\alpha''}{\omega} \tag{2.46}$$

Classical Limit of the FDT

Now we consider the opposite limit $\frac{\hbar\omega}{k_b T} << 1$. Here, many energy levels are occupied and the ratio of occupation probabilities for two energy levels ω_m and ω_n, where $\omega_m > \omega_n$, is $\frac{\rho_m}{\rho_n} = e^{-\hbar\omega_{mn}/k_B T} \approx 1 - \frac{\hbar\omega_{mn}}{k_B T}$. This means there is a small asymmetry between the emission and absorption rates of these two energy levels of order $\frac{\hbar\omega_{mn}}{k_B T}$.

For an applied drive ω at the difference between two energy levels, i.e. $\omega = \omega_{mn}$, we have

$$(\hat{x}^2)_\omega = \pi(2 - \frac{\hbar\omega}{k_B T}) \sum_n \sum_m \rho_n |x_{nm}|^2 \{\delta(\omega + \omega_{nm})\} \tag{2.47}$$

The factor of $2 - \frac{\hbar\omega_{mn}}{k_B T}$ means the absorption and emission rates contribute *almost* the same amount to the fluctuations, with the emission process contributing less by an amount $\frac{\hbar\omega_{mn}}{k_B T}$.

Likewise, we have

$$\alpha'' = \frac{\pi}{\hbar} \times \frac{\hbar\omega}{k_B T} \sum_n \sum_m \rho_n |x_{mn}|^2 \{\delta(\omega + \omega_{nm})\} \tag{2.48}$$

Here, the small $\frac{\hbar\omega_{mn}}{k_B T}$ asymmetry between emission and absorption rates means that the heat absorbed is proportional precisely to $\frac{\hbar\omega_{mn}}{k_B T}$.

In this high-temperature limit, the Bose-Einstein occupation dominates over the zero point motion, so

$$(\hat{x}^2)_\omega = 2k_B T \times \frac{\alpha''}{\omega} \tag{2.49}$$

We note that the $\hbar$ has vanished from the equation, as is expected in the classical limit.

2.4 Fundamental Noise Sources and Detection Limits

We now use the FDT to derive fundamental noise limits resulting from dissipation in two systems, a resistor and an island connected to a thermal bath.

Applications of the FDT: Johnson Noise of a Resistor

We derive the Johnson-Nyquist noise formula by considering a linear system in which voltage V is the generalized force, charge Q is the generalized response, and $U = QV$ is the associated energy. For the simple case of a voltage placed across a resistor R, working in frequency space we have

$$-i\omega R\widetilde{Q} = \widetilde{V} \tag{2.50}$$

The associated susceptibility α is all-imaginary:

$$\alpha(\omega) = \frac{\widetilde{Q}}{\widetilde{V}} = \frac{i}{\omega R} \tag{2.51}$$

$$\alpha''(\omega) = \frac{1}{\omega R} \tag{2.52}$$

From 2.43, the second moment of the response is

$$\langle Q^2\rangle = \frac{2}{\pi}\int_0^\infty \frac{\hbar}{\omega R}\left\{\frac{1}{2} + \frac{1}{e^{\hbar\omega/k_BT} - 1}\right\} d\,\omega \tag{2.53}$$

Taking the high-temperature limit in which $\hbar\omega/k_BT << 1$

$$\langle Q^2\rangle = \frac{4k_BT\Delta f}{R\omega^2} \tag{2.54}$$

where we have limited the integration interval to a width Δf. This implies a current noise through the resistor of magnitude

$$\langle I^2\rangle = \langle \omega^2 Q^2\rangle = \frac{4k_BT\Delta f}{R} \tag{2.55}$$

We can obtain the generalized force noise $\langle V^2\rangle$ by dividing the $\langle Q^2\rangle$ by response $|\alpha(\omega)|^2$ to obtain

$$\langle V^2 \rangle = 4k_B T R \Delta f \tag{2.56}$$

This is the celebrated Johnson-Nyquist noise formula describing the fundamental voltage fluctuations across a resistor R at temperature T over frequency width Δf [89, 53].

Applications of the FDT: Johnson Noise of an RC Circuit

We now consider the case of a series RC circuit. Suppose a voltage V drops over a series combination of resistor R and capacitor C, so that the following relation holds

$$V = \frac{Q}{C} + \dot{Q}R \tag{2.57}$$

where Q is defined as the charge across the plates of the capacitor.

In the frequency domain, the susceptibility is

$$\alpha = \frac{\widetilde{Q}}{\widetilde{V}} = \frac{C}{1 - i\omega\tau} \tag{2.58}$$

$$= \frac{C}{1 + \omega^2\tau^2} + i\frac{\omega C\tau}{1 + \omega^2\tau^2} \tag{2.59}$$

where $\tau = RC$.

Using the same procedure as the previous section, we find in the high-temperature limit (per frequency)

$$\langle Q^2 \rangle_f = \frac{4k_B T\tau C}{1 + \omega^2\tau^2} \tag{2.60}$$

This implies a roll-off of the charge fluctuations across the capacitor for $\omega > 1/\tau$. Multiplying both sides by ω^2 gives the current fluctuations through the resistor

$$\langle I^2 \rangle_f = \frac{4k_B T\tau C\omega^2}{1 + \omega^2\tau^2} \tag{2.61}$$

For frequencies much larger than the $1/\tau$ roll-off

$$\lim_{\omega >> 1/\tau} \langle I^2 \rangle_f = \frac{4k_B T}{R} \tag{2.62}$$

which is in agreement with the previous section. As before, dividing $\langle Q^2 \rangle_f$ by $|\alpha(\omega)|^2$ produces

$$\langle V^2 \rangle_f = 4k_B T R \tag{2.63}$$

The interpretation here is that a constant fluctuating force noise $\langle V^2 \rangle_f$ drives the RC circuit and produces response fluctuations given by $\langle Q^2 \rangle_f$ and $\langle I^2 \rangle_f$.

Applications of the FDT: Temperature Fluctuations of a Small Island

We now turn our attention to determining the noise floor of our thermal device [26, 30]. In particular, we consider a small island of heat capacity C_{th} with a thermal link G_{th} to a large bath held at temperature T. To review the assumptions underlying the linear thermal model used in this chapter, we assume that control parameters are applied on time scales much longer than the time scales of equilibration of the island to the thermal bath, which is typically a good approximation for cryogenic bolometric and calorimetric devices. This will justify our use of a lumped element circuit model for temperature increases accompanying applied heat power.

In this case, the relation of heat and entropy give us our generalized force and generalized response. Since the relation

$$\delta Q = T \delta S \tag{2.64}$$

tells us that an increase in entropy δS at temperature T is associated with an increase of heat energy δQ, our generalized force is δS and our generalized response is δT.

The standard lumped-element model of a thermal detector in the presence of an applied heat power $\frac{\partial Q}{\partial t}$ is

$$\frac{\partial Q}{\partial t} = G_{th} \delta T + C_{th} \frac{\partial T}{\partial t} \tag{2.65}$$

$$T \frac{\partial S}{\partial t} = G_{th} \delta T + C_{th} \frac{\partial T}{\partial t} \tag{2.66}$$

$$\tag{2.67}$$

In the frequency domain, this corresponds to a susceptibility

$$\alpha = \frac{\delta T}{S} = \frac{\omega^2 T\tau/G}{1+\omega^2\tau^2} + i\frac{\omega T/G}{1+\omega^2\tau^2} \tag{2.68}$$

From which we determine that

$$\alpha'' = \frac{\omega T/G}{1+\omega^2\tau^2} \tag{2.69}$$

From the FDT in the high-temperature limit, we find

$$(\Delta T^2)_f = \frac{4k_B T^2/G}{1+\omega^2\tau^2} \tag{2.70}$$

which tells us that the variance of the temperature fluctuations with increasing frequency will experience a roll-off at $\omega_{th} = 1/\tau_{th}$. We note there are two factors of T in the numerator. One arises from low-frequency response of the system, while the other arises from the $\frac{k_B T}{\hbar\omega}$ occupation number. Further, integrating this expression over frequency gives us the expression

$$\langle \Delta T^2 \rangle = \frac{k_B T^2}{C_{th}} \tag{2.71}$$

which gives the magnitude of fundamental temperature fluctuations across the thermal link. This expression is interesting for two reasons. First, it shows that the integrated area of $(\Delta T^2)_f$ is independent of G_{th}. This means that increasing G_{th} will decrease the magnitude of low-frequency ($\omega < \frac{1}{\tau_{th}}$) temperature fluctuations while increasing the roll-off frequency ω_{th} (bandwidth) of the fluctuations, and these two effects will cancel to leave the integrated area unchanged. The second is that this expression can also be derived from the following simple argument [85]:

We expect the fractional fluctuations of a thermodynamic system to go as

$$\frac{\Delta T_{rms}}{T} = \frac{1}{\sqrt{N}} \tag{2.72}$$

where N is the system size. If our system size is C_{th} as measured in units of k_B, then $N = C_{th}/k_B$. Squaring both sides of the above equation gives us

$$\langle \Delta T^2 \rangle = \frac{k_B T^2}{C_{th}} \tag{2.73}$$

We can convert the above temperature fluctuation PSD (generalized response) to entropy fluctuations (generalized force) by dividing by $|\alpha(\omega)|^2$, which gives us

$$(\Delta S^2)_f = \frac{4k_B G_{th}}{\omega^2} \tag{2.74}$$

Converting to power units, we obtain

$$(\Delta P^2)_f = \omega^2 T^2 (\Delta S^2)_f = 4k_B T^2 G_{th} \tag{2.75}$$

which is the standard formula for the fluctuation-limited noise equivalent power of a bolometer or calorimeter. We write this key conclusion as follows

$$NEP_{th} = \sqrt{4k_B T^2 G_{th}} \tag{2.76}$$

It is important to note, especially for the next section, that $(\Delta T^2)_f$ rolls off for $\omega > \frac{1}{\tau_{th}}$ while $(\Delta P^2)_f$ and NEP_{th} are constant for all frequencies.

Energy Resolution of a Calorimeter

We might assume that the fundamental energy resolution E_{rms} of a thermal detector when used as a single photon detector is set by the fundamental temperature fluctuations T_{rms} of a small island of heat capacity C_{th} connected to a thermal bath of temperature T

$$E_{rms} = C_{th} T_{rms} = \sqrt{k_B T^2 C_{th}} \tag{2.77}$$

However, we shall show that by employing a clever weighting procedure to the frequency domain signal, it is possible to improve the energy resolution of a fluctuation-limited thermal detector *without bound* by increasing the measurement bandwidth BW, according to

$$\sqrt{\langle E^2 \rangle} = \frac{NEP_{th}}{2\sqrt{BW}} \tag{2.78}$$

Thus, in principle, it is possible to make the energy resolution arbitrarily small by making the measurement bandwidth arbitrarily large.

Ultimately, the reason for this surprising result lies in *where* within the measurement chain a fundamental noise source arises. White noise at the output of the measurement chain degrades the signal-to-noise ratio for $\omega > \frac{1}{\tau_{th}}$ while white noise at the input does not. To derive this result, we perform the following procedure:

- First, we will determine the weights on the measured signal and rms noise which optimize the signal-to-noise ratio.
- Second, we will derive an expression for the energy resolution E_{rms} from this weighting procedure in terms of the noise equivalent power NEP of the detector.
- Third, we will consider the energy resolution E_{rms} for two different sources of noise. This will demonstrate how the location of noise in the measurement chain affects the ultimate energy resolution of the detector.

Determining Weights w_k

Here we describe here a weighting procedure on measured data which can be performed by almost any digital filter. We follow the analysis in McCammon [82].

An estimate of the energy E of a single-absorption event can be made from a series of signal measurements s_i in different bins i which may be summed with weights w_i. In the frequency domain, each signal measurement s_i (per frequency bin) is *independent* of the measurements in other bins, so summing over more bins improves our mean estimate of δE_0. Additionally, there will be an rms noise contribution n_i for each bin, which we also assume is not correlated with the noise contribution in other bins. In the frequency domain, this assumption is valid for stationary processes, which applies to the case of thermal detectors. Therefore, we can define an average and second moment of this weighting procedure

$$\langle V \rangle = \sum_i w_i s_i \tag{2.79}$$

$$\langle \Delta V^2 \rangle = \sum_i w_i^2 |n_i|^2 \tag{2.80}$$

We note that our sum here is symbolic for simplicity. In the next section, we will interpret it as an integral in frequency space. Similarly, we have not specified the units of s_i or n_i here, but we will relate them to physical parameters in the next section.

We now determine the weight w_k which will maximize the signal-to-noise ratio

$$\frac{\partial}{\partial w_k} \frac{\langle V \rangle}{\sqrt{\langle \Delta V^2 \rangle}} = 0 \tag{2.81}$$

$$\implies w_k = \frac{s_i*}{|n_i|^2} \times \frac{\langle \Delta V^2 \rangle}{\langle V \rangle} = \frac{1}{Z_0} \frac{s_i*}{|n_i|^2} \tag{2.82}$$

It follows that

$$\langle V \rangle = \frac{1}{Z_0} \sum_i \frac{|s_i|^2}{n_i^2} \tag{2.83}$$

$$\langle \Delta V^2 \rangle = \frac{1}{Z_0^2} \sum_i \frac{|s_i|^2}{n_i^2} \tag{2.84}$$

Relating E_{rms} to NEP

We will now relate the symbolic sums above to integrals over measurable parameters with the goal of deriving an expression for the measurement uncertainty $E_{rms} = \sqrt{\langle \Delta E^2 \rangle}$ of an incident energy pulse E. Ultimately, we will find that E_{rms} can be related to the integrated NEP of the measurement chain.

A few points to motivate the derivation:

- We assume that our device is a thermal detector with heat power P at the input and voltage V at the output.
- We assume a photon E arrives with delta impulse function $P(t) = E\delta(t)$, where $\delta(t)$ has units of $\frac{1}{\text{Time}}$.
- The terms s_i and n_i above referred to the signal and rms noise per bin at the *output* of the measurement, so their integrals will be interpreted as $\langle V \rangle$ and $\langle \Delta V^2 \rangle$, respectively.
- Ultimately, we are interested in E_{rms} which is the energy uncertainty at the *input* of the thermal detector. So, we will use the responsivity $\frac{\partial \langle V \rangle}{\partial E}$ to refer $\langle V \rangle$ and $\langle \Delta V^2 \rangle$ to the input.

- We will work in the frequency domain since noise between different frequency bins is *uncorrelated* for stationary processes. This means that it is valid to estimate the mean-square voltage ΔV^2 as a sum-of-squares,

$$\langle \Delta V^2 \rangle = \int w_i^2 |n_i|^2 df \tag{2.85}$$

- Altogether, we wish to calculate the function

$$\langle \Delta E^2 \rangle = \frac{\langle \Delta V^2 \rangle|_{t=0}}{\left(\frac{\partial V}{\partial E}\right)^2\Big|_{t=0}} \tag{2.86}$$

We begin by defining the frequency domain analogs of the weighted sums in the previous section for voltage-per-frequency $v(f)$, rms voltage noise-per-frequency $e_n(f)$, and (unitless) weights $w(f)$

$$\langle V(t) \rangle = \int_{-\infty}^{\infty} w(f) v(f) e^{i\omega t} df \tag{2.87}$$

$$\langle \Delta V^2 \rangle = \int_{0}^{\infty} w(f)^2 e_n(f)^2 df \tag{2.88}$$

where the sum-of-squares expression for $\langle \Delta V^2 \rangle$ holds for any time t, while $\langle V(t) \rangle$ is the Fourier transform of the weighted voltage $w(f)v(f)$ to time t. We note that voltage signal $v(t)$ and voltage rms noise $e_n(t)$ in the time domain are as follows:

$$v(t) = \frac{\partial V}{\partial x_i} \ldots \frac{\partial x_i}{\partial T} \frac{\partial T}{\partial P} \times P(t) = S_{VP} \times E\delta(t) \tag{2.89}$$

$$e_n(t) = S_{VP} \times NEP \tag{2.90}$$

where S_{VP} is the responsivity between the input power and output voltage and NEP is the noise equivalent power at the input.

The weights we use in analog to the previous section are

$$w(f) = \frac{1}{Z_0} \frac{v(f)^*}{|e_n(f)|^2} = \frac{\langle \Delta V^2 \rangle}{\langle V \rangle} \frac{v(f)^*}{|e_n(f)|^2} \tag{2.91}$$

where we have expanded out the normalization factor Z_0 for clarity. We note that these normalization factors will cancel in the final expression. The primary things

to remember is that they are constant and can be taken out of the integral, and they have a dependence on E, which we will discuss soon.

The two integrals become

$$\langle V \rangle = \frac{1}{Z_0} \int_{-\infty}^{\infty} \frac{|v(f)|^2}{|e_n(f)|^2} df \tag{2.92}$$

$$\langle \Delta V^2 \rangle = \frac{1}{Z_0^2} \int_{-\infty}^{\infty} \frac{|v(f)|^2}{|e_n(f)|^2} df \tag{2.93}$$

Now, we would like to obtain an expression for $\frac{\partial \langle V \rangle}{\partial E}$ to convert $\langle \Delta V^2 \rangle$ to $\langle \Delta E^2 \rangle$. To do so, we factor out E from the two integrals by defining $v(f) = s(f) \times E$.

$$\langle V \rangle = \frac{E}{Z_0'} \int_{-\infty}^{\infty} \frac{|s(f)|^2}{|e_n(f)|^2} df \tag{2.94}$$

$$\langle \Delta V^2 \rangle = \frac{1}{Z_0'^2} \int_{-\infty}^{\infty} \frac{|s(f)|^2}{|e_n(f)|^2} df \tag{2.95}$$

We note the normalization Z_0 contains factors of E since $\langle V \rangle \propto E$ while $\langle \Delta V^2 \rangle$ is independent of E, so it transforms to $Z_0' = \frac{\langle V^2 \rangle}{\langle S \rangle}$. It follows that

$$\frac{\partial \langle V \rangle}{\partial E}\Big|_{t=0} = \frac{2}{Z_0'} \int_{0}^{\infty} \frac{|s(f)|^2}{|e_n(f)|^2} df \tag{2.96}$$

$$\tag{2.97}$$

where we have used the symmetry of the integrand to change the integration range.

Finally, we have the following expression for the mean-square energy fluctuations at the input

$$\langle \Delta E^2 \rangle = \frac{\langle \Delta V^2 \rangle}{(\partial V / \partial E)^2|_t = 0} = \frac{1}{4 \int_0^{\infty} \frac{|s(f)|^2}{|e_n(f)|^2} df} \tag{2.98}$$

$$= \frac{1}{\int_0^{\infty} \frac{4}{NEP(f)^2} df} \tag{2.99}$$

where we have used the definitions $s(f)^2 = |S_{VP}|^2|P(f)|^2$ and $|e_n(f)|^2 = |S_{VP}|^2 NEP(f)^2$ together with the fact that $|P(f)|^2 = 1$ for a delta function potential transformed to the Fourier domain.

We write our result as follows

$$E_{rms} = \sqrt{\langle \Delta E^2 \rangle} = \frac{1}{\sqrt{\int_0^\infty \frac{4}{NEP(f)^2} df}} \tag{2.100}$$

Sources of NEP

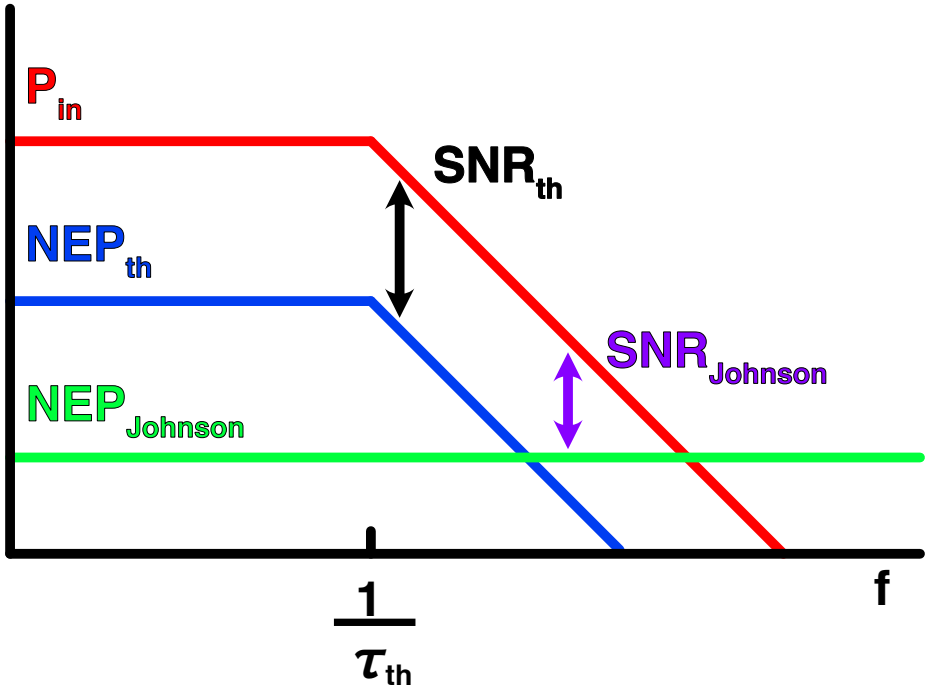

Figure 2.4: **Signal and Noise at the *Output* of the Measurement Chain.** Signal $P(f)$ and noise spectral densities $NEP_{th}(f)$ and $NEP_{Johnson}(f)$ at the measurement output. Both $P(f)$ and $NEP_{th}(f)$ experience a one-pole roll off above the thermal cut off $\omega_{th} = \frac{1}{\tau_{th}}$, producing a signal-to-noise ratio SNR_{th} which does not roll-off above the thermal cut off. By contrast, $NEP_{Johnson}$ is flat at the output, so the signal-to-noise ratio $SNR_{Johnson}$ *does* roll off above ω_{th}.

We now compare two sources of noise to identify how their location within the measurement chain affects the bandwidth over which they can be integrated.

Suppose there exists a resistor at the output of the measurement chain. The associated

Johnson noise and responsivity of this noise source are

$$e_n = \sqrt{4k_B T R \Delta f} \tag{2.101}$$

$$S_{VP} = \frac{\partial V}{\partial P} = \frac{\partial V}{\partial x_i} \cdots \frac{\partial x_i}{\partial T} \frac{\partial T}{\partial P} \tag{2.102}$$

$$= \frac{\partial V}{\partial x_i} \cdots \frac{\partial x_k}{\partial T} \frac{1/G_{th}}{1 + i\omega\tau_{th}} \tag{2.103}$$

It follows that Johnson noise referred to the input of the detector is

$$NEP^2_{Johnson} = \frac{|e_n|^2}{|S_{VP}|^2} = \frac{4k_B T R \Delta f}{|\frac{\partial V}{\partial x_i} \cdots \frac{\partial x_k}{\partial T}|^2} \times G^2_{th}(1 + \omega^2 \tau^2_{th}) \tag{2.104}$$

and the associated signal to noise ratio, referred to input, is

$$SNR_{Johnson} = \frac{|P(f)|^2}{NEP^2_{Johnson}} = \frac{1}{\frac{4k_B T R \Delta f}{|\frac{\partial V}{\partial x_i} \cdots \frac{\partial x_k}{\partial T}|^2} \times G^2_{th}(1 + \omega^2 \tau^2_{th})} \tag{2.105}$$

It is clear that $SNR_{Johnson}$ experiences a one-poll roll due to the thermal response of the calorimeter.

Now, let us look at a different noise source, in particular, the thermal fluctuations at the *input* of the calorimeter

$$NEP^2_{th} = 4k_B T^2 G_{th} \tag{2.106}$$

It follows that the signal-to-noise ratio is frequency independent

$$SNR_{th} = \frac{|P(f)|^2}{NEP^2_{th}} = \frac{1}{4k_B T^2 G_{th}} \tag{2.107}$$

even for frequencies above the thermal time constant $\omega > \frac{1}{\tau_{th}}$.

Physically, what's going on here is that the signal $P(f)$ experiences a thermal roll-off as it passes through the measurement chain, by virtue of the temperature response to applied power

$$\left|\frac{\delta T}{P}\right|^2 = \frac{1/G_{th}^2}{1+\omega^2\tau_{th}^2} \tag{2.108}$$

so, if there is a white noise at the output, the signal-to-noise ratio (relative to that white noise) will also roll-off. However, the fluctuation limited NEP_{th} experiences precisely the same thermal roll-off as $P(f)$ as it passes through the measurement chain, so the signal-to-noise ratio $|\frac{P(f)}{NEP_{th}}|$ does *not* roll off. This is a good reminder that the important quantity in a measurement is neither the signal nor the noise by themselves, but the signal-to-noise ratio.

Since the fluctuation-limited NEP_{th} is frequency independent, the accompanying energy resolution is

$$\sqrt{\langle E^2\rangle} = \frac{NEP_{th}}{2\sqrt{BW}} \tag{2.109}$$

where there is no fundamental limit on the integration bandwidth BW.

Key Takeaway

The key idea in this section concerns the precision with which we can estimate the energy E_0 incident upon a thermal detector operated in calorimeter/single-photon mode. For the signal in frequency space, each frequency bin gives an *independent estimate* of E_0, so averaging over more frequency bins gives a more accurate estimate of E_0. Typically, though, there exists a limit on the bandwidth that can be summed over. For example, when white noise is introduced after the input, the temperature roll-off of the signal above $\omega_{th} = \frac{1}{\tau_{th}}$ degrades the signal-to-noise ratio and limits the bandwidth to $BW = \frac{1}{4\tau_{th}}$. However, rather remarkably, the fluctuation-limited NEP is flat at the input and also rolls off above ω_{th}, which causes the signal-to-noise ratio to be constant for all ω and places no fundamental limit on the bandwidth. Therefore, within this picture, the energy resolution of a fluctuation-limited detector can be made arbitrarily small.

2.5 Conclusion

We review what has been demonstrated in this chapter:

- First, we have introduced a physical model of a thermal detector and discussed its operation under applied DC and AC power, in the frequency and time domains, and for single-quantum absorption events.
- Second, we have introduced the Fluctuation-Dissipation Theorem (FDT), sketched its derivation and discussed its consequences in the quantum and classical regimes.
- Third, we have used the FDT to derive the Johnson-Nyquist noise formula for a resistor and fluctuation-limited noise equivalent power NEP_{th} for a thermal detector.
- Finally, we have derived a limit on the energy resolution $\sqrt{\langle E^2 \rangle}$ of thermal detector and shown that there is no fundamental lower bound on this resolution for a fluctuation-limited thermal device.

The reader should now be equipped to understand the performance limits for a variety of state-of-the-art cryogenic detectors, including for the graphene-based thermal detector we have recently demonstrated.

Chapter 3

GRAPHENE-BASED SUPERCONDUCTING DETECTORS BACKGROUND

In this chapter we discuss some fundamental concepts related to graphene-based superconducting detectors.

- First, we motivate and discuss the phenomenon of the temperature-dependent supercurrent in an S-N-S weak link, which arises from electron-hole reflections at the interface of a normalconductor and a superconductor.
- Second, we motivate the use of two-dimensional electron gases when designing low-heat capacity thermal detectors, with a focus on how graphene's linear band structure can produce exceptionally low heat capacities
- Third, we introduce the resistively- and capacitively-shunted Josephson junction (RCSJ) model which describes the RF and DC electrical impedance of a Josephson junction
- Fourth, we give a brief review of some of the important cryogenic graphene-based thermal detectors in the last decade, many of which integrate superconducting phenomena into their device design in order to push performance limits.
- Finally, we discuss an exciting application of ultrasensitive calorimetry, the measurement of Landauer's postulated minimum $k_B T \log(2)$ heat dissipation associated with the erasure of a classical bit.

Having completed this chapter, the reader will be prepared to understand the physical mechanisms underlying the resonantly-coupled graphene device which will be discussed in subsequent chapters.

3.1 Principles of Superconductor-Normal-Superconductor Junctions

BCS theory, formulated by Bardeen, Cooper and Schrieffer in 1957, explains the origin of the interesting phenomena of superconductors as ultimately originating in a phase transition which occurs at low temperatures [8, 110, 49]. In this phase

transition, particles in the ground state become correlated in a way that can be measured by an order parameter in the limit of length scales much larger than a Fermi wavelength λ_F

$$F_{\sigma\sigma'}(r) = \langle \varphi_\sigma(r)\varphi_{\sigma'}(r)\rangle \tag{3.1}$$

Essentially, this expression means that in the superconducting state where $F \neq 0$, the positions of electrons are correlated. Scaling this order parameter by the strength of the interaction λ produces the pair potential

$$\Delta(r) = \lambda(r)F(r) \tag{3.2}$$
$$= |\Delta(r)|e^{i\varphi(r)} \tag{3.3}$$

where the second line implies that all of the particles in the ground state are associated with a single quantum mechanical phase $\phi(r)$. For a conventional superconductor such as elemental aluminum, this pair potential serves as the relevant energy scale by which *Cooper pairs*— bound states of electrons which are mediated by the attractive interaction of electron-phonon scattering in the presence of a Fermi sea— are energetically lowered from other excitations [44].

Quasiparticles and the BdG Equations

We now look to characterize the excited states (quasiparticle states above the Cooper pair ground state) which will take the form of linear combinations of electrons and holes, each of which possesses an energy strictly bounded below by the superconducting gap energy Δ. This will motivate a key feature of the superconducting density-of-states, which is that there exist no states within an energy Δ of the Fermi energy E_F. In the next section, we will see how this produces a quantum mechanical amplitude for electron-hole reflections at the interface of a superconducting and normalconducting metal.

Quasiparticle states can be elegantly constructed from the eigenstates and eigenvalues of the Bogoliubov-de-Gennes (BdG) equations [49, 44, 110, 2], which are expressed as follows

$$\begin{pmatrix} \frac{\hbar^2k^2}{2m} - \mu & \Delta(r) \\ \Delta^*(r) & \mu - \frac{\hbar^2k^2}{2m} \end{pmatrix} \begin{pmatrix} u_k \\ v_k \end{pmatrix} = E_k \begin{pmatrix} u_k \\ v_k \end{pmatrix} \tag{3.4}$$

To illustrate the difference between the normal-conducting and superconducting states, we introduce a simple case of the BdG equations, with two key simplifications. First, we assume electrons and holes propagate as plane waves, i.e. electron wavefunction is described as $u(r) = u_k e^{i\vec{k}\cdot\vec{r}}$ and hole wavefunction is described by $v(r) = v_k e^{i\vec{k}\cdot\vec{r}}$. Second, we assume bulk superconductivity, which implies that $\Delta(r) = \Delta_0 e^{i\varphi}$ where we have removed the spatial dependence of the phase.

We will first consider the uncoupled ($\Delta_0 = 0$) normal-conducting case and then the coupled ($\Delta_0 \neq 0$) superconducting case.

Uncoupled (Normal State) BdG Equations

In the absence of a superconducting correlations $\Delta_0 = 0$, off-diagonal terms vanish and the BdG equations become

$$\begin{pmatrix} \frac{\hbar^2 k^2}{2m} - \mu & 0 \\ 0 & \mu - \frac{\hbar^2 k^2}{2m} \end{pmatrix} \begin{pmatrix} u_k \\ v_k \end{pmatrix} = E_k \begin{pmatrix} u_k \\ v_k \end{pmatrix} \tag{3.5}$$

Since the matrix is diagonal, the resulting equations are uncoupled.

$$\left(\frac{\hbar^2 k^2}{2m} - \mu\right) u_k = E u_k \tag{3.6}$$

$$\left(\frac{\hbar^2 k^2}{2m} - \mu\right) v_k = -E v_k \tag{3.7}$$

$$\tag{3.8}$$

These sets of equations describe two energy bands (see Fig. 3.1). The top equation describes the electron band, in which electrons propagate as plane waves according to the Schrodinger Equation. As the k-vector of an electron increases, so does its energy since $E_k = \frac{\hbar^2 k^2}{2m} - \mu$.

Conversely, the bottom equation describes the hole band, in which holes also propagate as plane waves according to the Schrodinger equation. Similarly, as the k-vector of a hole increases, so does its energy since its energy is given by $E_k = \mu - \frac{\hbar^2 k^2}{2m}$.

Clearly, the two bands are symmetric about a flip across the Fermi energy axis $E = \mu$. This has an important consequence for the group velocity. While electrons and holes with the same k-vector have the same energy, they have opposite group velocities

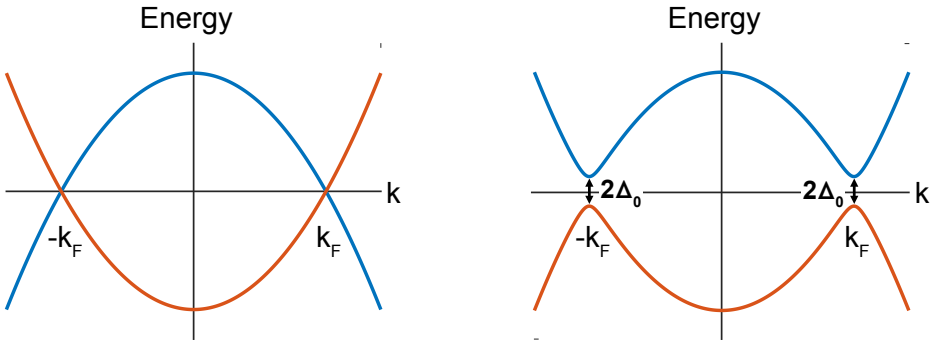

Figure 3.1: **Quasiparticle Energy Bands for Normalconducting and Superconducting States.** (left) In the normal state, the superconducting gap energy vanishes ($\Delta = 0$) and the BdG equations decouple into two different energy bands. The concavity of the electron band (red) implies that electrons have a positive group velocity $\frac{\partial\omega}{\partial k} \geq 0$, whereas the hole band (blue) implies that holes have a negative group velocity $\frac{\partial\omega}{\partial k} \leq 0$. (right) In the superconducting state ($\Delta \neq 0$), the presence of the superconducting gap Δ couples electron and holes to produce quasiparticles, where a quasiparticle of a given k-vector is composed of a linear combination of an electron and hole of the same k-vector. The relative magnitude of the electron and hole contributions depend on the proximity of k to k_F. In the case of the $E > 0$ band, excitations deep within the Fermi-sea are hole-type, excitations far above the Fermi-sea are electron-type, and excitations close to the Fermi sea are of mixed character. This can also be understood from the two quasiparticle energy bands, where the sign of the group velocity of the quasiparticle changes as k sweeps across k_F, indicating a cross-over from hole-type to electron type (blue trace) or vice-versa (red trace).

$\frac{\partial\omega}{\partial k}$. Electrons have positive group velocity $\frac{\partial\omega}{\partial k} > 0$, while holes have negative group velocity $\frac{\partial\omega}{\partial k} < 0$, which implies that electrons and holes with the same k travel with the same speed but in opposite directions. This will have important consequences for the phenomenon of *Andreev reflection*, discussed later in this chapter.

Coupled (Superconducting) BdG Equations

We now consider the case in which the superconducting gap is non-zero, i.e. $\Delta = \Delta_0 e^{i\varphi}$. Just as we might ask about the eigenvectors and eigenvalues of a coupled mass/spring system to determine resonant modes and frequencies of the system, we now ask for eigenvectors and eigenvalues of the BdG equations to determine the excitation energies and linear combinations of electrons and holes which comprise such excitations. Note also that we enforce the normalization condition $|u_k|^2+|v_k|^2 =$

1.

$$\begin{pmatrix} \xi_k - E_k & \Delta_0 e^{i\varphi} \\ \Delta_0 e^{-i\varphi} & -\xi_k - E_k \end{pmatrix} \begin{pmatrix} u_k \\ v_k \end{pmatrix} = 0 \tag{3.9}$$

where, for simplicity, we have written the energy difference relative to the Fermi energy as $\xi_k = \frac{\hbar^2 k^2}{2m} - \mu$. Finding the eigenvalue of this matrix gives an important expression for the energy of the excitations

$$E_k = \pm\sqrt{\xi_k^2 + \Delta_0^2} \tag{3.10}$$

This equations has a few important conclusions. First, it tells us that that every excitation comes with a minimum energy Δ_0, which is why we have referred to this quantity as an important energy scale for superconductivity. This means low-energy disturbances, e.g. phonons with $E < \Delta_0$, will not disturb the system since they do not have sufficient energy to produce transitions between different energy states of the system. In the common parlance, a superconducting system is 'gapped' to excitations.

Second, whereas the two energy bands– electron and hole– were previously uncoupled from one another, they are now coupled, i.e. the modes have *hybridized*. As can be seen in Fig. [...], starting in the positive energy band $E_k = +\sqrt{\xi_k^2 + \Delta_0^2} = +\sqrt{(\frac{\hbar^2 k^2}{2m} - \mu)^2 + \Delta_0^2}$ at $k = 0$ and increasing k, will initially yield excitation energies which decrease as k approaches k_F, but which then 'turn around' at $k = k_F$ and yield energies which increase for $k > k_F$. Clearly, this also means that the group velocity $\frac{\partial\omega}{\partial k}$ is negative (hole-like) for $k < k_F$, while it is positive (electron-like) for $k > k_F$.

The physical interpretation here is that each excitation of the superconducting system is a linear combination of an electron and hole of the same wavevector k, and the relative size of the electron and hole contributions is determined by the proximity of k to the Fermi wavevector k_F. Thus, the same energy band can smoothly interpolate between hole-like and electron-like excitations as k is swept through k_F. This can be seen by considering the eigenvectors of the equation, which are the linear combination of electrons and holes of the same k-vector. Thus,

$$u_k = \frac{1}{\sqrt{2}}\sqrt{1 + \frac{\xi_k}{E_k}} \times e^{i\varphi},\ v_k = \frac{1}{\sqrt{2}}\sqrt{1 - \frac{\xi_k}{E_k}} \tag{3.11}$$

For excitations deep within the Fermi sea $|k| << k_F$, the excitation is essentially hole-like ($u_k \approx 0$, $v_k \approx 1$). For excitations far above the Fermi sea $|k| >> k_F$, the excitation is essentially electron-like ($u_k \approx 1$, $v_k \approx 0$). Excitations close to the Fermi surface $k \approx k_F$ have a mixed character ($u_k \approx \frac{1}{\sqrt{2}}$, $v_k \approx \frac{1}{\sqrt{2}}$), and this mixed character is sustained over an energy width of Δ_0. Thus, we can appreciate that much of the important behavior of superconducting systems occurs within a width Δ_0 of the Fermi energy E_F.

Andreev Reflection

At an N-S interface, an important question is what happens when an electron propagating in the normal metal impinges upon the interface with the superconducting contact. If the electron possesses an energy above the Fermi energy but below the superconducting energy gap Δ, there will be no quasiparticle states of equal energy to which it can transition in the superconductor. Further, if the interface is clean, i.e. high transparency, it can neither undergo a low-energy scattering to another electronic state in the normal metal. What happens then?

The answer is that a different physical process occurs, known as *Andreev reflection*, in which the electron (an excitation above the Fermi sea) reflects as a hole (an excitation below the Fermi sea), where both the electron and hole propagate within the normal metal [15, 1, 100, 9, 111, 108]. In such a reflection event, charge conservation implies that a Cooper pair is transferred to the superconductor. Conversely, if a hole is incident upon the N-S interface, it will reflect as an electron, taking up a Cooper pair from the superconductor. In an S-N-S junction, the back-to-back S-N and N-S junctions allow a round-trip process to occur in which an electron in the normal metal can reflect from one interface as a hole, and the hole can propagate with opposite group velocity to reflect from the the other interface as an electron. The combination of these reflection events allows for the net flow of a Cooper pair, i.e. a supercurrent, through the S-N-S junction. Thus, the source of the Josephson effect in an S-N-S junction is the net transfer of Cooper pairs from one superconducting contact to another mediated by electron-hole reflections at the interfaces.

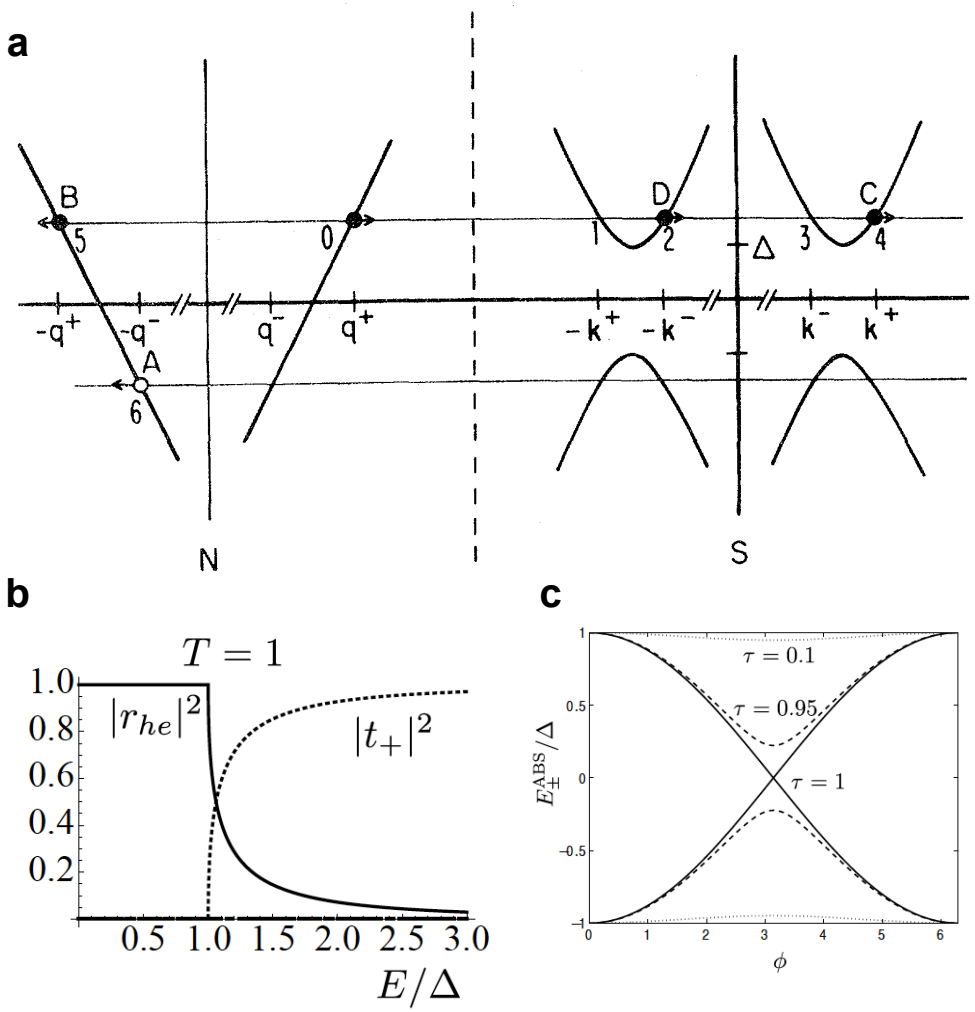

Figure 3.2: **Andreev Reflection**. **a.** Scattering Processes at a Superconductor-Normalconductor Interface, with permission from Blonder, Tinkham, and Klapwijk [15]. In the case of an electron in a normal metal *(0)* incident upon a superconductor, the following processes are considered. Quasiparticle transmission into the left branch *(2)* or right branch *(4)*. Reflection as a normal electron *(5)* or *(6)* Andreev-reflection as a hole **b.** Andreev Reflection coefficients as a function of incident electron energy E (with permission from Heikkilä [49]). For an incident electron, $|r_{he}|^2$ corresponds to the probability of Andreev electron-hole reflection, while t_+ corresponds to the transmission into the superconductor as a quariparticle of equal energy. We see that for electron energies below the superconducting gap $E < \Delta$ only electron-hole reflection may occur. Above the gap, the probability of electron-hole reflection decreases and quasiparticle transmission increases with energy. **c.** Andreev Bound State Energy E^{ABS} vs. the phase difference between the superconductors ϕ (with permission from Heikkilä [49]). For finite transmission coefficients $\tau < 1$, the bound state energy is 2π-periodic, while for perfect transmission it is 4π-periodic.

This phenomena can be formulated as a scattering problem, in which there exist amplitudes for each of the relevant processes [49]. Suppose initially that an electron in the normal metal moves to the right toward the N-S junction with unity amplitude. In this case, the electron can be transmitted into the superconductor as a quasiparticle excitation. Alternatively, it can be reflected in the normal metal as normal reflection *or* it can deposit a Cooper pair into the superconductor, leaving behind a hole of equal energy below the Fermi sea. These possibilities are contained in the following wavefunctions

$$\psi_{normal} = \begin{pmatrix} 1 \\ 0 \end{pmatrix} e^{ikx} + r_{ee} \begin{pmatrix} 1 \\ 0 \end{pmatrix} e^{-ikx} + r_{he} \begin{pmatrix} 0 \\ 1 \end{pmatrix} e^{ikx} \tag{3.12}$$

$$\psi_{supercon} = t_+ \begin{pmatrix} u_0 e^{i\phi_0} \\ v_0 \end{pmatrix} e^{ikx} + t_- \begin{pmatrix} v_0 e^{i\phi_0} \\ u_0 \end{pmatrix} e^{ikx} \tag{3.13}$$

In the limit of a transparent interface, expressions for the coefficients can be obtained by solving for continuity of the wavefunctions (up to a deposition of a Cooper pair in the superconductor) and their derivatives across the boundary. This yields:

$$r_{ee} = 0, \;\; t_+ = t_- = 0, \;\; |r_{eh}|^2 = 1 \;\text{ for }\; |E| < \Delta \tag{3.14}$$

$$r_{ee} = t_- = 0, \;\; |r_{eh}|^2 = \frac{E - \sqrt{E^2 - \Delta^2}}{E + \sqrt{E^2 - \Delta^2}} \;\; |t_+|^2 = 1 - |r_{eh}|^2 \;\text{ for }\; |E| > \Delta \tag{3.15}$$

We explain the subgap ($|E| < \Delta$) scattering process. For energies below the superconducting gap, only evanescent waves can propagate in the superconductor, so the quasiparticle states cannot support a proability current (We note that the above equations hold for probability currents, in the sense that they take into account length scales much larger than the superconducting coherence length, e.g. the length scale of the evanescent wave.). Further, for a transparent interface, there is no amplitude to reflect as a normal metal electron at any energy. So, the only allowed scattering process is that the invident electron reflects as a hole in the normal metal with probability $|r_{he}|^2 = 1$, i.e. Andreev reflection is the only allowed process for subgap energies. Conversely, for energies above the gap, there is a finite amplitude to reflect as a hole and a finite amplitude to transition into the superconductor as a quasiparticle.

It is important to note that the electrical current does not carry heat, since Cooper pairs do not possess entropy. Thus, this mechanism allows the flow of electrical current but blocks the flow heat current, and it is therefore a good candidate for measuring the temperature of an electron gas contained in the normal metal while simultaneously isolating it from external heat loss through the superconducting leads.

Andreev Bound States

We recognize that the S-N-S junction bears a striking resemblance to the elementary picture of a quantum mechanical particle-in-a-box. In particular, unpaired electrons and holes can propagate as waves within the normal metal, but at subgap energies they decay as evanescent waves in the superconducting contacts. (As Blonder, Tinkham, and Klapwijk [15] showed, the current of the evanescent waves is converted into supercurrent of the Cooper pair generated at each reflection, with an exponential dependence on the length from the interface.) Since the length of the normal metal region is finite, we should expect a series of bound states to occur in an S-N-S junction in analogy to the bound states of a particle in a finite length quantum well.

To determine the energies of these bound states, we match the phases of back-to-back electron/hole and hole/electron reflections [49]. For an electron-hole or a hole-electron reflection from a superconducting lead of phase ϕ, it can be shown that the phase accumulated upon this reflection is

$$\varphi_{eh} = -\arccos(E/\Delta) + \phi \qquad \varphi_{he} = -\arccos(E/\Delta) - \phi \tag{3.16}$$

We can write down total accrued phases for the round-trip in the two cases in which an electron is initially incident and when a hole is initially incident.

$$\varphi_1 = (k_e + k_h)L + \phi - 2\arccos(E/\Delta) \tag{3.17}$$

$$\varphi_2 = (k_e + k_h)L - \phi - 2\arccos(E/\Delta) \tag{3.18}$$

where we have assumed that one superconducting lead has phase ϕ and the other superconducting lead has zero phase. In the limit of a ballistic junction, the dynamical phase accumulation is small relative to the phase accrued from the superconducting leads, so we approximate $(k_e + k_h)L \approx 0$. We then enforce the boundary condition for a bound state

$$\varphi_1, \varphi_2 = 2\pi n \tag{3.19}$$

for some integer n. From this phase matching condition, the allowed bound state energies of a transparent contact are

$$E_\pm \approx \pm\Delta \cos(\phi/2) \tag{3.20}$$

If the contact has some transmission coefficient τ, such that $\tau = 1$ characterizes a transparent contact and $\tau << 1$ characterizes a low-transparency (tunnel) contact, the bound states energies are modified to

$$E_\pm = \pm\Delta\sqrt{1 - \tau \sin^2(\phi/2)} \tag{3.21}$$

Since charge and phase are conjugate elements in a Josephson junction, the current through the junction goes as $I_s = \frac{\partial E}{\partial \phi}$, so the total current through a ballistic S-N-S junction is

$$I_S = \frac{2e}{\hbar} \sum_{\pm} \frac{\partial E_\pm}{\partial \phi} \tanh\left(\frac{E_\pm}{2k_B T}\right) = \frac{e\Delta^2}{2\hbar} \frac{\tau \sin(\phi)}{E_+(\phi)} \tanh\left(\frac{E_+(\phi)}{2k_B T}\right) \tag{3.22}$$

In the limit of low transparency $\tau << 1$, the Ambekagaor-Baratoff [110] relation is recovered

$$I_S \approx \frac{\pi\Delta}{2eR_N} \tanh\left(\frac{\Delta}{2k_B T}\right) \sin(\phi) = I_c(T) \sin(\phi) \tag{3.23}$$

where we see that the temperature dependence of the critical current arises from the thermal filling of the Andreev bound states. For longer junctions, more states (including states above the gap) contribute to the current, and more sophisticated mathematical tools are required, yielding a more complex temperature dependence of the critical current [35, 46].

3.2 Graphene Background

Heat Capacity of an Electron Gas

A simple argument for electronic heat capacity in a solid state system is given by Kittel [60]. In a classical monoatomic gas in, suppose, three dimensions, each atom is endowed with three degrees of freedom. This means that each atom should have a heat capacity $\frac{3}{2}k_B$, and since each atom is independent of all the others, the total heat capacity of an N-atom classical gas is

$$C_{classical} \approx N \times \frac{3}{2}k_B \tag{3.24}$$

However, early researchers found that the heat capacity of an electron gas is much smaller than this, often at the level of 1% of the classically-predicted value.

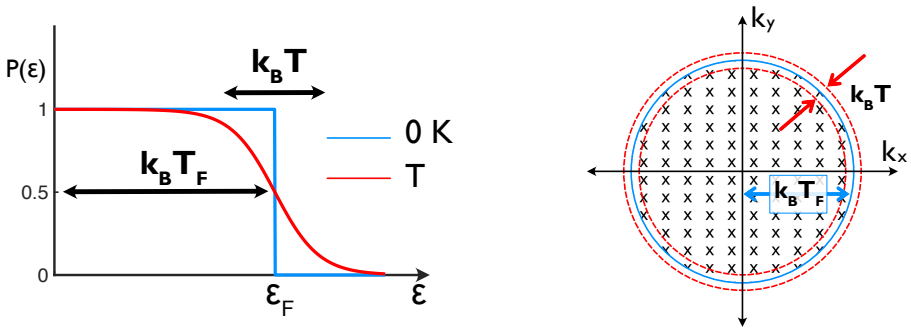

Figure 3.3: **Thermal Excitations of a Fermi Electron Gas**. (**left**) Fermi-Dirac Distribution. At $T = 0$, the Fermi-Dirac distribution is brick-wall occupation function in which all electrons are at their lowest possible energies prescribed by Pauli repulsion. As the temperature is increased to a finite T, a smearing of the distribution occurs over a width k_BT. In other words, only those electrons with in a k_BT of the Fermi energy are thermal excited. (**right**) The Fermi Sea. This diagram is meant to demonstrate that only a small fraction of the total electrons in the Fermi sea are thermally excited, accounting for a suppression of C_{th} by a factor of $\frac{T}{T_F}$ relative to the classical case.

The reason for this discrepancy is that electrons, of course, are not classical particles. They are fermions which fill up a Fermi sea as their number increases. With the Fermi-Dirac distribution as our guide, increasing the temperature of the electron gas from 0 Kelvin to some finite temperature T smears the Fermi distribution by an amount k_BT. In other words, only those electrons within a k_BT of the Fermi surface are involved in the absorption of thermal energy This can be a very small fraction of the total electrons, $\sim \frac{T}{T_F}$. Thus, we can write the heat capacity of an electron gas

$$C_{th} \approx N k_B \frac{T}{T_F} \tag{3.25}$$

up to numerical factors, where we see that the suppression by the factor $\frac{T}{T_F}$ accounts for the diminished heat capacity of an electron gas. We also see the important result that the electronic heat capacity scales linearly in T, even down to 0 Kelvin. This linear T scaling implies that the electronic heat capacity typically dominates at low temperatures over the phonon heat capacity, which typically scales as T^2 or T^3 depending on the thermal phonon dimension, or the heat capacity of the superconducting leads, which is exponentially suppressed $C_{th} \sim e^{-\Delta/k_B T}$. Roukes [96] shows this predicted scaling for a suspended nanostructure, as shown in Fig. 3.4.

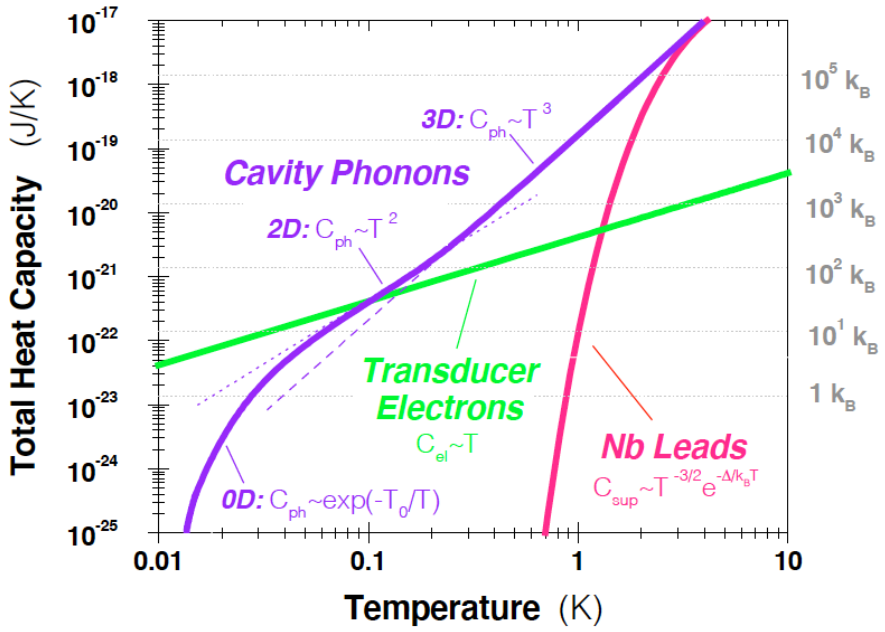

Figure 3.4: **Heat Capacity C_{th} Scaling with Temperature in a Suspended Nanostructure, from Roukes [96]**. In the case of an electron gas on a suspended nanostructure with galvanic contact via superconducting leads, Roukes considered the relative contributions to the total heat capacity. At low temperatures, the electronic heat capacity, which scales as $\sim T$ typically dominates over the other sources of heat capacity, which possess a stronger temperature scaling. Due to the energy gap between the ground state and the excited states, the heat capacity of the superconducting leads are exponentially suppressed as $\sim e^{-\Delta/k_B T}$. Since the phononic contributions to the heat capacity go as the dimensionality of the phonons, with freeze-out occurring when the phonon wavelength exceeds the device size.

An alternative derivation can be given by the Sommerfeld expansion of the Fermi-Dirac distribution in the limit of small temperature [6]. We briefly quote the result that the Sommerfeld approximation expands the Fermi Dirac distribution to zero-th order in T as a step function with step at E_F, and higher order terms in T^{2n}. With these assumptions the electorn gas energy is given by

$$U = E_F + \frac{\pi^2}{6}(k_B T)^2 g(E_F) \tag{3.26}$$

where E_F is the Fermi energy and the lowest-order expansion term scales as T^2 where $g(E_F) = \frac{\partial N}{\partial E}\Big|_{E_F}$ is the density of states at the Fermi level. We note that N comes in units of number.

Taking temperature derivative to obtain the heat capacity

$$C_{th} = \frac{\pi^2}{3} k_B^2 T g(E_F) \tag{3.27}$$

where once again we have shown the linear-T scaling of the electronic heat capacity.

Heat Capacity of a Graphene 2DEG

Our focus now turns to calculating the two-dimensional electron gas heat capacity for two different types of band structures, graphene's linear band structure and a standard parabolic band structure such as might be found in a InAs quantum well. The two types of band structures share many similarities, in the sense that they both scale linearly in area A and temperature T, i.e. $C_{th} \propto AT$. We will see that the key difference between the heat capacities of these two solid-state systems is the dependence on carrier density n_A, with the parabolic band structure C_{th} possessing no dependence and the graphene possessing $C_{th} \propto \sqrt{n_A}$.

Heat Capacity of a 2DEG with a Parabolic Band Structure

Starting from the expression for heat capacity of a two-dimensional electron gas [60, 6]

$$C_{th} = \frac{\pi^2}{3} k_B^2 T \times \frac{dN}{dE_F}\Big|_{E_F} \tag{3.28}$$

where see that the density-of-states at the Fermi level $\frac{dN}{dE_F}|_{E_F}$ is key quantity which differentiates the heat capacity of different electron gases. The number of electrons can be determined from the phase-space product of the area A and the k-vector area πk_F^2, and numerical factors accounting for the phase-space volume and two-fold spin degeneracy

$$N = \frac{2}{(2\pi)^2} \times A \times \pi k_F^2 \tag{3.29}$$

In the case of a parabolic band structure $E = \frac{\hbar^2 k^2}{2m^*}$. This implies that

$$N = \frac{A}{2\pi} \frac{2m^*}{\hbar^2} E \tag{3.30}$$

$$\implies \left.\frac{dN}{dE}\right|_{E_F} = \frac{A}{2\pi} \frac{2m^*}{\hbar^2} \tag{3.31}$$

The surprising result here is that the density of states is *independent* of the carrier density, so we expect that the heat capacity C_{th} should also be independent of the carrier density. Indeed this is the case

$$C_{parabolic} = A \frac{\pi^2}{3} k_B^2 \frac{m^*}{\hbar^2} T \tag{3.32}$$

2DEG Heat Capacity for Graphene (Linear Band Structure)

For graphene, the linear band structure $E = \hbar v_F k$ ($v_F = 10^6$m/s) yields a different form of the density-of-states at the Fermi level [113, 115]. As before, we calculate the number of states from the phase-space product

$$N = \frac{4}{(2\pi)^2} \times A \times \pi k_F^2 \tag{3.33}$$

$$= \frac{A}{\pi} \frac{E^2}{\hbar^2 v_f^2} \tag{3.34}$$

$$\implies \frac{1}{A} \left.\frac{dN}{dE}\right|_{E_F} = \frac{2E_F}{\pi \hbar^2 v_F^2} \tag{3.35}$$

where the factor of 4 comes from the total degeneracy of graphene. Since $E_F \propto k_F = \sqrt{\pi n_A}$, where n_A is the number of carriers per area, we see that the density-of-states has a dependence on carrier density. The heat capacity of graphene then becomes

$$C_{th} = A\frac{2\pi^{3/2}}{3}k_B^2\frac{\sqrt{n_A}}{\hbar v_F}T \tag{3.36}$$

where we note that the primary effect of the linear band structure has been to introduce the $C_{graphene} \propto \sqrt{n_A}$ dependence. Thus, in contrast to 2DEGs with a parabolic band structure, the heat capacity of the graphene 2DEG can be varied by changing the carrier density.

As a rule of thumb, a 2DEG with parabolic band structure (of any carrier density) with $m^* \approx 0.05m_e$, area $A \approx 1\mu m^2$, and temperature $T = 100$ mK has a heat capacity of $C_{parabolic} \approx 18\,k_B$. By contrast a graphene flake of size $A = 1\mu m^2$, carrier density $n_A = 10^{12}/\text{cm}^2$, and temperature $T = 100$mK has a heat capacity of $C_{graphene} \approx 4.6\,k_B$, and scales with $\sqrt{n_A}$. Thus, decreasing carrier density to $\sqrt{n_A} = 10^{11}/\text{cm}^2$ will decrease the graphene heat capacity to $\sim 1.5k_B$. From Walsh et al. [115], the heat capacity of a graphene flake is plotted in Fig. 3.5 with its corresponding energy resolution $\Delta E/h$. In the latter, it is assumed that the measurement bandwidth is limited by the thermal time constant τ_{th}. This is not a fundamental bound, as derived in section 2.4.

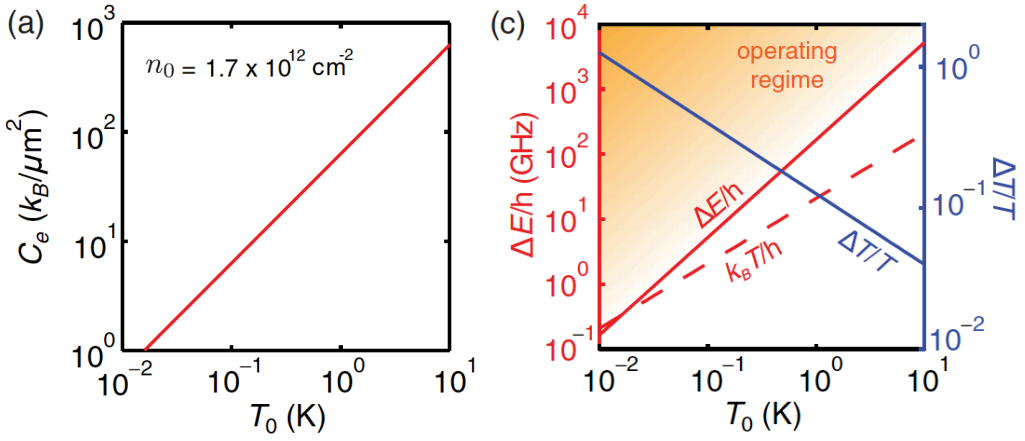

Figure 3.5: **Projected Thermal Detector Specifications for a graphene 2DEG, from Walsh et al. [115].** (**left**) C_{th} vs. Flake Temperature for a graphene 2DEG. For temperatures below 100 mK, it should be possible to achieve heat capacities below $10k_B$, where the C_{th} can be further reduced by shrinking the flake area A, reducing the carrier density n_A, or lowering the flake temperature T. (**right**) Energy resolution vs. Flake Temperature for a graphene 2DEG. It is assumed that the energy resolution of graphane 2DEG operated as a thermal detector is limited by a measurement bandwidth set by the thermal roll-off τ_{th}.

3.3 Resistively- and Capacitively-Shunted Junction (RCSJ) Model

The key model for DC and RF response of a Josephson junction is the resistively- and capacitively-shunted junction (RCSJ) model, in which the junction is in parallel with a lumped-elemenet resistor and a lumped-element capacitor [110, 112]. The resistive branch accounts for normal losses and the capacitive branch accounts for the capacitive coupling between the superconducting leads. Accounting for the Josephson equation for current and the standard voltage drops across a resistor and capacitor, the equations of motion for this model are as follows:

$$C\frac{dV}{dt} + \frac{V}{R} + I_c \sin(\varphi) = I \tag{3.37}$$

Due to the Josephson relation for voltage, $V = \phi_0 \frac{d\varphi}{dt}$ for $\phi_0 = \hbar/2e$, we can convert the above equation into one solely in terms of derivatives of the phase φ and the bias current I, where the former is the dynamical variable and the latter in the forcing term

$$\frac{d^2\varphi}{d\tau^2} + \frac{1}{Q}\frac{d\varphi}{d\tau} + \sin(\varphi) = I/I_c \tag{3.38}$$

where we have introduced the characteristic (plasma) frequency $\omega_p = \sqrt{\frac{2eI_c}{\hbar C}}$, quality factor $Q = \omega_p RC$, and scaled time as $\tau = \omega_p t$. These equations describe a particle moving in a washboard-like potential

$$U(\varphi) = -E_J \cos(\varphi) - \phi_0 I\varphi \tag{3.39}$$

In which the capacitance C controls the inertia (acceleration term) of φ, the resistance R controls the damping, and applying a bias current I amounts to tilting the washboard potential. For DC $I \leq I_c$, there exist regions in which the phase may be stationary, and thus the voltage is be zero. This corresponds to the superconducting regime. For $I > I_c$, there exist no regions in which the phase can be stationary, so velocity of the particle will always be non-zero. This is known as the free-running, or normal, state, and it corresponds to the junction developing a non-zero voltage drop.

For I slightly below I_c, the particle can be excited over the potential maximum, either by thermal excitation or quantum mechanical tunneling. This excitation produces a variance about the mean switching current, as in 3.7.

For SNS junctions, the capacitance is typically low (<pF) and the inertial term may be disregarded. Thus, the equations of motion describe an overdamped particle in a washboard potential, in which the velocity of the particle is solely determined by the slope of the potential at a given instant.

$$\frac{d\varphi}{dt} = \frac{2eI_cR}{\hbar}\left(\frac{I}{I_c} - \sin(\varphi)\right) \tag{3.40}$$

If a time-dependent bias current $I(t)$ is applied, the Josephson voltage and current relations conspires to produce an effective inductance. Implicit in this description is the assumption that the current source has a much larger impedance than the junction, which is typically the case for a 50 Ω measurement circuit and a 1Ω graphene Josephson junction. Differentiating the Josephson current relation, we find

$$I(t) = I_c \sin(\varphi(t)) \tag{3.41}$$

$$\frac{dI}{dt} = I_c \cos(\varphi)\frac{d\varphi}{dt} \tag{3.42}$$

We can scale this equation by ϕ_0 to relate voltage to the time-derivative of the bias current

$$V = \frac{\phi_0}{I_c \cos(\varphi)}\frac{dI}{dt} \tag{3.43}$$

$$L_J = \frac{\phi_0}{I_c \cos(\varphi)} = \frac{\phi_0}{I_c\sqrt{1-(I/I_c)^2}} \tag{3.44}$$

$$\approx \frac{\phi_0}{I_c} \tag{3.45}$$

where the final expression holds in the limit of $I << I_c$, implying that the junction state is deep within a well of the RCSJ model and executes oscillations about the well minimum [78]. Clearly, as the bias current increases, higher order nonlinear terms will contribute to the Josephson inductance.

3.4 Cryogenic Graphene Thermal Detectors

In this section, we give a brief overview of some recent cryogenic graphene detectors and important techniques used to perform temperature readout which often rely upon the cryogenic or superconducting phenomena discussed earlier in this chapter.

Resistive Readout

The temperature-dependence of the resistance $R(T)$ can be used to monitor the temperature of a graphene flake, where the resistance can be measured in a four-wire IV measurement [123]. However, since the resistance of graphene (as with many solid-state systems) saturates at sub-Kelvin temperatures, this technique is typically limited to liquid helium temperatures and above. Further, the four-wire measurement requires sourcing a normal current through a normal resistance, which dissipates $P = I^2R$ to the graphene flake. At sub-Kelvin temperatures, this typically heats the electrons of the graphene far above the fridge temperature, making it unsuitable for operating the graphene flake at the 100 mK-level required for calorimetry of low-GHz photons.

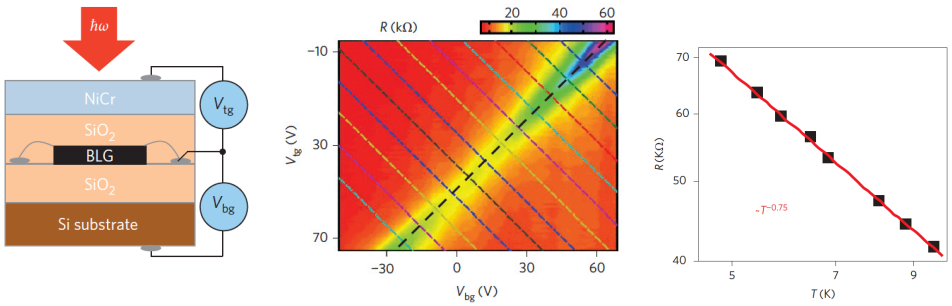

Figure 3.6: **Resistive Readout of Dual-Bilayer Gated Graphene Flake Temperature at 5K, from Yan et al. [123]**. **a.** A bilayer graphene sample is gated with a global top gate and bottom gate. **b.** A heat map of the resistance is shown as function of top gate and bottom gate. **c.** The temperature-dependent resistance $R(T)$ is shown down to 5K.

Noise Thermometry

A suitable technique for cryogenic measurement of the graphene electronic temperature is Johnson noise thermometry, as demonstrated first by Fong and Schwab [39] and Fong et al. [40] and subsequently by many others [36]. This technique is described in greater detail in Chapter 7.3, both for normal metals and graphene at cryogenic temperatures.

In Johnson noise thermometry[31], the Johnson noise fluctuations of a lumped-element resistance are amplified and directly measured. Since the noise comes in units of $k_B T$, it is a form of primary thermometry in that it does not, in principle, require a calibration to an additional temperature standard. For this reason, Johnson noise thermometry is often considered to be a 'gold-standard' technique for performing thermometry, especially on cryogenic solid-state systems.

For graphene, Johnson noise thermometry typically requires an impedance match between the (usually) high resistance of the graphene flake and a 50 Ohm measurement circuit. For this reason. Fong and Schwab used a NbTiN tank resonator circuit with resonant frequency 1.16 GHz and bandwidth of 80 MHz, to impedance match a 30 kΩ region of a graphene flake to their 50 Ω measurement circuit, with a $T_N = 4K$ cryo-HEMT as the front-end amplifier.

Unfortunately, due to system noise, the temperature range of their measurement was limited to temperatures in excess of 2K, though this limit can be circumvented by using a quantum noise-limited front-end amplifier, such as a Josephson parametric

amplifier, a traveling-wave parametric amplifier, or a SQUID amplifier [29, 97].

Graphene Josephson Junction Switching Detectors

Due to the mechanism of Andreev reflection, we expect a temperature-dependence of the supercurrent which flows through a graphene Josephson junction [69, 115, 34, 95, 114, 17, 124, 16, 59, 66, 70, 90, 33, 52, 55, 71, 37]. Since this temperature-dependence often persists down to the level of 100 mK before saturating, it can be used to measure temperature changes of the graphene flake down to the preferred level for using a graphene flake as a thermal detector of sub-10 GHz microwave photons.

A particularly straightforward way of measuring the supercurrent is by four-wire I-V measurements, in which the bias current I_B is ramped through the scale of the critical current I_c and the resulting voltage drop is measured across the junction. For $I_B < I_c$, the junction will remain in its supercurrent state and there will be no voltage drop. However, once the bias current exceeds a given threshold value known as the switching current I_S, the junction switches normal and a non-zero voltage drop develops across the junction. Usually, the switching current is close to the value of the critical current I_c, though various experimental considerations can suppress it, such as the speed of the bias sweep. In the RCSJ model, increasing the bias current corresponds to increasing the tilt of the washboard potential until the particle transitions from the stationary (superconducting) state to the free-running (normalconducting) state. Figure 3.7 shows an example of the temperature dependence of the mean value of the switching current, where it is evident that this technique maintains temperature sensitivity down to ~200 mK.

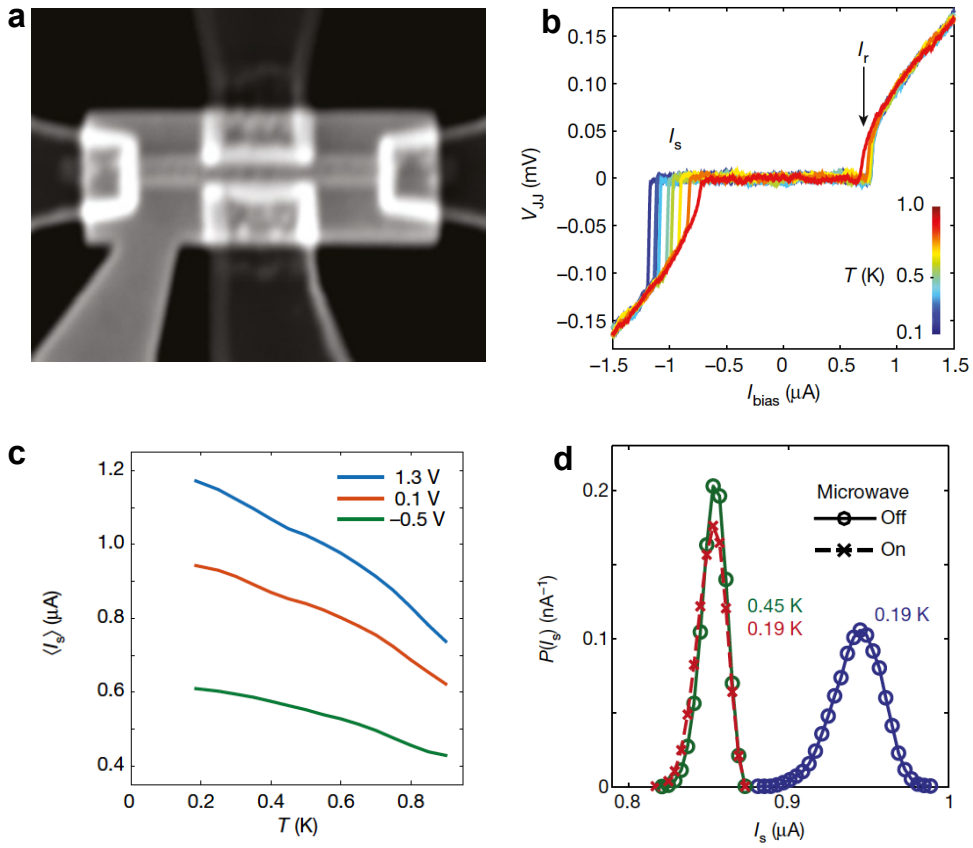

Figure 3.7: **Graphene Josephson Junction Switching Detector, from Lee et al. [69] a.** SEM image of a graphene Josephson Junction. The graphene flake is the long, thin the center of the image surrounded by four contacts and a gate to control carrier density. The contacts are composed of edge-contacted NbN superconductors, where the contacts at the top and bottom of the image comprise the Josephson junction leads, and the contacts at the left and right of the image comprise the heater leads. **b.** IV curve of the graphene Josephson Junction. The zero-voltage supercurrent region has a maximum value $Is(T)$ of the switching current which demonstrates a clear temperature dependence. There is a clear hysteresis in the IV curve between the positive and negative bias due the positive-to-negative I_{bias} sweep direction, where Joule heating of the flake in the normal regime suppresses the retrapping current I_r relative to the switching current I_s. **c.** Temperature dependence of the average switching current. Clearly, the switching current exhibits a temperature dependence down to 200 mK, which allows operation of the threshold detector down to these temperatures. **d.** Switching probability of I_s. Variance of the switching current $\sigma^2_{I_S}$ about the mean value $\langle I_s \rangle$ can be explained in the RCSJ model either by thermal excitation or macroscopic quantum tunnelling.

The relevant uncertainty in this measurement typically appears as a variance about $\langle I_s \rangle$ the mean value of the switching current. As stated previously, this can be modeled as the escape of the particle over the barrier, either due to thermal excitation or macroscopic quantum tunneling [115].

A bare Josephson junction integrated into a graphene flake can be operated as a threshold detector, in the following sense. A particular bias current I can be chosen, where $I < I_s$. In the event of absorption of radiation, the flake temperature will increase, the temperature-dependent switching current will be suppressed, and the junction will switch normal when $I > I_s$. This registers that the incoming radiation was above a given threshold value.

As discussed in section 8, a linear detector in the small-signal regime will output a signal proportional to its input signal. In this case, the noise equivalent power can be straightforwardly defined as the noise spectral density measured at the output referred to the input of the detector for a 1 Hz measurement bandwidth. In the case of a threshold detector, however, the noise equivalent power is much less straightforward to define or interpret. Lee et. al. calculated an NEP-like metric of their threshold detector, which they define as

$$NEP_{Lee} = P_{min}/\sqrt{BW} \tag{3.46}$$

where P_{min} is the minimum resolvable input power due to the measured standard deviation of the switching current and BW is an estimated measurement bandwidth.

When applied to a linear detector, this metric is well-defined. Suppose there is a steady-state signal P at a particular frequency in the presence of the noise spectral density NEP (in units of $W/\sqrt{Hz}$). In this case, we can ask for the total integrated noise signal, and subsequently, the signal-to-noise ratio.

Assuming the noise spectral density in each unit bandwidth is uncorrelated (true for white noise), each channel of bandwidth provides an independent contribution to the total integrated noise. Thus, the total integrated rms noise is $\sigma_P = \sqrt{NEP^2 \times BW} = NEP \times \sqrt{BW}$, where we have assumed that the NEP is constant over the bandwidth of interest. Now, we can define the minimum resolvable power P_{min} as that signal power which will produce a signal-to-noise ratio of unity

$$1 = \frac{P_{min}}{\sigma_P} = \frac{P_{min}}{NEP \times \sqrt{BW}} \implies P_{min} = NEP \times \sqrt{BW} \tag{3.47}$$

where we see that shrinking the measurement bandwidth BW reduces the number of independent noise contributions and, correspondingly, decreases the minimum resolvable power P_{min}, i.e. makes the detector more sensitive. As in lock-in detection [72], we see it is advantageous to employ the narrowest integration bandwidth BW possible in order to minimize the added noise. From this discussion, we see that this figure-of-merit is well-defined in the case of a steady-state signal in the presence of a noise spectral density.

However, in the case of a threshold detector, there exists neither a steady-state signal nor a steady-state noise spectral density. Instead, each sweep of the bias current produces one measurement of the switching current I_s. Considering the RCSJ model at the bias point just below junction switching (in other words, for large tilt of the washboard potential), the fundamental uncertainty of this measurement arises from the stochastic escape of the phase particle over a potential barrier, either by thermal activation or quantum tunneling. The stochasticity of this particle escape yields an uncertainty in I_s, which can be seen from the measured standard deviation σ_s about the mean switching current $\langle I_s \rangle$. This is a fundamental uncertainty, but it arises from a different measurement technique than the steady-state signal in the presence of a noise spectral density.

It would be more appropriate to simply use the measured P_{min} (the uncertainty in the switching current σ_s referred to the input of their power detector) as the figure-of-merit for their threshold detector, in analogy to using timing jitter to quantify the uncertainty of a superconducting nanowire single photon detector (SNSPD), another type of threshold detector [86]. The timing jitter quantifies the timing uncertainty between the arrival of a photon and the voltage pulse arising from the switching of the detector from its superconducting to normalconducting states. Practically, it can be defined as the FWHM of the Gaussian envelope of the delay time between the photon arrival and measured voltage pulse.

As a brief aside, we also note that while Lee et. al. claim a measurement bandwidth limited by the dissipation time of the input heater signal to the flake ($BW \approx 790$ MHz), this particular measurement technique will have a measurement bandwidth limited by the repetition rate of the I-V sweep or the resetting time of the

junction from the normal state to the superconducting state. Both of these rates are substantially slower than the thermally-limited measurement bandwidth and degrade the sensitivity of their defined metric.

We direct the reader to chapter 8 to see how the noise-equivalent power can be measured in a linear detector composed of a resonantly-coupled graphene Josephson junction.

Resonant Readout of Graphene-based Josephson Junctions

In the interest of increasing the measurement bandwidth to the level in which it is possible to resolve individual thermal events, we turn to understanding how a graphene flake can be coupled to a superconducting resonator for the purpose of fast monitoring of the graphene flake temperature. Ultimately, this readout mechanism may allow for straightforward frequency-division multiplexing of many thermal graphene detectors on a single microwave line.

Microwave Kinetic Inductance Detectors

The microwave kinetic inductance detector (MKID) has been a key enabling technology for precision astronomical detection and multiplexed readout [28, 127, 80, 42]. Here, we discuss the fundamental mechanism for device operation with the goal of demonstrating how this detector inspired the temperature readout mechanism of the device architecture presented later in this thesis.

Energy from an applied AC signal can be stored in the kinetic energy of Cooper pairs. The reactive (non-dissipative) energy flow between electromagnetic field and superconductor produces an effective surface inductance L_s, with length-scale set by the penetration depth λ into the superconductor. At temperatures far below the superconducting transition temperature $T << T_c$, the electrical impedance of the film is dominated by this so-called 'kinetic inductance', rather than by resistive quasiparticle losses.

When pair-breaking radiation ($h\nu > 2\Delta$) is absorbed by the superconductor, Cooper-pairs are broken apart into quasiparticles. This results in a shift of the surface inductance, with an estimate of the fractional change in the surface inductance given by

$$\frac{\delta L_s}{L_s} = \frac{\delta n_{qp}}{2N_0\Delta} \tag{3.48}$$

for n_{qp} the quasiparticle density, N_0 the single spin density of states at the Fermi level, and $N_0\Delta$ the density of Cooper pairs. To exploit this property of superconducting films for detection purposes, the superconductor can be patterned into a transmission line resonator, so that shifts in the surface inductance resulting from the absorption of pair-breaking radiation can be transduced into shifts of a resonant frequency that can be monitored by microwave reflectometry.

A microwave resonator loading a feedline (measurement line) has the important property that the electrical loading depends on the frequency of a microwave tone propagating down the feedline [75], allowing for straightforward frequency-division multiplexing. To illustrate, suppose an applied microwave signal has frequency within the linewidth of the resonance. In this case, the resonator will electrically load the line and scatter the signal. Since the phase and magnitude of the transmitted signal will shift when the resonant frequency shifts, the scattered signal can be used as a measure of the shift of the surface inductance, and therefore, as a measure of the incoming pair-breaking radiation. If the microwave signal has frequency outside of the linewidth of the resonance, the impedance of the resonator will be much larger than that of the 50 Ω line, and the signal will pass by without scattering. Provided that many microwave tones can be sent down the feedline simultaneously and provided that each resonance is spaced into non-overlapping regions of frequency space, an array of MKIDs to be individually and simultaneously addressed, with readout occurring with a single wideband cryogenic amplifier.

This remarkable technology has driven much progress in superconducting astronomical instrumentation over the last two decades. For example, recent demonstrations of microwave kinetic inductance detectors include 20 kilopixel frequency-multiplexed arrays, noise equivalent powers of $1 \times 10^{-19} W/\sqrt{Hz}$, and a variety of applications including precise triangulation of phonon emission events from high-energy particle collision [84]. Buoyed by the success of this device architecture, especially its capability to easily multiplex many devices on a single feedline, other detectors have been designed to incorporate resonant readout. For example, thermal KIDs (TKIDs) have been designed to serve as a drop-in replacements for TES bolometers, obviating the need for costly and complex time-domain multiplexing SQUID chips [116].

However, the need to break Cooper pairs places fundamental limits on the KID photon energy resolution, with typical MKID operation in the near IR and up. Pushing single-shot photon resolution below the IR will require a fundamentally new

detection mechanism. For this reason, other groups (including ours) have pushed to combine the benefits of resonant readout as discussed here with temperature-sensitive elements such as graphene flakes capable of pushing photon resolution to the level of the low-GHz regime.

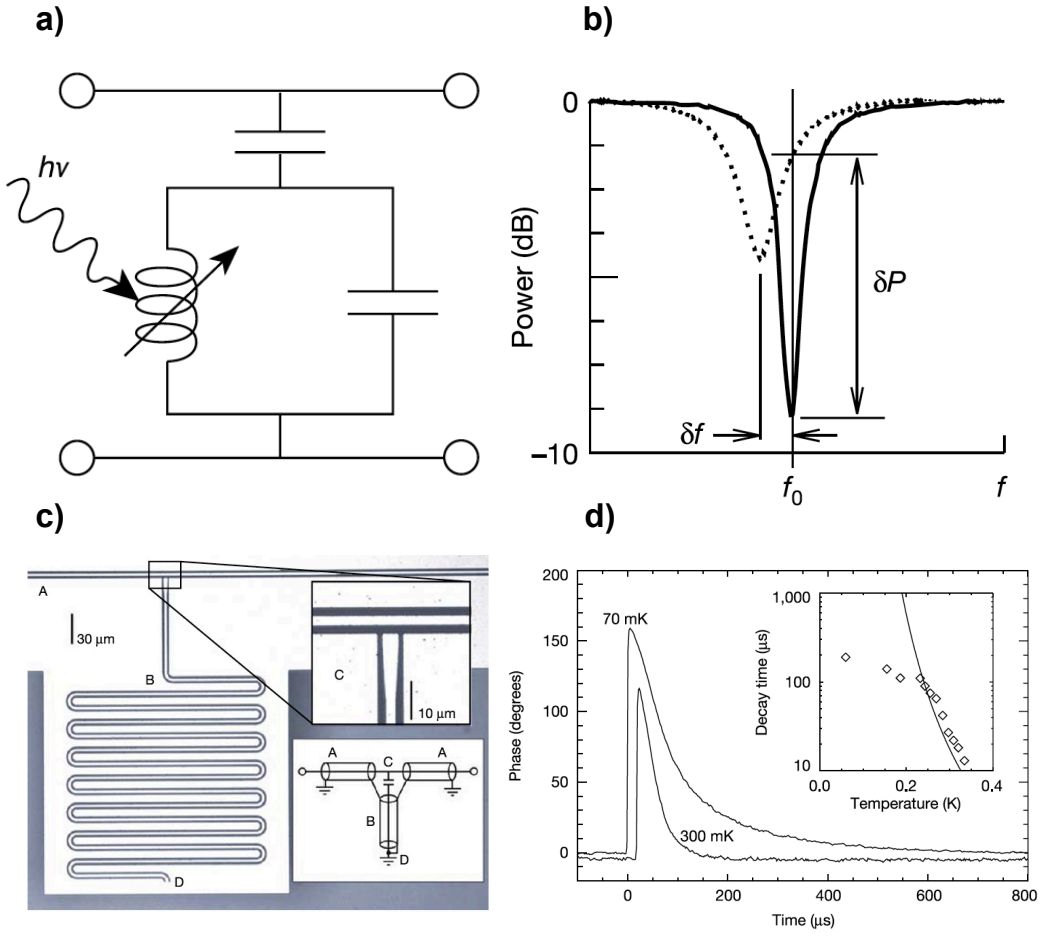

Figure 3.8: **A Brief Introduction to MKIDs (borrowed with permission from Day et al. [28]). a. Detection Principle of an MKID.** Pair breaking radiation ($h\nu > 2\Delta$) breaks Cooper pairs, alters the surface inductance of the superconducting film, and shifts the resonant frequency of the resonantor. **b. Resonant Frequency Shift.** Accompanying the absorption of radiation, the resonant frequency and quality factor shift. This shift can be monitored by the scattering of a microwave tone at a frequency within the linewidth of the resonance. Tones outside the linewidth will not be scattered. **c. Top-down Image of Superconducting Resonator.** Example of a CPW-style quarter-wavelength resonator patterned from superconducting aluminum on a sapphire substrate. **d. Absorption of an X-ray photon.** Phase the transmitted scattered signal upon absorption of an X-ray photon.

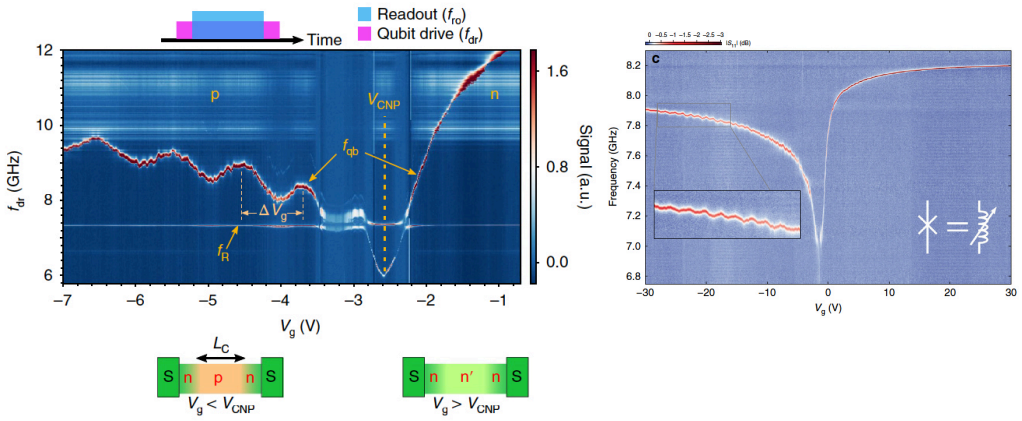

Figure 3.9: **Resonantly-coupled Graphene Josephson Junction Qubits (from Wang et al. [117] and Schmidt et al. [101]). (left)** In their graphene JJ/microwave circuit, [117] show resonance tuning over a range of 6-12 GHz and p-n-p Fabry-Perot type oscillations with an effective Fabry-Perot cavity length of L_c = 110nm **(right)** Schmidt et al. [101] show resonance tuning over a range of 6.8-8.2 GHz and Fabry-Perot type oscillations in a cavity length of L_c = 390nm.

In recent years, there has been growing interest in using voltage biases to control qubits in order to reduce the stray electromagnetic fields endemic in current-based control of superconducting qubits. This style of 'gatemon' qubit typically involves coupling a superconducting resonator to a Josephson junction integrated into a semiconductor or Van-der-Waals heterostructure.

Toward the goal of developing voltage-tunable transmon qubits, Wang et. al. and Schmidt et. al. have demonstrated superconducting resonator-VdW structures, with Wang et. al. demonstrated coherent behavior in the strong-coupling regime. Their resonantly-coupled graphene devices are exceedingly similar to the one presented in this thesis, though they are primarily interested in using the voltage-tunable supercurrent to realize control of their qubit.

As shown in Figure 3.9, both groups observe Fabry-Perot-type oscillations resulting from the propagation of ballistic carriers in a p-n-p junction, with Wang estimating an $L_c \approx 110$ nm cavity length (excluding the doping length about the contacts) and Schmidt demonstrating a cavity length of $L_c \approx 390$ nm. As expected, the substantial tunablity of the Josephson current yields tuning of the resonant frequency, with Wang demonstrating tuning over a range of 6 to 12 GHz and Schmidt demonstrating tuning

from 6.8 to 8.2 GHz.

From standard qubit measurements of energy relaxation and dephasing, Wang demonstrated an energy relaxation coherence time $T_1 \approx 36$ns and a dephasing time $T_2^* \approx 55$ns. It is suggested that a limiting source of these coherence time is the capacitive coupling between the shunt capacitance and backgate, which can be alleviated by a redesign of the geometric capacitance in future generations of these devices.

Resonantly-Coupled Graphene Josephson Junction Thermal Detector

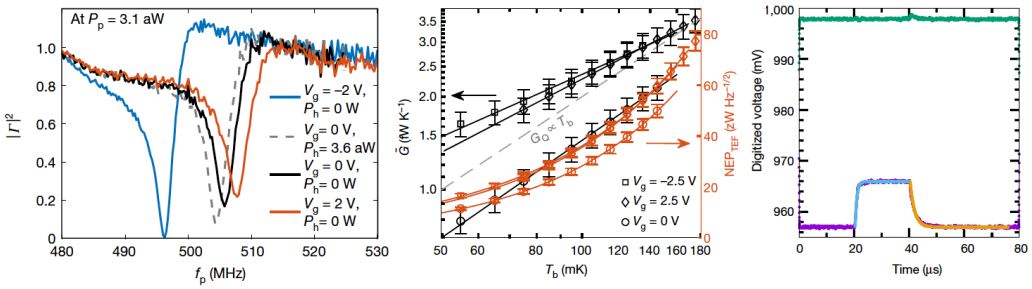

Figure 3.10: **Bolometer Operating at the Threshold of QCD, from Kokkoniemi et al. [63]. a.** Examples of resonance position at different backgate voltages and applied powers. **b.** Differential thermal conductance G and measured NEP as a function of bath temperature T_b. **c.** Time trace showing device response for quick turn-on and turn-off of applied power. Exponential fits determine rising and falling time constants.

Kokkoniemi et al. [63] demonstrated a resonantly-coupled graphene Josephson junction which performed temperature readout of the graphene flake. Their thermal absorber consisted of graphene-on-SiO_2 where the inductance of the graphene Josephson junction was integrated with lumped-element capacitors to form a resonant circuit. In this setup, heating and readout were performed on the same microwave line, which required estimation of absorbed heat power to the flake from estimates of the signal attenuation and measurements of the transmitted signal. It would be useful in future iterations of this experiment to perform heating via a 4-wire measurement where the applied heat power can be precisely measured. In this thesis, we present an example of such a device architecture with this capability.

Their SiO_2-stamped graphene flake demonstrated excellent thermal properties, such as measured noise equivalent power down to the level of 10 $zW/\sqrt{Hz}$ and very small

Gth at the level of 1 fW/K. Due to this small thermal coupling to the environment, the device demonstrated a minimum resolvable thermal time constant of $\tau = 200$ ns, which implies the ability to resolve 30 GHz photons.

Excitingly, this result demonstrates the viability of using a resonantly-coupled graphene flake as a low-C_{th} thermal detector for microwave photons. It remains to be seen which properties of such a VdW material stack will increase the yield of such detectors, and astronomical detection efforts will focus on whether this design can be implemented via top-down lithography and associated nanofabrication techniques in order to scale up to production of detector arrays.

3.5 Applications of Ultrasensitive Calorimetry: Measurement of the Landauer Limit

An interesting application of a cryogenic calorimeter operating at single-k_BT energy resolution is the direct measurement of the *Landauer limit*, the heat dissipation associated with the erasure of a classical bit. We give a brief pedagogical introduction to Landauer erasure and briefly review the associated theoretical and experimental literature.

In 1961, Rolf Landauer [68] postulated that the erasure of a classical bit should be accompanied by a fundamental minimum heat dissipation to the local environment. This postulate emerged from considerations of two different types of entropy. The first type, Shannon entropy [105], is an information-theoretic metric defined for a logic element with states i occupied with probability p_i. It is defined as

$$\langle S \rangle = -k_B \sum_i p_i \log(p_i) \tag{3.49}$$

If a classical bit (two-state logic element) can be in either state with equal probability, then the corresponding Shannon entropy of the classical bit is

$$\langle S \rangle = k_B \log(2) \tag{3.50}$$

When the bit undergoes an irreverible erasure, it is forced into only one of the two possible states, so its Shannon entropy vanishes, i.e. $\langle S \rangle = 0$. Thus, the erasure of a classical bit is accompanied by the reduction of Shannon entropy $\Delta S = -k_B \log(2)$,

where the sign refers to the fact that the erasure procedure reduces the Shannon entropy of the bit.

The second type of entropy considered by Landauer was thermodynamic entropy S_{thermo}, a fundamental state variable of thermodynamic systems that characterizes the number of accessible states [61]. Landauer suggested that there exists a real, measurable correspondence between these two types of entropy that preserves the second law of thermodynamics. Namely, the irreversible erasure of a classical bit, which reduces the Shannon entropy of the system by $\Delta S = -k_B \log(2)$, must be accompanied by a *minimum* increase in thermodynamic entropy by a corresponding amount $\Delta S_{thermo} = k_B \log(2)$. This increase in thermodynamic entropy is equivalent to the heat dissipation

$$\Delta Q = k_B T \log(2) \tag{3.51}$$

In this way, the reduction of Shannon entropy of the bit is compensated by an increased thermodynamic entropy to the local environment, and, thus, the second law of thermodynamics is not violated. We note that since, at any given moment, a single *classical* bit can occupy only one of its two states, an experimentalist would need to perform the erasure procedure many times or on several identically-initialized classical bits in order to measure the average quantity $\Delta Q = k_B T \log(2)$.

This result was celebrated as a resolution to the paradox of the Maxwell's demon, which supposes that an intelligent demon can rectify fluctuations of a thermodynamic system in such a way that it can perform thermodynamic work without an accompanying dissipation of thermodynamic heat. Several thought experiments utilizing such a demon have been presented, including Szilard's Engine [107] and Brillouin's torch [21]. The novelty of Landauer's postulate was in identifying the ultimate source of the dissipation in the erasure of the logic elements used by the demon to store information required to perform the rectification [10].

Experimentally, there has been growing interest in demonstrating Maxwell's demons [54, 12, 51, 91, 73, 62], or even using generalized Maxwell's demons to perform useful work [18, 19, 121, 20]. We shall detail one type of experiment here, though there are many others utilizing a variety of physical systems.

Bérut et al. [13] used a a laser trap to create a bistable well potential which traps a glass bead in an aqueous solution, shown in Fig. 3.11(left). The laser trap was

deformed in real time to realize an irreversible erasure protocol in which the bead was initialized in either well with equal probability and then forced into one of the two wells. Subsequently, a heat dissipation was associated with with this erasure protocol. Using a camera with a high-frame rate, the position of the bead was tracked and the velocity was determined at each time point. Assuming a particular dissipation function which depends on the velocity and integrating over the entire trajectory of the bead, a total dissipation was calculated and found to be consistent with the bound set by the Landauer limit.

This is a well-defined experiment with a clearly-defined erasure protocol and associated dissipation. However, its reliance upon an estimated loss function and its indirect estimation of the thermodynamic properties of the system based upon measurements of the dynamics of the system leaves room for a direct measurement of the thermodynamic itself. Roukes conceived of such an experiment, in which a logical element is integrated directly into a suspended cryogenic calorimeter, as shown in Fig. 3.11 (center) . This system should allow both an erasure protocol with high precision in a cryogenic logic element and the direct coupling of the logic element to a heat measurement device for direct measurement of the dissipated heat.

The erasure capability of this experiment was demonstrated by Saira et al. [99], using superconducting flux logic as realized with a flux qubit. The flux qubit, a parallel combination of back-to-back Josephson junctions (see Fig. 3.11c), realizes an underdamped bistable well potential where the dynamical variables are linear combinations of the superconducting junction phases. Independent control of the barrier height and tilt is achieved via external magnetic flux lines with DC and fast-pulse fluxes. The qubit is operated in a regime where the bistable well can be a continuously deformed from two isolated wells to a single global minimum, allowing for fast and precise implementation of the erasure protocol.

To determine the origin of environmental fluctuations (in particular, if they are of thermal origin), a time-domain pulse sequence is implemented in which the escape of the system from one well to the other is monitored with a DC SQUID magnetometer. Results shown in Fig. 3.11d indicate that the activation rate smoothly interpolates from being dominated by thermal fluctuations to being dominated by macrosopic quantum tunneling (MQT) with crossover occurring at $T_{mxc} \approx 100$ mK. Subsequent experiments are performed at $T_{mxc} \approx 500$ mK in order for the system to be well within the thermal fluctuation-dominated regime.

When implementing a control protocol to perform a Landauer erasure, the micro-

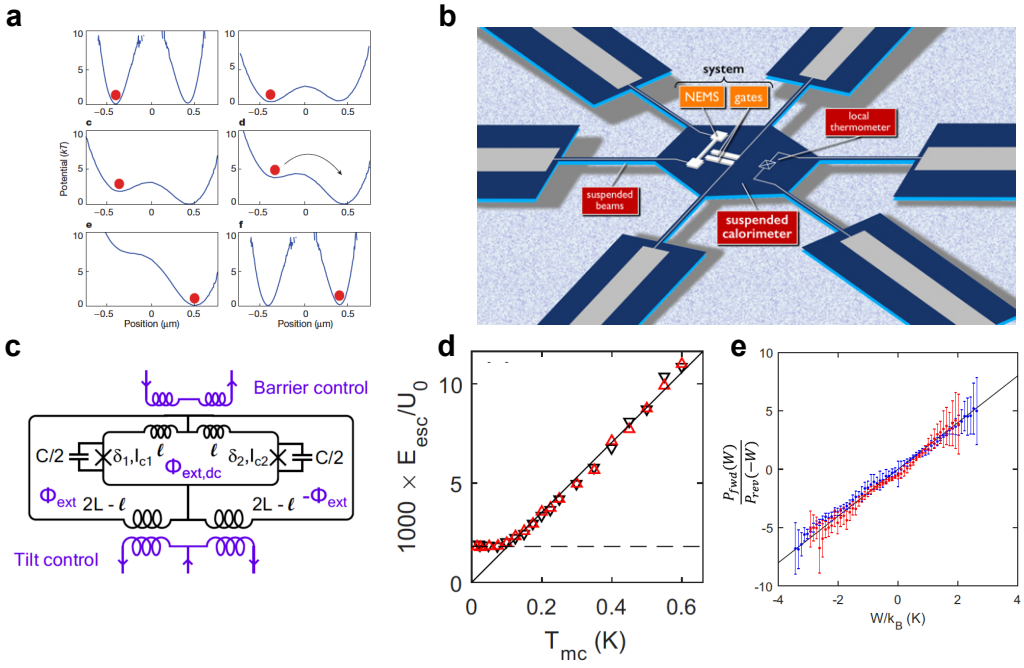

Figure 3.11: **Modern Landauer Erasure Experiments a.** Bistable potential realized by the laser trap, from Bérut et al. [13]. The erasure protocol allows the silica bead to start initially in either the left or the right well, but ensures that at the end of the procedure, the bead will only be on the right well. **b.** Schematic of a calorimetric measurement of the heat dissipation of a logical element. Here, the logic element takes the form of a nanoelectomechanical system (NEMS), though any controllable logic element will suffice. The logical element is integrated into a suspended low-C_{th} island, where local thermometry is performed to monitor the island's temperature. If $\Delta Q = k_B T \log(2)$ is dissipated locally in a control protocol upon the logic element, the suspended structure will have sufficient energy resolution and measurement bandwidth to resolve the associated temperature increase.**c** Impedance diagram of flux qubit, from Saira et al. [99] (along with d,e). Back-to-back Josephson junctions are shown, along with flux bias lines for controlling barrier height and tilt. **d** Activation rate vs. stage temperature shows crossover from thermal activation to macroscopic quantum tunneling (MQT) at $T_{mxc} \approx 100$ mK. **(e)** Probability ratios of trajectory-level work W for forward and reverse processes follows Crook's relation [27], as realized by a superconducting flux logic platform.

scopic work W integrated over the entire trajectory is determined from a summation of the potential differences as the system transitions from one potential well to the other. The erasure protocol can also be reversed by time-reversing both control channels. As seen in Fig. 3.11e, statistics of the microscopic work were found to be in agreement with the Crook's relation for work in microscopic systems [27], where

the ratio of the probability of the system absorbing work W during the forward and reversed protocols is given by the relation

$$\frac{P_{fwd}(W)}{P_{rev}(W)} = e^{W/k_BT} \tag{3.52}$$

Thus, it is apparent that the Landauer erasure protocol can be implemented, and the associated dynamics can be measured, using superconducting flux logic. The remainder of this thesis will discuss progress toward the complementary capability of pushing the limits of calorimetry toward the level of single-k_BT resolution.

We note that the postulated Landauer limit and Maxwell demon thought experiments are not without their criticisms [88, 87]. Critiques are leveled at selective inclusion and exclusion of thermal fluctuations at various stages of the demon protocol; at the notion of a reversible control procedure which, though valid in standard thermodynamic protocols, is argued not to hold at the molecular scales where the Maxwell's demon is relevant; and at the notion of a high-fidelity dissipationless control protocol, with some authors claiming that any physical procedure that reduces fluctuations with high probability comes at the cost of additional sources of dissipation that will ultimately defeat the Maxwell's demon. For theorists, a centralized response treating these critiques would be useful [11]. For experimentalists, the direct measurement of $\Delta Q = k_BT \log(2)$ accompanying the erasure of a classical bit would serve as gold-standard evidence for this postulate.

3.6 Conclusion

In this chapter we have

- First, we have discussed models for much of the superconducting phenomena which will be exploited in the rest of this thesis, including *Andreev reflection*-mediated supercurrent in S-N-S junctions and the RCSJ model of a Josephson junction.
- Second, we discussed how the heat capacities of cryogenic solid-state system can be substantially diminished relative to their classical counterparts, and we discussed advantages of using graphene's linear band structure toward this end.
- Third, we reviewed of some of the recent relevant graphene and related superconducting detectors in development.

- Finally, we review Landauer erasure pedagogy and recent experiments, including an implementation in superconducting flux logic.

With this background, reader should now be equipped to delve into the details of our cryogenic graphene-based thermal detector.

Chapter 4

MEASUREMENT SETUP

In this chapter, our goal is to describe the cryogenic and RF instrumentation with which we perform the measurements discussed in the subsequent chapters. We will perform the following:

- We will discuss the operation of a dilution refrigerator from first principles, including a rule-of-thumb expression for the cooling power of a standard fridge.
- We will discuss our cryogenic setup, which is primarily composed of a Blue-Fors LD400 dilution refrigerator.
- We will discuss the measurement setup used for microwave reflectometry and heating measurements of the graphene/resonator sample.
- We will discuss key RF components of the measurement setup, including the amplifier chain, sample boxes, and filtering.

When reading the subsequent chapters, the reader is encouraged to refer back to this chapter to review the measurement setup.

4.1 Principles of Dilution Refrigeration

The key physical concept behind a dilution refrigerator is that a particle in a particular state of matter has an associated energy. It follows that when the particle transitions from one state of matter to another, it must gain (or emit) the energy difference ΔE between being in the initial and final states. Often, we are interested in the case when there is an energy barrier, i.e. $\Delta E > 0$, and we ask for the transition rate between the initial and final states since this rate will set the cooling power of our refrigerator.

Classically, the energy to overcome the barrier typically comes from the thermal bath, and often we need only consider the relative sizes of ΔE and the thermal energy scale $k_B T$ to determine the likelihood of transition. As we will see, this

likelihood scales as the Boltzmann factor $e^{-\frac{\Delta E}{k_B T}}$, which means that the transition rate is exponentially suppressed as $T \to 0$ K.

However, for a quantum states of matter, important additional principles must be considered, such as Pauli repulsion, superfluidity, and zero-point motion. We will see that these additional phenomena alter the energy budget such that transitions from one quantum state to another can occur *even* at $T = 0$ K. This is the surprising result that underlies the design of a dilution refrigerator.

In the following, we first consider the case which is essentially classical and then consider the case which is essentially quantum.

Evaporative Cooling in the (Essentially) Classical Limit

In this section, we discuss how a vat of Helium-4 can be used to achieve evaporative cooling. We follow the treatment in Pobell [92].

Helium-4 has the remarkable property that its zero-point motion is so large that it does not condense into a solid at ambient pressure, even at $T = 0$ K. Thus, even down to $T = 0$ K, a vat of helium-4 will have two coexisting phases— liquid and gas— and helium-4 atoms will go from one phase to the other. The pressure in the gas phase when the liquid and gas phases are in equilibrium is called the *vapour pressure* denoted P_{vap}. We also assume that the vat is in good thermal contact with the helium-4, so that thermal energy can be exchanged and there exists a common temperature T.

If we apply a pump to the gas phase to remove helium-4 atoms at some rate, this will cause a continuous rate of liquid helium-4 atoms to cross the phase boundary into the gas phase to replenish the vapour. Then, we should expect cooling power associated with this net evaporation since each particle going from the liquid to the gas phase takes up some energy from the environment

$$Q = \dot{n} L \tag{4.1}$$

where Q is the cooling power, $\dot{n}$ is the rate of particles crossing the phase boundary and L is the energy-per-particle required to do so. Assuming the pump displaces a constant volume of the gas at a rate $\dot{V}$, we can write the cooling power as

$$Q = \frac{\dot{V} L}{RT} P(T) \propto P(T) \tag{4.2}$$

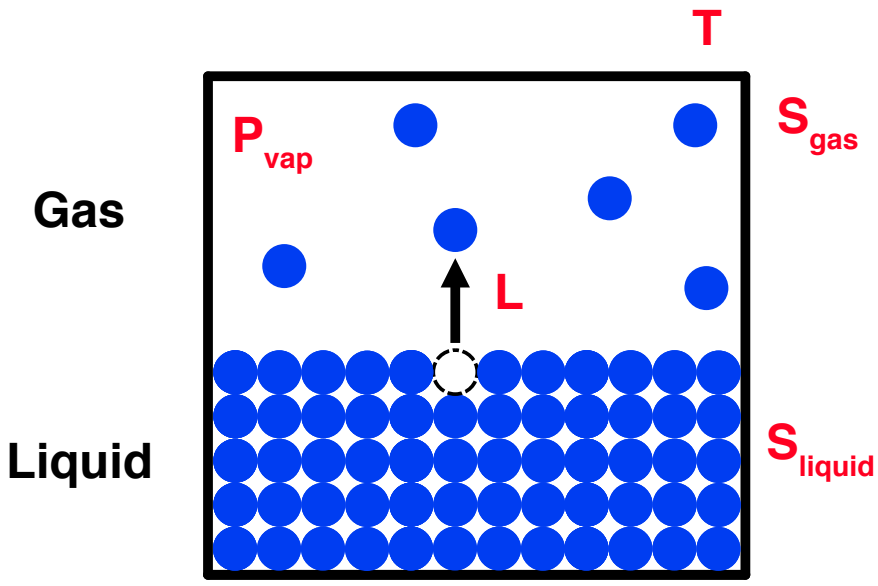

Figure 4.1: **Helium-4 Liquid-Gas Phase Coexistence**. A vat of helium-4 held at temperature T will have coexisting liquid and gas phases. The gas phase has an equilibrium vapour pressure P_{vap} and entropy S_{gas} and the liquid has entropy S_{liquid}. A He-4 atom can transition from the liquid to the gas phase upon absorption of latent heat $L = T(S_{gas} - S_{liquid})$.

We now seek the temperature dependence of the vapour pressure, $P(T)$. We will see that $P(T)$ is strongly dependent on T, so it will primarily determine the temperature dependence of Q.

In thermodynamics, it can be tricky to remember which quantities change and which are constant during a given process, so we review the assumptions for a first-order phase change.

For a closed system during a first-order phase change:

- Vapour pressure P_{vap} and temperature T do not change across the phase change, i.e. a phase change occurs at a exists a well-defined point in $P - T$ space. However, the vapour pressure P_{vap} *does* change with T, and it will trace out a line called in the *coexistence curve* situated at the boundary of the liquid and gases phases. It follows that we can define the derivative $\frac{dP}{dT}$ as the tangent to this curve (where we have dropped the vap label).

- Entropy S and volume V *do* change across the phase change. For the liquid-gas case, we can define $\Delta S = S_{gas} - S_{liquid} > 0$ and $\Delta V = V_{gas} - V_{liquid} > 0$.
- For a phase change, there will be a per-particle enthalpy $L = T\Delta S > 0$ (in units of Joules) which a particle will take up as it transitions from the liquid to the gas phase. We call L the *latent heat of vaporization* and note that it is weakly dependent on temperature, so we assume it to be constant.

From the Clausius-Clapeyron relation (or deriving from Maxwell's relations), we have the relation

$$\frac{dP}{dT} = \frac{\Delta S}{\Delta V} = \frac{S_{gas} - S_{liquid}}{V_{gas} - V_{liquid}} \tag{4.3}$$

which says that the slope of P relative to T at a given point on the $P-T$ coexistence curve can be determined by the per-particle (or per-mole) entropy difference relative to the volume difference across the phase change.

We can make the approximation that the molar volume of the gas is much greater than the molar volume of the liquid, so $V_{gas} - V_{liquid} \approx V_{gas} \approx \frac{RT}{P}$. Using the relation between the entropy difference ΔS and the latent heat of vaporization L, we then obtain

$$\frac{dP}{dT} = \frac{LP(T)}{RT^2} \tag{4.4}$$

$$\implies P(T) \propto e^{-L/RT} \tag{4.5}$$

which tells us that the pressure is exponentially suppressed as $T \to 0$. It follows that the cooling power has temperature dependence

$$Q \propto e^{-L/RT} \tag{4.6}$$

where the suppression of the cooling power arises from the fact that the rate of particles crossing the liquid-gas boundary is exponentially suppressed with $\frac{L}{k_B T}$. This is in agreement with our earlier discussion that the transition probability from the liquid to the gase phase should go as the Boltzmann factor $e^{-\frac{L}{k_B T}}$. This exponential

suppression has the consequence that the practical minimum temperature—that is, the temperature at which the heat load of the system equals the cooling power—is $T_{min} \approx 1.3$ K for helium-4. Thus, a different refrigerator design must be employed to access the milli-Kelvin temperature regime.

To review, although helium-4 is a liquid down to $T = 0$ K, evaporative cooling is exponentially suppressed at low temperatures due to the finite energy L required to promote a helium-4 atom from the liquid to the gas phase.

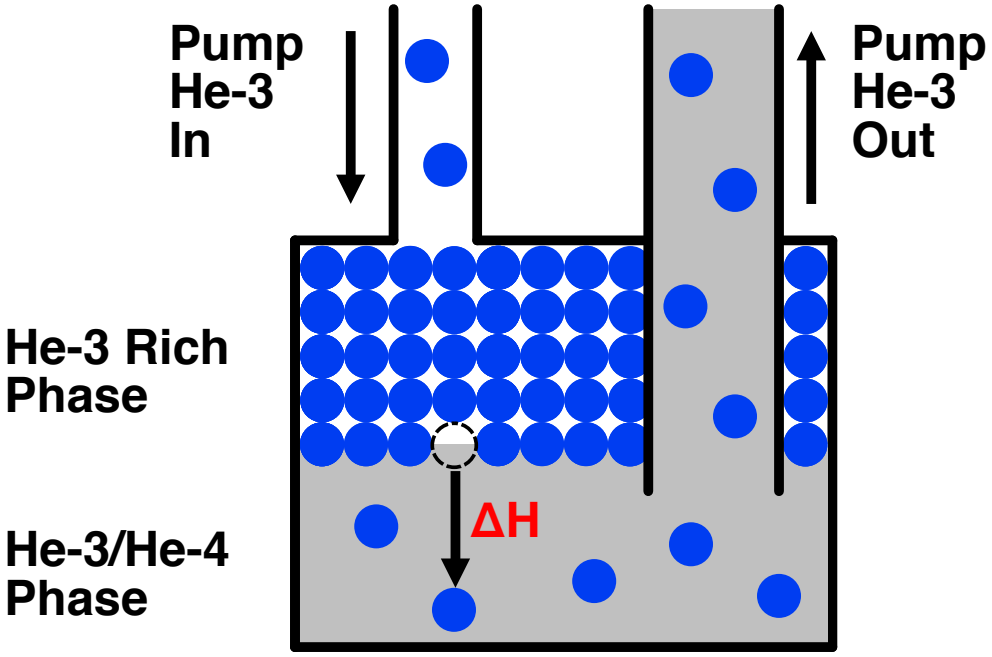

Figure 4.2: **Dilution Cooling in Mixing Chamber**. Schematic shows the flow of helium-3 in the mixing chamber of a dilution refrigerator, where the blue circles refer to He-3 atoms and the gray region refers to the inert superfluid He-4 background. He-3 is pumped into the chamber to the low-density He-3 rich phase. As each He-3 atom crosses into the He-3/He-4 phase, it takes up a heat ΔH from its surroundings, producing a cooling power. He-3 is then pumped out of the mixing chamber to be re-circulated and pumped back into the mixing chamber. Dilution cooling can achieve temperatures below $T_{mxc} = 10$ mK due to the finite (6.6%) concentration of He-3 in the He-3/He-4 phase.

Dilution Cooling in the Quantum Limit

In evaporative cooling, the heat of vaporization L is the relevant energy associated with a particle in the liquid phase crossing into the gas phase. By contrast, when

a single particle goes from from one *mixture* to another, the relevant energy is the enthalpy of mixing

$$\Delta H = \int_0^T \Delta C dT \tag{4.7}$$

where ΔC is the difference in heat capacities between the two mixtures. We can achieve cooling of the environment when $\Delta H > 0$, which will occur when $\Delta C > 0$. The intuition for this is that the heat capacity C characterizes the number of degrees-of-freedom of the particle in a given mixture, where each degree-of-freedom possesses a thermal energy set by temperature T. When the particle goes into another mixture with larger C, it gains additional degrees-of-freedom, each of which will take up thermal energy from the environment. Because of this property, maintaining a continuous flow of particles across the boundary, e.g. by pumping, produces a continuous cooling power.

To illustrate the procedure of dilution cooling, we will first discuss key properties of He-3 and He-4, then discuss why a finite amount of He-3 dissolves in superfluid He-4 even down at $T = 0$ K, and finish with an expression for the cooling power of this process.

Sub-Kelvin Properties of Helium-3 and Helium-4

The two isotopes of helium we will concern ourselves with are He-4 and He-3.

He-4 is a boson and becomes a superfluid at 2.177 K. Below 500mK, He-4 is almost entirely condensed into its quantum mechanical ground state, free of excitations such as rotons and phonons. In other words, it behaves primarily as a so-called inert superfluid background, which contributes to, say, the system volume but does not contribute to the heat capacity of the system.

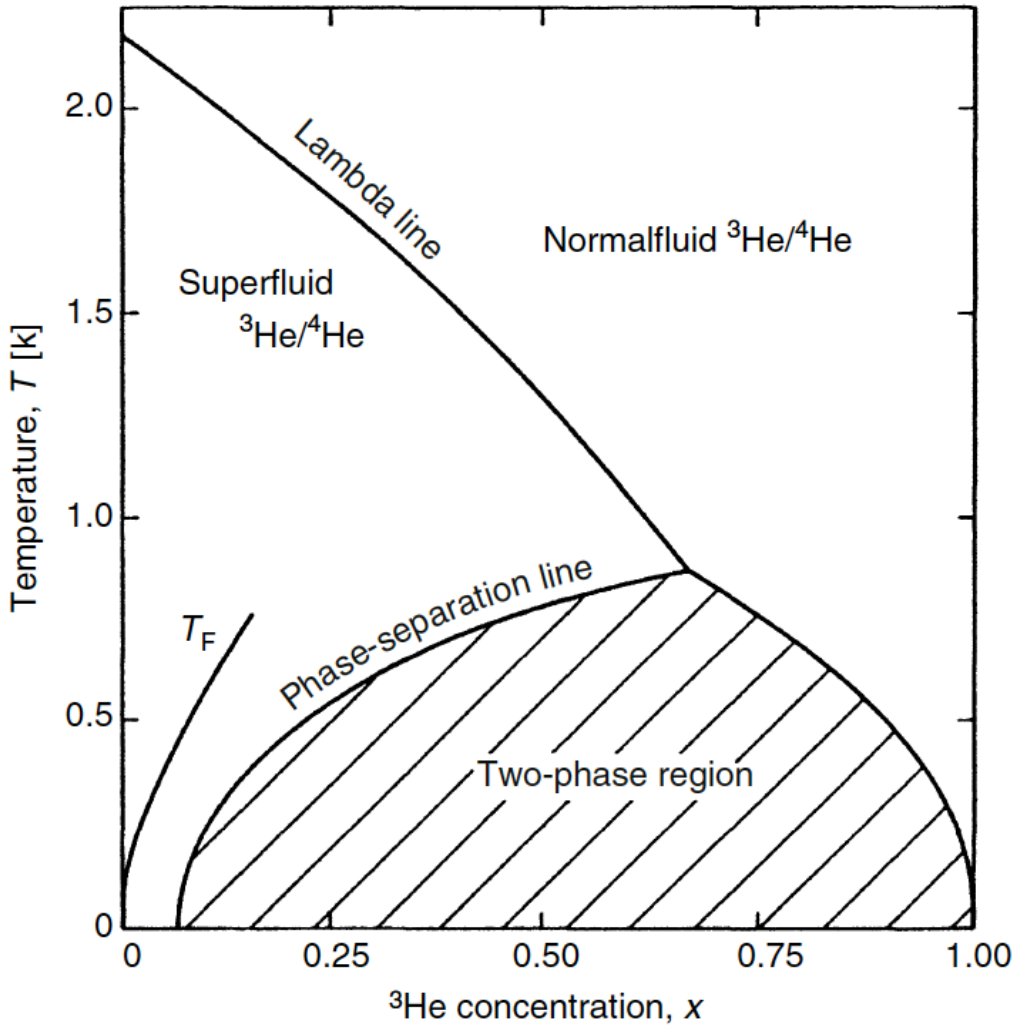

Figure 4.3: **Phase Diagram of Helium-3/Helium-4 Mixture, from [92]**. Phase diagram is shown as a function of temperature (y-axis) and He-3 mole fraction (x-axis). Below $T = 870$ mK, the hatched "two-phase region" is not physically accessible and the mixture has two distinct accessible phases along the phase-separation line, with different He-3 mole fractions x. One phase is He-3 rich ($x > 70\%$) and approaches $x = 100\%$ as $T \to 0$ K. The other ($x < 70\%$) is a dilute mixture of He-3 in superfluid He-4 and approaches $x = 6.6\%$ as $T \to 0$ K. This finite concentration of helium-3 is the source of the cooling power of a dilution refrigerator. Diagram taken from [92].

By contrast, He-3 is a fermion, and we will see shortly why this is relevant. First, though, we ask what happens if we add a concentration x of He-3 to the superfluid He-4 and lower the surrounding temperature T. As shown in Fig. 4.3, for $T < 870$ mK the mixture of He-3 and He-4 splits into two phases, one which is rich in He-3 and one which contains a dilute concentration of He-3 in superfluid He-4. As T approaches 0 K, the He-3 rich phase approaches a concentration of 100% He-3. However, the dilute concentration of He-3 in He-4 approaches a finite concentration of 6.6% *even* at $T = 0$K, which is the surprising result we will answer in the next section.

There are two key properties to note about He-3. First, since He-3 has a smaller per-atom mass than He-4 but roughly the same electronic properties, it will have a lower density than the He-4. For this reason, the He-3 rich phase will sit on top of the He-3/He-4 phase in the mixing chamber. Second, due to its fermionic properties, He-3 in superfluid He-4 can be modeled as a dilute non-interacting gas—similar to electrons in a metal—with the interactions between He-3 and the He-4 superfluid background taken into account via the substitution of the He-3 mass m with the effective mass $m^* \approx 2.5m$.

Finite Concentration of He-3 in He-4

To understand why there is a a finite concentration of He-3 in superfluid He-4 down to $T = 0$ K, we compare the energy of a single He-3 atom in the He-3 rich phase to the energy of a single He-3 atom in superfluid He-4. The former is simply given by the per-atom latent heat of vaporization L, where

$$\mu = -L \tag{4.8}$$

says that L is the binding energy that must be added to take a single He-3 atom from the He-3 rich phase to infinity.

On the other hand, if we place a single He-3 atom in superfluid He-4, it will be *more* strongly bound than in the He-3 rich phase. This is because the Van-der-Waals forces between He-3 and He-4 are identical due to their identical electronic structure, but the He-4 has a lower zero-point motion due to it's higher mass, i.e. it is more dense. Because of this, a single He-3 will be closer to the liquid He-4 atoms than to liquid He-3 atoms, so it will experience larger VdWs forces and a larger binding energy $-\epsilon$ in superfluid He-4 than in the He-3 rich phase. We write this as

$$-\epsilon < -L \tag{4.9}$$

Finally, if we add more He-3 atoms to superfluid He-4, they add as a non-interacting Fermi gas. In other words, due to Pauli repulsion, they will populate a Fermi sphere until the energy to add an additional He-3 atom to the He-3/He-4 phase is equal to the latent heat L of the He-3 rich phase

$$-\epsilon + k_B T_F(x = 6.6\%) = -L \tag{4.10}$$

where the Fermi temperature is $k_B T_F = \frac{\hbar}{2m^*}\left(\frac{3\pi^2 x N_0}{V}\right)^{2/3}$ for N_0 the total number of helium atoms, V the volume of the solution, m^* the effective mass of He-3 in He-4, and x the mole fraction of He-3. As denoted in the equation, this equality holds when the concentration of He-3 in He-4 is $x \approx 6.6\%$.

Projected Cooling Power of a Dilution Refrigerator

To calculate the cooling power of the mixing, we use the equation

$$Q = \dot{n}_3 \Delta H \tag{4.11}$$

which says that the cooling power Q is proportional to the rate $\dot{n}_3$ of He-3 going from the He-3 rich phase to the He-4 superfluid phase and each He-3 atom takes up an enthalpy ΔH as it crosses the phase boundary. Since the concentration of He-3 in superfluid He-4 is finite down to $T = 0$ K, it follows that $\dot{n}_3$ will also be finite.

Omitting a detailed calculation of the heat capacities of the two phases, we appeal to the fact that the heat capacity of the He-3 in both the He-3 rich and superfluid He-4 phase scales as

$$C \propto \frac{T}{T_F} \tag{4.12}$$

where, as discussed previously, the superfluid He-4 is in its quantum ground state below 500 mK and thus its heat capacity is dominated by that of the dilute gas of He-3. This implies that

$$\Delta H = \int_0^T \Delta C dT \propto T^2 \tag{4.13}$$

where as discussed previously $\Delta C > 0$, i.e. the heat capacity of He-3 in superfluid He-4 is larger than the heat capacity of the He-3 rich phase. Had we gone through the details of the calculation, we would have found, for $\dot{n}_3$ in units of moles per second crossing the phase boundary,

$$Q = 84 \dot{n}_3 T^2 \text{ [W]} \tag{4.14}$$

which approximately corresponds to $Q = 1\ \mu$W for $\dot{n}_3 = 100 \mu$mol/s at $T = 10$ mK.

4.2 BlueFors LD-400 Dilution Refrigerator

In late 2015, our group purchased and installed a BlueFors LD-400 dilution refrigerator. In this fridge, cooling takes place in a vacuum-sealed cryostat (see Fig 4.4 and 4.5e) with multiple radiation shields and thermally-conductive stages, the most important of which is the mixing chamber stage achieving measured temperatures as low as 6.8 mK and a measured cooling power of $P_{cool} = 18\mu$W at 20 mK ($n_{mol} = 1.08$ mmol/s) and $P_{cool} = 530\mu$W at 100 mK ($n_{mol} = 1.140$ mmol/s). We note that the dependence of cooling power agrees with a T^2 dependence to within 6%. A Cryomech pulse tube performs initial cooling of the system to ~4K, at which point the condensing and dilution procedure can begin. The dilution cycle is achieved using turbo and scroll pumps, high pressure lines, and compressors to force evaporated He-3 back into the dilution cycle (see Fig. 4.5a,b). Stage temperature is measured by resistive RuO_x thermometers. A separate control unit (see Fig. 4.5d) toggles valves and pumps, sets and monitors stage temperature, initiates cooldowns, and monitors fridge operation. A gas handling cabinet on wheels (see Fig. 4.5a) contains all pumps and pneumatic valves and can be placed in another room to reduce vibrations at the cryostat. An cooling water system (see Fig. 4.5c) allows a closed-circuit loop to cool the pumps while allowing heat transfer to occur to building water.

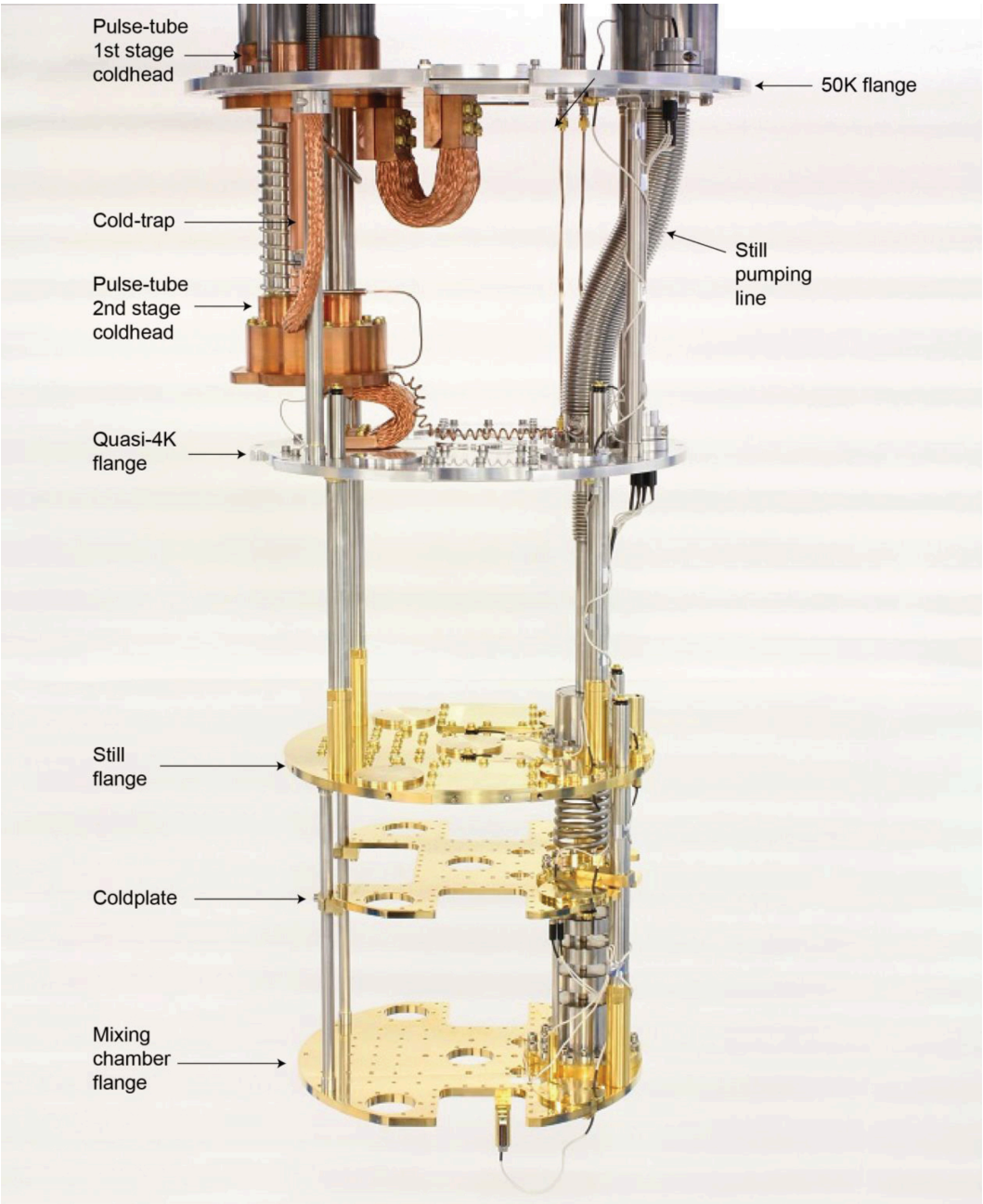

Figure 4.4: **LD400 Dilution Refrigerator Insert, borrowed with permission from BlueFors Oy.** Image showing the cryogenic plates of an LD400 dilution refrigerator. Descending plates achieve lower temperatures with the lowest mixing chamber plate achieving the minimum temperatures of the dilution refrigerator. At the top of the image is shown the coldhead of the pulse-tube used for pre-cooling the system without liquid He-4.

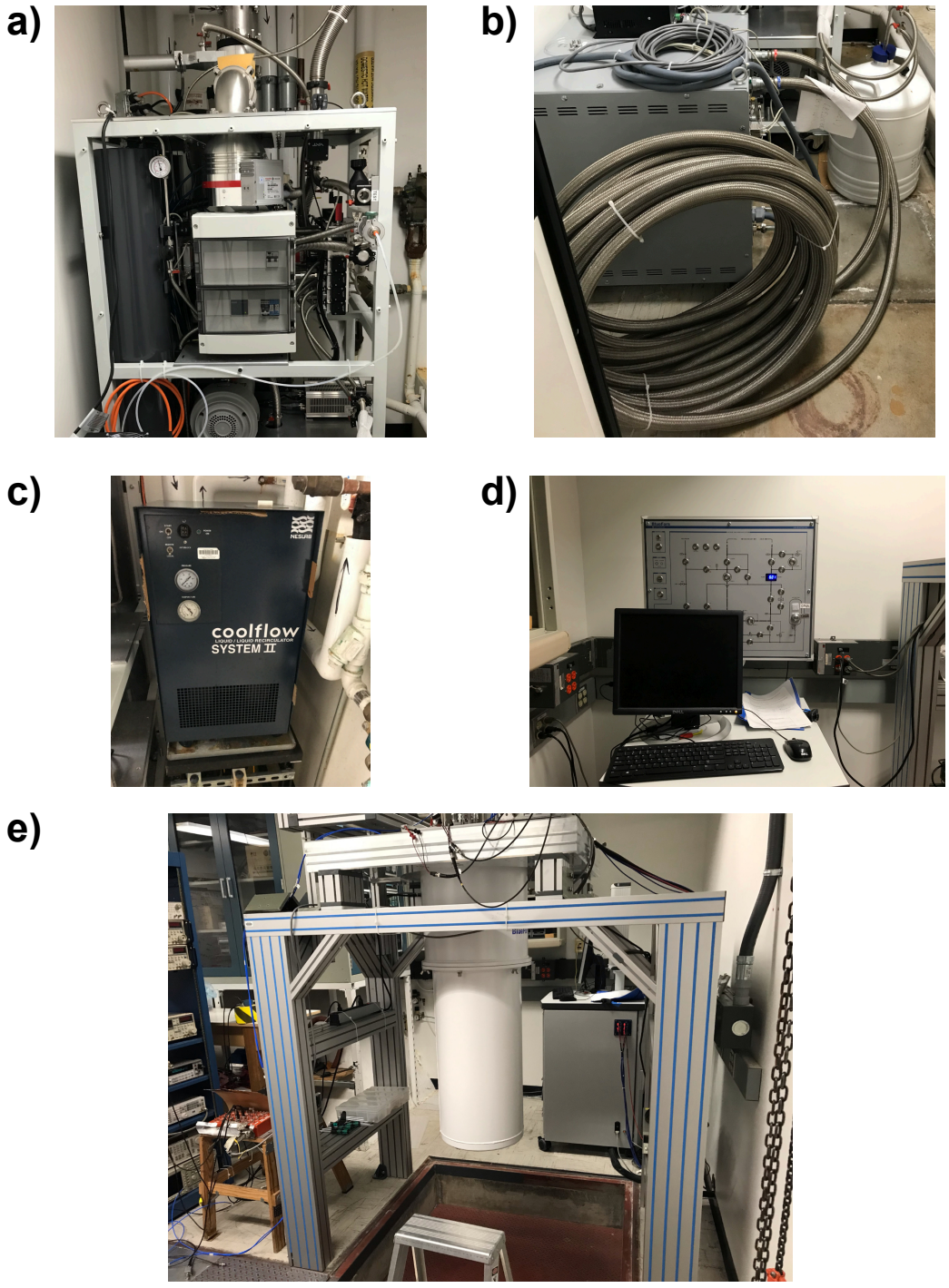

Figure 4.5: S_{21}. a. Gas Handling System. b. High-Pressure Lines and Compressor c. Water Chiller d. Control Unit e. Cryostat

4.3 S_{21} Measurement Circuit

Thermal characterization of the gJJ/resonator device require two sets of measurements. The first is microwave reflectometry to monitor the resonance feature produced by the gJJ-loaded microwave resonator. The second is the application and measurement of Joule heat power to the graphene flake in order to determine thermal properties of the flake which set fundamental limits on detector performance. We discuss both and refer to the full circuit diagram 4.3. Other useful resources for cryogenic RF measurement include [65].

Microwave Reflectometry

A standard S_{21} transmission measurement is performed in which a swept microwave tone is sent out of Port 1 of a PicoVNA 2 vector network analyzer (VNA) and down through attenuators and stages of the dilution refrigerator. The impedance of the resonator/gJJ device loads the line and scatters the incoming microwave tone. The transmitted portion of the microwave signal is amplified by a first-stage $T_n = 4\,\mathrm{K}$ CIT LF2 low noise amplifier, and then by three room temperature amplifiers, where it is detected by Port 2 of the VNA. The measured signal is

$$S_{21}(f) = \left.\frac{V_2(f)}{V_1(f)}\right|_{Z_0 \text{ on port 2}} = \left|\frac{V_2(f)}{V_1(f)}\right| e^{i\Delta\phi} \tag{4.15}$$

where V_1 is the complex voltage sent out of Port 1, V_2 is the complex voltage at Port 2 (which is terminated in a Z_0 impedance), and S_{21} is their complex ratio which contains the relative magnitude and the phase difference between the two waves.

To improve DC isolation between the device and the VNA, we include inner/outer DC blocks on the ports of the VNA. To vary readout power incident upon to the device, we vary the room temperature attenuation between $-50\,\mathrm{dB}$ and $-80\,\mathrm{dB}$. The attenuation at the fridge stages ensures the 300 K noise at room temperature is attenuated below the noise floor of the mixing chamber. In the diagram 4.3, the attenuators and amplifiers are positioned immediately under the fridge stage to which they are thermally anchored.

Heat Application and Measurement

Heater measurements are performed by applying a DC heater current I_{heater} to the heater port of the graphene flake and reading out the corresponding voltage drop in a 4-wire measurement. To source I_{heater}, an Agilent 33210A AWG outputs a DC volt-

age for the DC heating measurements and an AC voltage for noise equivalent power measurements. Since the ballast resistor $R_{ballast} = 1\text{M}\Omega$ is 3 orders-of-magnitude larger than the heater port resistance $R_{heater} \approx 1\,\text{k}\Omega$, the series combination of the AWG and $R_{ballast}$ can be well-approximated as a current source I_{heater}. The I_{heater} current travels down phosphor-bronze (PhBr) twisted-pair lines to the heater port where it Joule heats the graphene flake. Outside of the fridge, the shield on the twisted pair lines is held at fridge ground. The return line of the twisted pair is grounded through a $100\,\Omega$ resistor to a breakout box (not shown) which is also held at fridge ground. The return line terminates at the negative terminal of the AWG. We note that the possible ground loop introduced by the grounding of the twisted pair return line through the $100\,\Omega$ resistor does not have an appreciable effect on the measurement.

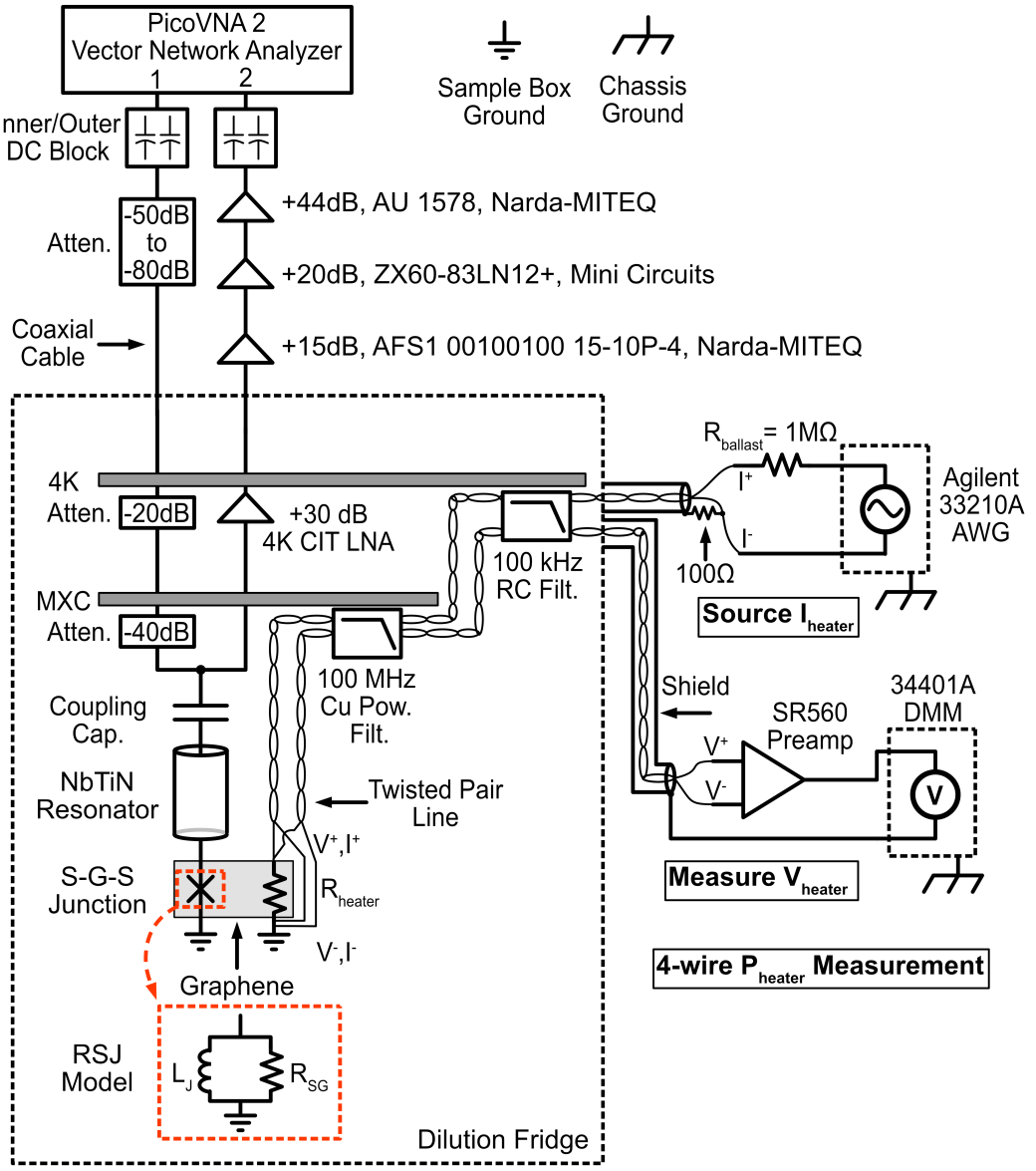

Figure 4.6: S_{21} **Circuit Diagram.** The circuit diagram shows both the S_{21} readout of the resonance feature and the application and readout of P_{heater}. In the S_{21} measurement, a signal is sourced from the PicoVNA2 vector network analyzer (VNA) and passes through a series of attenuators down to the resonator/graphene device held at T_{mxc}. The transmitted portion of the signal is amplified by an amplification chain with a first-stage 4K LNA and read out by the VNA. Application of P_{heater} proceeds by sourcing a current I generated by a voltage sourced by the Agilent 33221A AWG and dropped over a 1 MΩ ballast resistor. After passing through a two stages of filters, the sourced current flows through the normal resistance R_{heater} of the heater port of the graphene sample and dissipates Joule heat power in the flake. The voltage drop V across graphene heater is amplified by a SR560 preamp and read out by a 32201A digital multimeter (DMM). In this way, the $P_{heater} = I \times V$ delivered to the graphene flake is measured in a 4-wire measurement.

4.4 Amplifier Chain

Front-end amplifiers typically determine the accessible experimental parameter space of a low-noise cryogenic measurement. For the microwave reflectometry portion of our measurement, our front-end amplifier is a SiGe CIT LF2 low noise amplifier from Sandy Weinrab. For an applied bias voltage of 2.5 V, the gain is ≈ 30 dB, optimum frequency range is 10 MHz – 2 GHz, noise temperature is $T_n \approx 4$, gain compression is -14 dBm. While this represents a standard low noise amplifier in the present day, novel state-of-the-art amplifiers show improved specifications, such as the traveling-wave parametric amplifiers of Josephson-type (JJ-TWPA) [76] and of kinetic inductance-type (KI-TWPA) [38]. These amplifiers, especially the latter, suggest a means of achieving quantum-limited ($T_n \approx 50$ mK/GHz), large-gain amplification over large bandwidths. While much work has been focused on amplifiers in the frequency ranges of 1-4 GHz, 4-8 GHz and 8-12 GHz for quantum information applications, recent work has shown KI-TWPAs operating up to 30 GHz [106]. With a fundamental limit on frequency operation set by the $\sim$1.4 THz superconducting gap frequency of NbTiN, the coming years are expected to see amplifier designs at even higher frequencies for applications in astronomy and high-frequency quantum information.

As shown in Fig. 4.7, we additionally have three room-temperature amplifiers following the first stage amplifier for amplifying the S_{21} resonance signal. In order, the amplifiers are a +15 dB Narda-MITEQ AFS1 00100100 15-10P-4, a +20 dB Mini-Circuits ZX60-83LN12+, and a +44 dB Narda-MITEQ AU-1578. For a -100dB tone sent through these three amplifiers, we see the output signal (Fig 4.8) is amplified by +80 dB in the frequency range of 500 MHz – 1 GHz. This is in agreement with the specifications for each of these three amplifiers.

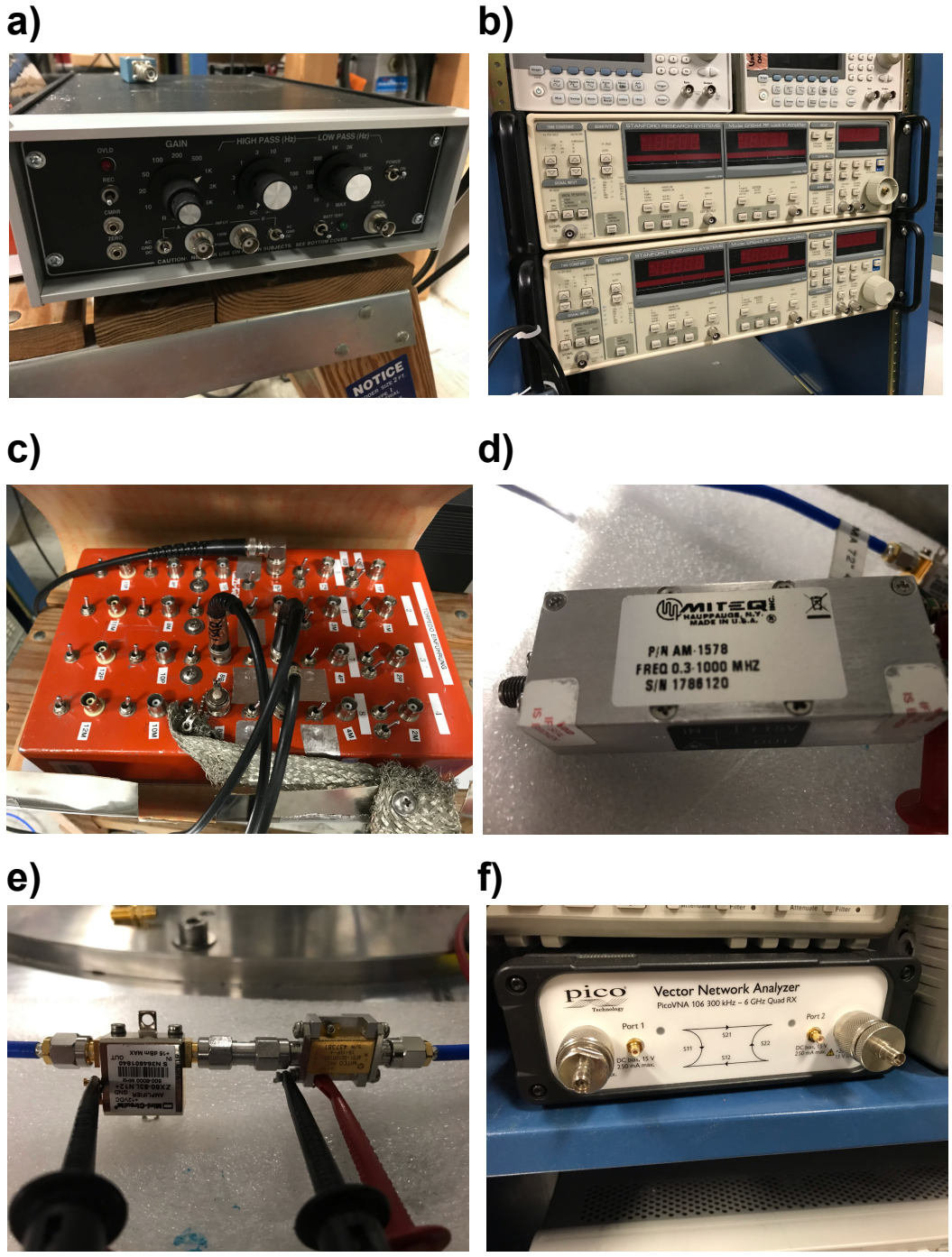

Figure 4.7: S_{21}. **a.** DL 1201 Low Noise Voltage Preamp, used for amplifying output of heater port. **b.** Model SR844 RF Lock-In Amplifier. **c.** Breakout box used for sending signals on twisted-pair lines. **d.** +44 dB Narda-MITEQ AU-1578 Room Temperature Amplifier **e.** +15 dB Narda-MITEQ AFS1 and +20 dB Mini-Circuits ZX60-83LN12+ Room Temperature Amplifiers. **f.** PicoVNA 106, 300 kHz– 6 GHz Vector Network Analyzer.

,

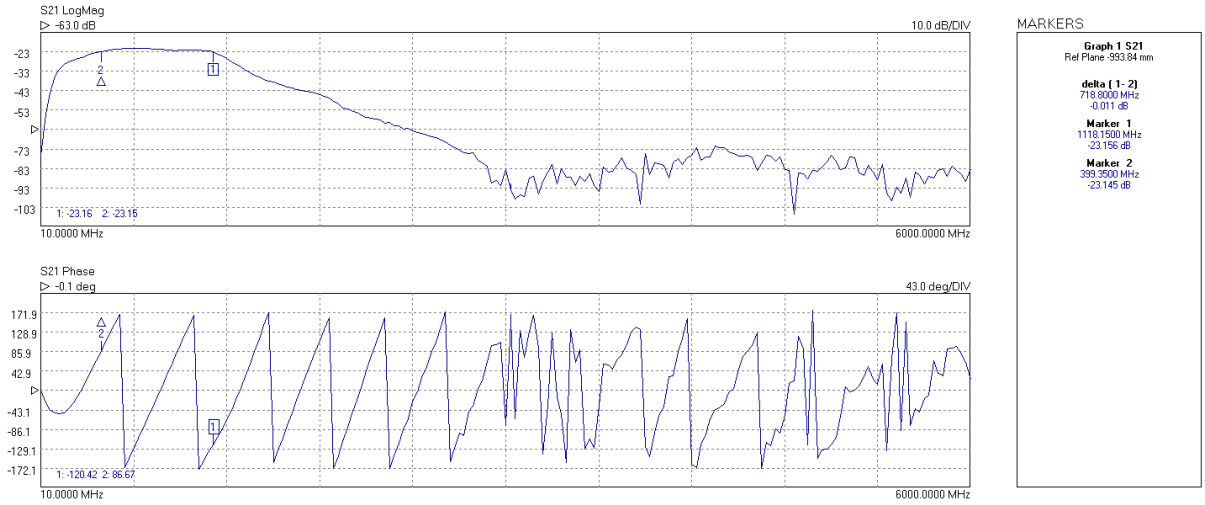

Figure 4.8: S_{21} **Room Temperature Amplifier Cascaded Gain Profile.** For an input -100 dBm signal, the gain (S_{21} mag) of the thee room temperature amplifiers is approximately 80 dB over 500 MHz- 1 GHz.

4.5 Sample Box

The sample box (designed by Olli Saira) fulfills three purposes. First, it holds the samples and maintains a low-resistance thermal link with the mixing chamber stage. Second, it includes magnetic shielding to reduce parasitic couplings between the sample and environment. Third, it routes and filters DC and RF electrical signals to the samples.

To achieve the the first of these functions, the sample box has 24 DC lines (connected via PhBr twisted pair lines to room temperature electronics) and 6 RF lines (connected via RF BeCu coaxial cables to room temperature electronics). The sample is adhered to the sample box using epoxy or other thermally conductive adhesive and

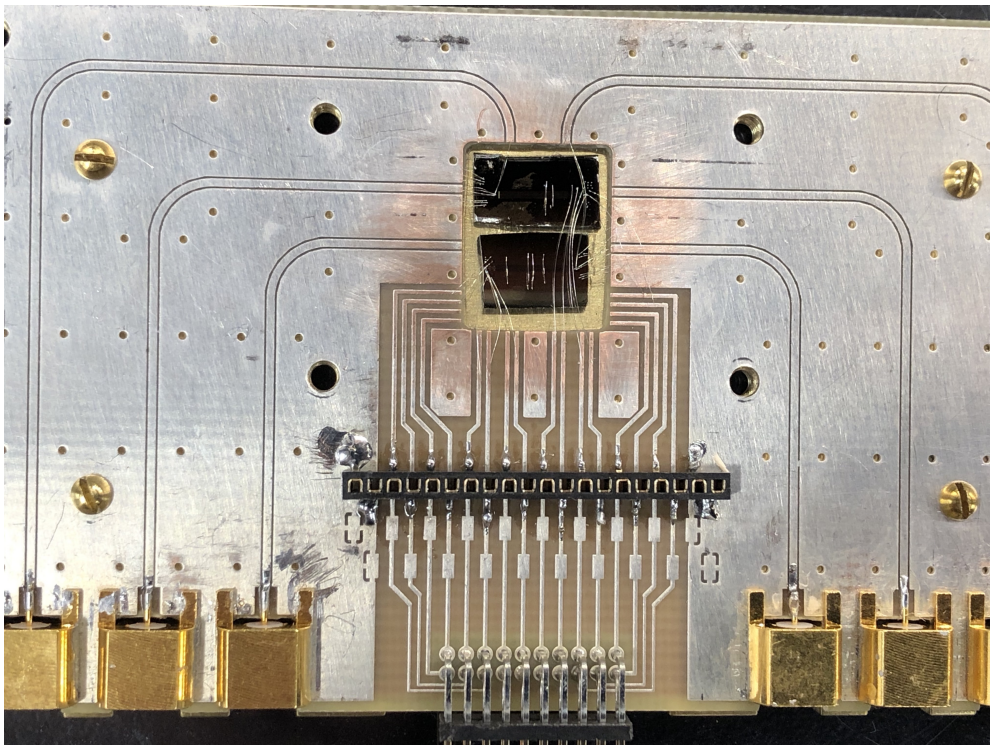

Figure 4.9: **Sample Holder.** Here we have a view of the inside of the sample holder, with two chips adhered to the holder with wirebonds to the lines responsible for carrying DC or RF signals to the sample. At the bottom, 16 quasi-DC filtered twisted pair lines are available to wirebond to the samples. From the sides and top, 6 RF lines are available for wirebonding, here shown as coplanar waveguides with the central conductor clearly separated from the aluminum ground plane and 6 connectors visible.

wirebonded to any of the lines. As shown in Fig 4.10a, the sample box is made of low-thermal resistance metal and attached to the mixing chamber stage via a copper L-joint and screws (see Fig 4.10e-f).

Second, a magnetic shield is placed over sample box, as denoted by the grey region in Fig 4.10a. Since mu-metal shielding characteristics can degrade at cryogenic temperatures, the shield is made of CRYOPHY, a high-permeability nickel-iron soft magnetic alloy (Ni/Mo/Fe) operational down to cryogenic temperatures. The shield is 1.5mm thick and 4.4" in its longest dimension. COMSOL simulations predict shielding of external magnetic fields up to a factor of 10^5 approximately 1" into the body of the shield. As shown in 4.10f, a piece of heavy copper foil is used to thermally link the magnetic shield to the sample box.

For electrical filtering, the sample box includes a copper powder filter on the DC

lines. Fig 4.10b shows the DC lines prior to their submersion in the stycast/Cu powder mixture, with more in-depth discussion of such filters in section 4.6. The 6 RF lines in the sample box are designed as air-gap CPW lines filled with Eccosorb, a microwave absorber used to attenuate high-frequency signals. The top and bottom portions of the RF lines are shown in 4.10c-d, where the black sections are the Eccosorb. COMSOL simulations suggest Eccosorb attenuation scales roughly as $1\frac{\text{dB}}{\text{GHz cm}}$. We use a 0.5"-long piece of Eccosorber which is predicted to yield no appreciable change in the 50 Ω characteristic impedance for < 5 GHz frequencies.

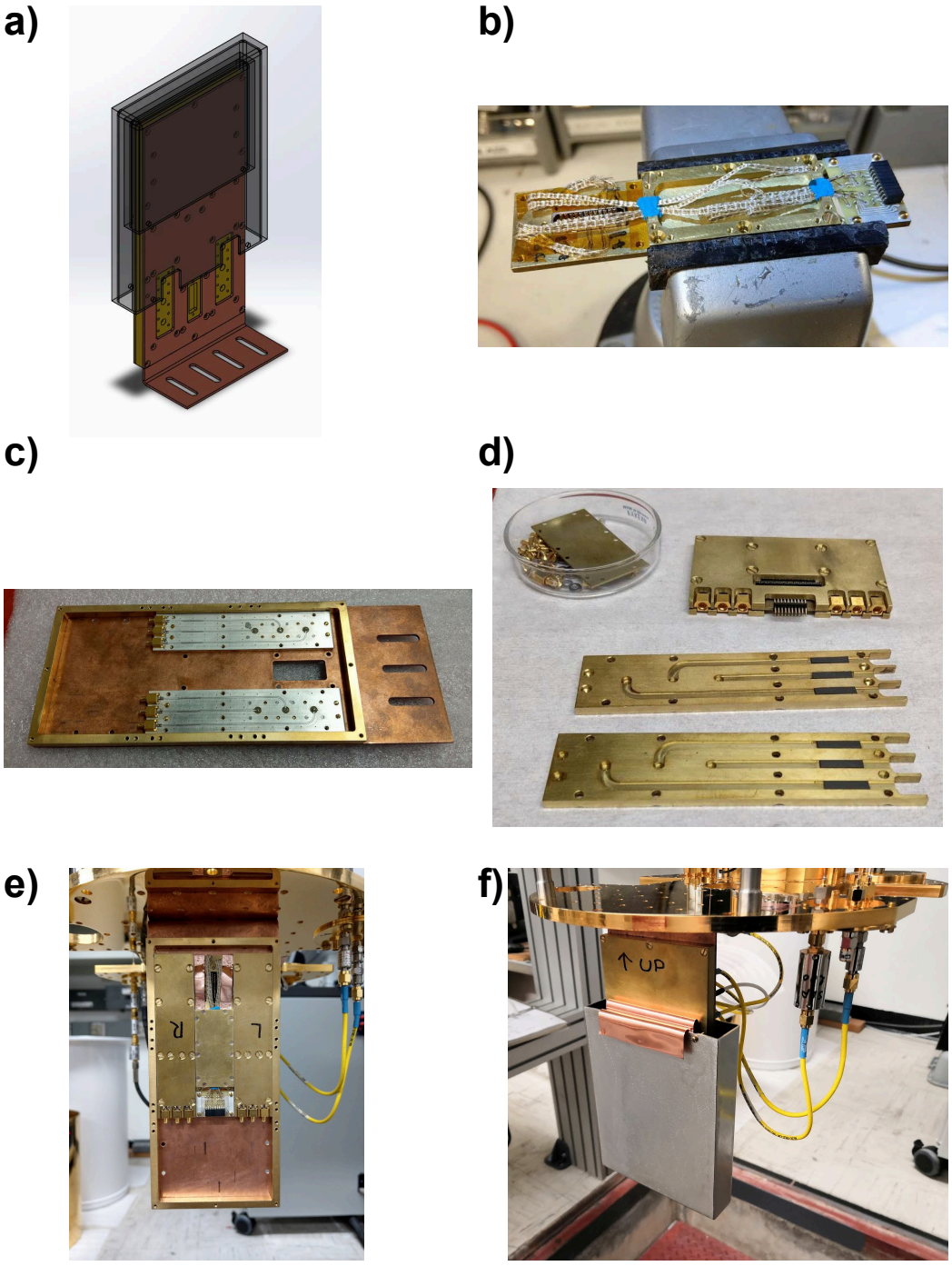

Figure 4.10: **Sample Box Photos (courtesy of Olli Saira). a.** CAD diagram of sample box. **b.** DC twisted pair lines prior to immersion in copper powder/Stycast mixture. **c.** Sample box coplanar waveguide grooves. **d.** Coplanar waveguide grooves in opposite plate, with Eccosorb regions. **e.** Sample box installed on mixing chamber stage. **f.** Installed sample box with magnetic shield and thermalizing copper sheet

4.6 Metal Powder Filters

Since Josephson junctions act as wideband detectors of microwave and RF signals, filtering high frequency noise is important for proper operation of these devices. For example, ambient high-frequency RF noise can be filtered with mu-metal shielding, and high frequency noise on electrical lines can be filtered with electrical filters.

Focusing on the latter of these two filter types, low-pass lumped-element RC, RLC, and LC filters in the microwave and RF regime typically have precisely engineered filter characteristics, such as cut-off frequency, roll-off steepness, attenuation, and ripple. However, these filters often suffer from diminished attenuation at higher frequencies due to parasitics. For example, Bladh et. al. [14] showed that a single pole RC, two-stage RLC, and Minicircuits LC filters all demonstrated attenuation no better than 20-30 dB for frequencies above 4 GHz. This is of particular concern when >120dB attenuation is required to attenuate high frequency signals below the noise floor.

To alleviate this issue, Martinis et. al. [77] introduced a new type of filter to improve attenuation at high frequencies. Initially, they used an RC filter bank at 4.2 K with cutoff frequency of 1 MHz which showed a large 60 dB attenuation from 20-200 MHz. However, at higher frequencies the attenuation decreased, likely due to stray capacitance across the resistors. Subsequently, a filter composed of a spiral coil of insulated Manganin wire surrounded by copper powder was included, which achieved an attenuation of 50 dB from 0.5-12 GHz. By incorporating a chain of filters, including a 3-pole RF LC filter, two series powder filters installed at 4.2K, and two filters at the stage temperature, they demonstrated a 200 dB attenuation from 100 MHz to 12 GHz.

Metallic powder filters have since become standard in cryogenic electronics. They can simultaneously filter high-frequency noise and spurious signals while thermalizing the line to the low temperature stages. Further, they are relatively easy to make and present a low resistance which reduces extraneous heating. However, they are often relatively bulky, with high cutoff frequencies and low temperature behavior which is difficult to predict at the construction stage. Mixing the powder with epoxy can improve thermalization of the wire, but it can also diminish the attenuation and produce parasitic resonances when the packing inside of the wire coil is incomplete or when air bubbles produce a non-homogenous grain distribution.

Construction of the filter is reasonably straightforward. A thin insulated wire is surrounded by a fine grain metal powder. Grains are typically of size 30μm - 60μm

and coated by a native insulating dielectric which produce a large effective surface area. The physical mechanism underlying the filter is the phenomenon of skin-effect damping, in which high frequency magnetic fields on the line are dissipated as eddy currents induced in the grains of the metallic powder. To reduce magnetic pickup, half the wire is wound in a spiral while the other half is counter-wound. To ensure good thermalization, the metallic powder can be mixed with Stycast epoxy and used to coat the inside and outside of the coil. Attenuation depends on grain size and composition (copper, bronze, stainless steel) as well as the geometry of the wire [77, 74].

When designing a filter chain to attenuate the entire bandwidth of interest, it is important to remember that metallic powder filters typically have large cut-off frequencies (attenuation to the noise floor at 1-2 GHz). By contrast, lumped-element filters can be engineered to have much lower cut-off frequencies, although they suffer from diminished attenuation at higher frequencies. Therefore, it is standard to place these two types of filters in series to attain good attenuation throughout the bandwidth of the measurement. Lukashenko et. al. [74] take this idea to the limit of integrating an LC filter directly into the powder filter. They exploit the inductance of the powder filter wire and integrate two discoidal capacitors to construct what they term a powder-Pi filter. Their design achieves filter characteristics including a low cut-off frequency at 1 MHz, low ripple, steep decay of -50dB/decade per filter stage, attenuation at high frequencies, and low-temperature behavior which well-approximates the intended design of the filter.

In our setup (see Fig. 4.3), we include two low-pass filters on the heater twisted pair lines used for applying DC and low-frequency AC heat to our graphene device [98]. There is an RC filter bank at 4K (R = 600 Ω, $f_0 = \frac{1}{2\pi RC} = 100$ kHz) followed by a copper powder filter at stage temperature. The copper powder filter is composed of a 20 cm resistive constantan twisted pair (R=14 Ω/wire) in a Stycast/Cu powder dielectric mixture. Room temperature characterization of a similar filter box suggests a cutoff frequency of $f_0 = 100$ MHz.

4.7 Conclusion

In this chapter, we have done the following:

- We have discussed the operation of a dilution refrigerator from first principles, showing how the properties of quantum fluids makes possible cooling down to < 10 mK temperatures.

- We have discussed attributes of our BlueFors LD400 dilution refrigerator used for cooling samples to sub-Kelvin temperatures.
- We have discussed microwave reflectometry and heating measurement setups, including a detailed diagram of these measurements.
- We have discussed important RF components of our measurements, including the amplifier chain, sample boxes, and filtering.

Chapter 5

NANOFABRICATION

In this chapter, we will discuss the nanofabrication procedure used to make the graphene/resonator device. Often the least celebrated stage of an cryogenic experiment, nanofabrication is nevertheless often the most important (and least predicable from first principles) since it determines the set of accessible devices that can be constructed and measured. To illustrate the nanofabrication procedure, we perform the following:

- First, we will discuss the nanofabrication recipe used to define and etch the NbTiN resonator, form the graphene-based material stack, and evaporate the aluminum electrodes used to join the material stack to the resonator. The recipe will be discussed in sufficient detail to be replicated in a standard university cleanroom.
- Second, we will discuss the device design, including a brief review of transmission lines and transmission line resonators, and provide key transmission line parameter estimates from RF electromagnetic simulations.

Completion of this chapter will provide the reader a sufficient understanding of the device architecture to prepare them for the following chapters, in which the graphene/resonator device will be fully characterized using microwave reflectometry, thermal response measurements, and noise measurements.

5.1 Fabrication Procedure

This nanofabrication procedure follows standard graphene and transmission line resonator fabrication procedures. Additional details may be found in Harpreet Singh Arora's PhD thesis [4].

Patterning the NbTiN Resonator

The initial substrate is a commercially available undoped silicon wafer with 300 nanometers of thermally-grown silicon dioxide. After a few hundred nanometers of NbTiN ($T_c \approx 14$K) are sputtered using a commercially available sputtering target, the wafer is diced into small ~5x7mm pieces using a handheld diamond scriber.

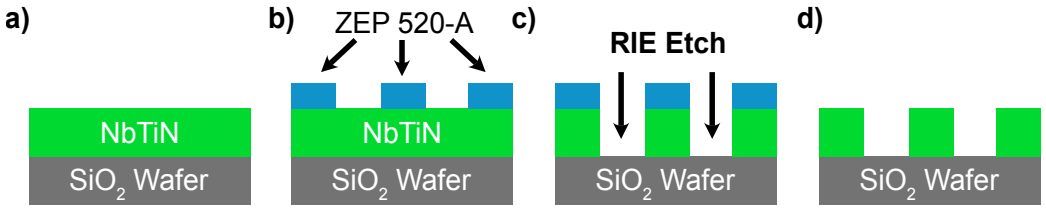

Figure 5.1: **Patterning the NbTiN Resonator. a)** A cross-section schematic of the NbTiN film sputtered on a SiO_2 chip is shown. **b)** To form the etch mask for patterning the NbTiN resonator, an electron beam resist is spin, baked, patterned in an EBPG and developed. **c)** A reactive ion etch etches away that portion of the NbTiN which is not covered by the electron beam resist mask. **d)** The resist is removed according to standard procedures, leaving behind the patterned NbTiN resonator, shown in cross section.

To pattern the resonator (as shown in Fig. 5.1), an etch mask is defined using a conventional electron beam resist, typically ZEP 520-A (Zion Chemicals). The resist is spun onto a diced chip at 5000 rpm for 90 seconds and baked on a hotplate at 150°C. The chip is then transferred to the electron beam pattern generator (EBPG) where the resonator pattern is inscribed into the resist using a 1 nA beam current and 350 $\mu C/cm^2$ dose. Following the EBPG write, the chip is dipped in a developer solution, typically ZED N50, for 90 seconds and isopropyl alcohol for 30 seconds before being blow-dried with nitrogen gas. To smooth the resist edges, and consequently the resonator profile, the chip is placed on the 150°C hotplate for an additional 3 minutes.

To etch the NbTiN resonator, we place the chip in the reactive ion etcher (RIE). To remove any residual resist, we first perform a mild O_2 reactive ion etch for 45s (50 sccm O_2 flow, 60 mTorr chamber pressure, 40 W RF power). Then, we perform an SF_6/Ar reactive ion etch with an etch rate of approximately 100nm NbTiN per 120 seconds (20 sccm SF6 flow, 10 sccm Argon flow, 15 mTorr chamber pressure, 80 W RF power).

For a final clean, the chip is placed in N-Methyl-2-Pyrrolidinone (NMP) at 80°C for an hour. A final mild O_2 reactive ion etch (same recipe as above) is performed to remove any residual resist. The chip is now ready for the graphene stack transfer.

'Stamping' the Van-Der-Waals Material Stack

The stack of Van-der-Waals materials (of which graphene is the active layer) is assembled via a 'stamping' procedure, in which the top layer is first picked up and

is then used to pick up all subsequent layers [5, 119]. Remarkably, no adhesive is required beyond that used to pick up the top layer, since the thin layers of different Van-der-Waals materials attract one another via Van-der-Waals forces. This procedure is shown in Fig. 5.2.

Initially, a glass slide is prepared with two layers of polymer. The base layer, a silicone elastomer Polydimethylsiloxane (PDMS), is chosen for its mechanical properties and chemical inertness. The second layer, a solution containing polycarbonate (PC) plastic with bisphenol-A (BPA), is chosen for its good adhesive properties. The glass slide is heated to 100°C, lowered to contact the top hBn layer with the adhesive PC, and subsequently raised to pick up the hBn layer. This is repeated to pick up the descending layers of the material stack and achieve the desired stack profile. Once all layers have been picked up, the entire stack is placed on the chip with the etched NbTiN resonator at 100°C. Then, the glass slide is raised to a temperature of 180°C to melt the PC and is lifted away, leaving behind the Van-der-Waals material stack covered by a layer of PC. The outcome of this nanofabrication step is that the Van-der-Waals material stack has been 'dropped' on the resonator chip and is ready to be contacted with metallic electrodes.

Deposition of Aluminum Electrodes

To define a deposition mask for the aluminum electrodes (as shown in Fig. 5.3), a 400-500nm layer of PMMA 950-A5 is spun onto the chip at 2000 rpm at 180°C for 90 seconds. Once again using electron beam lithography, the electrode pattern is inscribed into the resist with a large 1200 $\mu C/cm^2$ dose to ensure removal of the PMMA. After a standard PMMA development (MIBK:IPA 1:3 for 90 seconds), the chip undergoes a mild O_2 etch in the RIE (recipe above) to remove residual resist. Then, a CHF_3/O_2 etch in the RIE is performed to expose the 1D edge of the graphene [118] and allow for an Ohmic contact to the aluminum (40/4 sccm CHF_3/O_2 flow, 40 mTorr pressure, 60 W RF power). To deposit the aluminum electrodes, the chip is transferred to a Lesker electron beam evaporator free of any magnetic materials. There a Ti/Al (5nm/100nm) film is evaporated, where the thin Ti layer is included for improved adhesion of the aluminum to the Van-der-Waals stack. Following a standard liftoff (typically in acetone), the result of this procedure is to contact aluminum electrodes to the Van-der-Waals material stack and NbTiN resonator. Fabrication is complete and the sample is now ready for measurement.

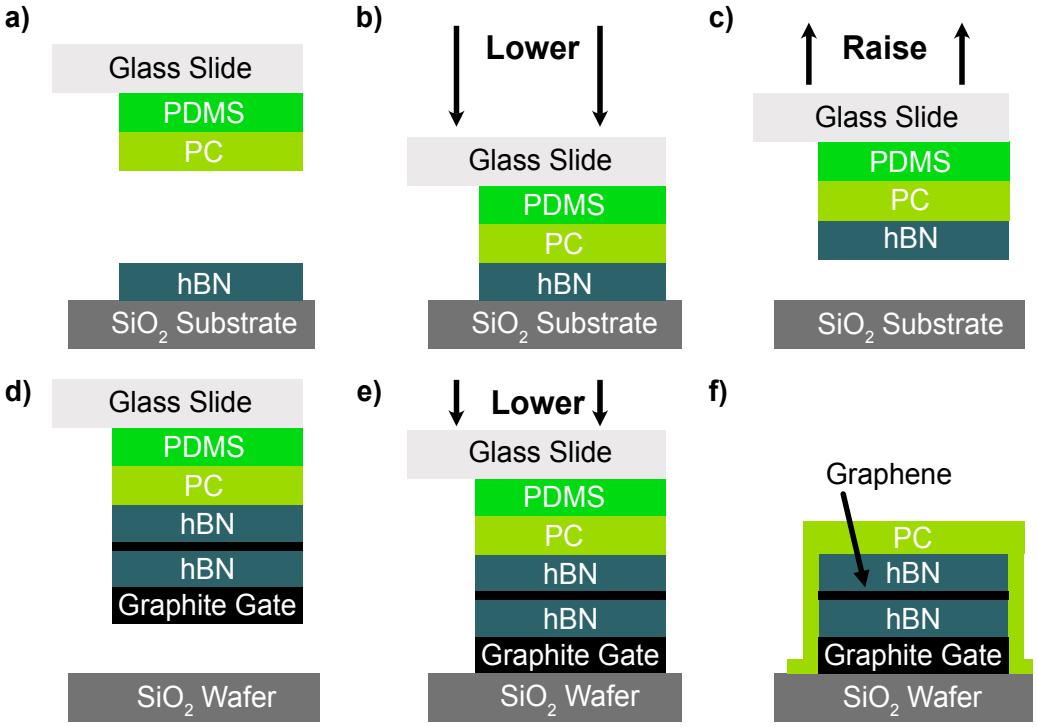

Figure 5.2: **Stamping Procedure.** **a)** The stamping procedure is performed using a glass slide covered by a silicone elastomer (PDMS) and adhesive polycarbonate (PC), **b)** The glass slide and polymers are lowered until the PC layer contacts the hexagonal boron nitride (hBn) layer. **c)** With the PC layer adhered to the hBn layer, the glass slide is raised, lifting the hBn layer off of the substrate. **d)** This procedure is repeated on all layers of the Van-der-Waals material stack, where Van-der-Waals forces create a sufficient attraction between the layers to allow stacking without any additional adhesive beyond the PC layer. The final material stack is shown and the SiO_2 wafer, in contrast to the SiO_2 substrate denoted previously, refers to the SiO_2 NbTiN chip upon which the Van-der-Waals stack will be stamped. **e)** The full stack is lowered onto the SiO_2 NbTiN chip for final placement. **f)** The glass slide is heated to melt the PC layer and lifted away, leaving behind the material stack covered in a layer of molten PC. The material stack is now ready to be contacted with metallic electrodes.

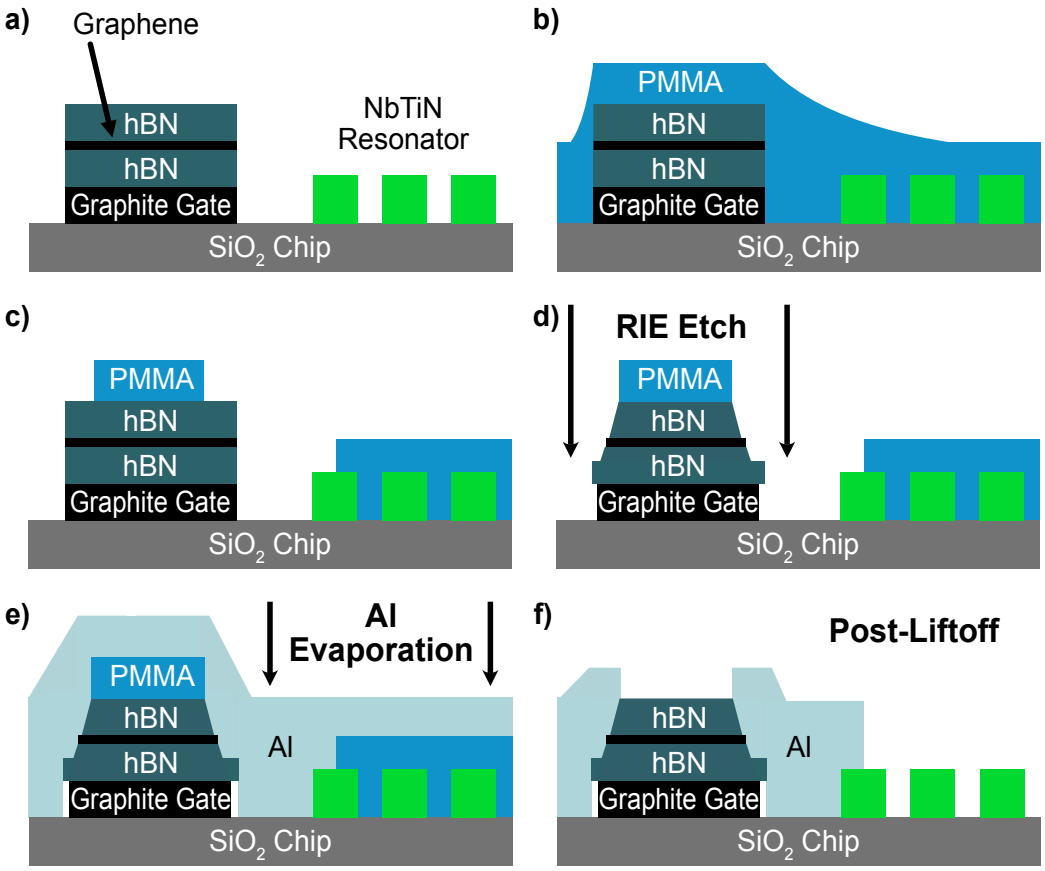

Figure 5.3: **Deposition of Aluminum Electrodes. a**. From the prior stamping step, the Van-der-Waals material stack is stamped on the NbTiN resonator chip. **b**. A PMMA mask is spun and baked on the chip. The mask will be used both as an etch mask and for a liftoff procedure to define the metallic contacts. **c**. Using electron beam lithography, the electrode pattern is inscribed into the PMMA and developed in a standard PMMA developer, removing the PMMA mask in those regions of the chip where aluminum contacts will be placed. **d**. An RIE CHF_3/O_2 etch is performed to etch into the Van-der-Waals stack and reveal the 1D edge of the graphene flake, in order to make a low-resistance Ohmic contact. **e**. Aluminum is evaporated onto the chip using an electron beam evaporator free of magnetic materials which may inhibit superconductivity. A thin titanium layer can be included to promote adhesion between the evaporated aluminum and substrate. **f**. The PMMA mask is removed in a standard liftoff procedure, leaving behind the aluminum electrodes patterned by the etch mask. The nanofabrication procedure is now complete and the sample is ready for measurement.

Example of an In-Process Sample

Shown is an example of an in-process (failed) hBn-encapsulated graphene sample. The goal of this sample was to define a Hall bar geometry in order to characterize the carrier density and mobility of the two-dimensional electron gas housed in the graphene flake.

Visible is a developed PMMA etch mask with an inscribed electrode pattern. The etch mask has also undergone an RIE plasma etch to etch into the Van-der-Waals material and prepare the sample for deposition of metallic electrodes. This corresponds to the completion of step d) in Fig. 5.3.

The central, brightly colored region at the center of the image shows the location of the stamped Van-der-Waals material stack. The aqua-colored region is the bottom hBn, the yellow region within the aqua region is the top hBn, and the darkened region overlapping both region is the graphite backgate, which sits underneath all other Van-der-Waals layers.

In the center of the material stack, the patterned Hall bar geometry is clearly visible. The topmost electrode is designed to contact the backgate, as indicated by its overlap of the darkened region of the sample. For the bottom set of electrodes, the uninterrupted brown regions show that reactive ion etch has etched through the bottom hBn and likely into the graphite backgate. Were metal to be evaporated on this sample, the bottom electrodes would likely be shorted to the gate, eliminating the possibility of performing reliable Hall measurements.

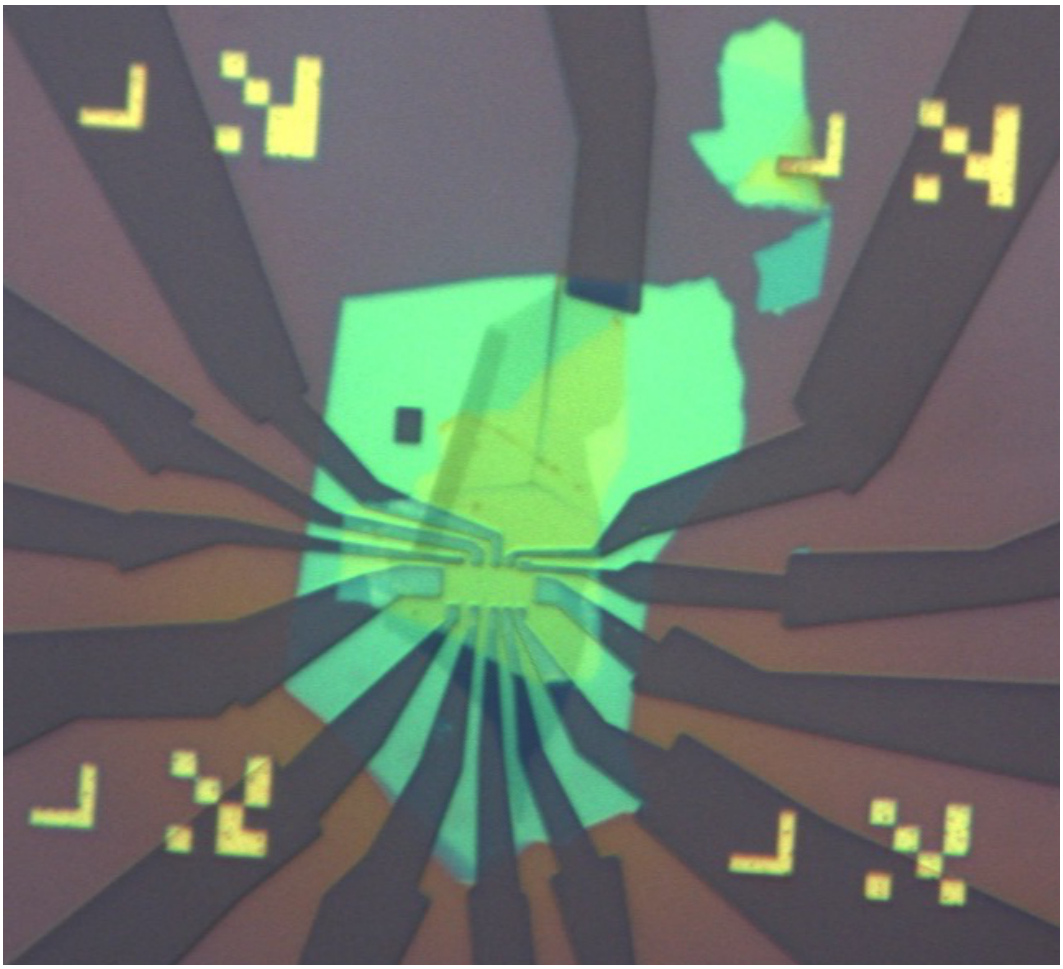

Figure 5.4: **Optical Image of Patterned Electrodes in a PMMA Mask on a Graphene-based Material Stack.** Visible is a developed PMMA etch mask with an inscribed electrode pattern. The aqua-colored region is the bottom hBn, the yellow region within the aqua region is the top hBn, and the darkened region overlapping both colored regions is the graphite backgate. Brown finger-like projections correspond to electrode designs patterned into the PMMA etch mask.

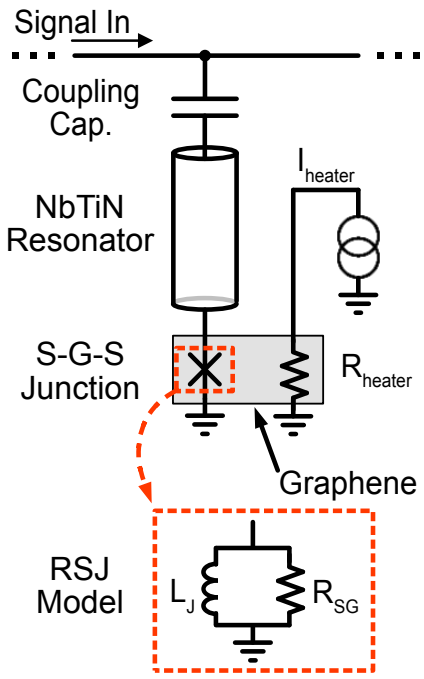

Figure 5.5: Electrical circuit schematic. A resonator designed for low characteristic impedance made of Niobium Titanium Nitride (NbTiN) is coupled to the external microwave line via coupling capacitor and terminated by the S-G-S junction. Characterization of the device is performed by sending in a microwave tone and measuring transmission coefficient S_{21}. Changes in the junction's electrical impedance shift the resonant frequency of the NbTiN resonator. A dedicated heater port allows application of Joule heat to the graphene flake, thereby electrically isolating the heating and readout ports while maintaining a thermal link between them. The resistance between heater port and the ground is ~1 kΩ. We model the S-G-S junction electrically as the parallel sum of a dissipationless branch of inductance $L_J = \frac{\Phi_0}{2\pi I_c}$ and a dissipative branch of resistance R_{SG}.

5.2 Graphene/Resonator Device

We now discuss the design and architecture of the Van-der-Waals material stack and NbTiN resonator define by the nanofabrication recipe as previously stated. In the next chapter, we will discuss the electrical properties of this device further, but for now we show the electrical circuit realized by the electrically-connected resonator and Van-der-Waals material stack (see Fig. 6.4), in order to give the reader an intuition for the relative placement and function of each of the components.

Encapsulated Graphene Device

Fig. 5.6 shows a top-down, real-color optical image of the encapsulated monolayer graphene device, to which material stack in Fig. 5.3 refers. The Van-der-Waals material stack is the blue-green region (the hBn primarily sets the color) and is contacted by aluminum electrodes (light blue). The encapsulated graphene flake has approximate area $A \approx 25\mu m^2$.

The electrodes serve four purposes. First, they form the superconducting leads of a superconductor-graphene-superconductor (S-G-S) junction, in which supercurrent flows from one superconducting aluminum electrode, through the monolayer graphene, to another superconducting aluminum electrode. In our device, supercurrent flows from the finger at the top of the image to either of the two symmetrically-placed ground wires which span the length of the device. The small superconducting gap (T_c ~1.1K) of the aluminum is expected to increase the temperature sensitivity of the graphene detector at sub-Kelvin temperatures. This is born out in the large temperature sensitivity of the device for device temperatures 180 mK–500 mK. Second, the electrodes form electrical contacts which are either connected to ground or form a series electrical connection to the NbTiN resonator. Third, the electrodes define the heater port and lead, which is used to source a normal current I_{heater} to the graphene flake and apply Joule heat for thermal characterization measurements. This port is placed far enough from all other superconducting electrodes to suppress supercurrent flow. Finally, one electrode (not shown) is used to apply a DC voltage to the graphite backgate in order to control the carrier density of the graphene flake.

The purpose of encapsulating monolayer graphene in hexagonal boron nitride is to reduce disorder and increase the mean free path of carriers [122]. We see from the Fabry-Perot-type oscillations measured in 6.3 that the carriers in the are indeed ballistic.

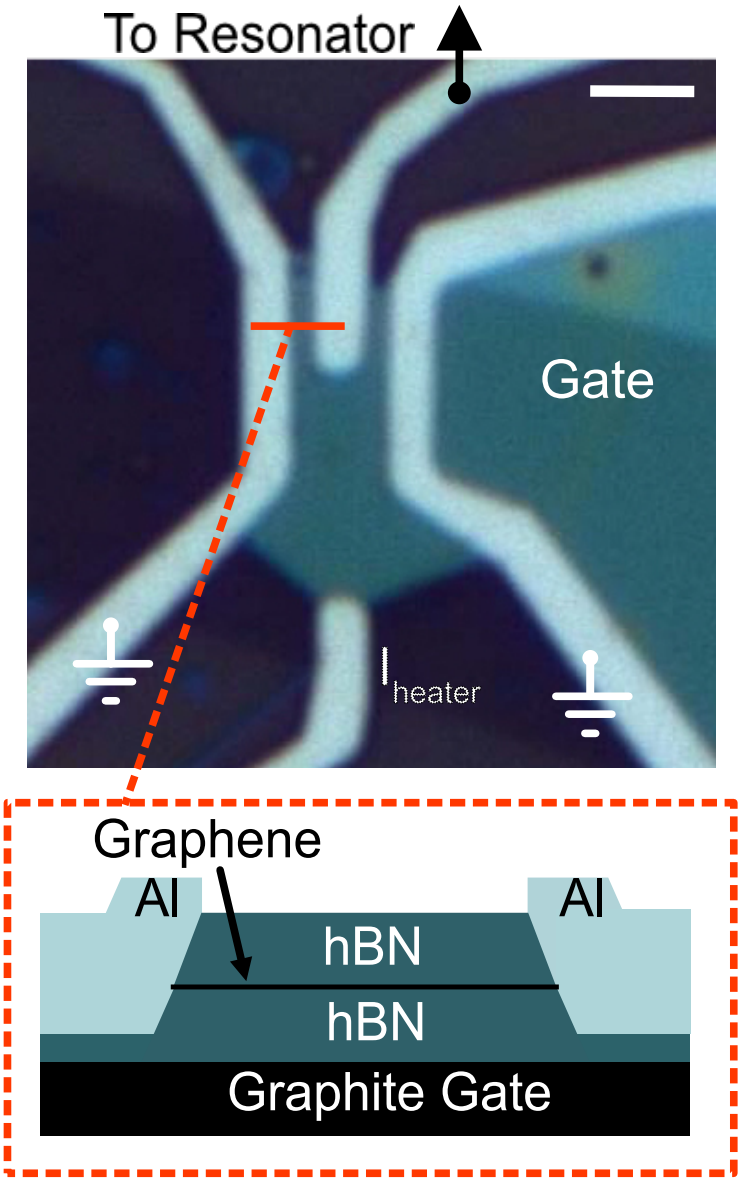

Figure 5.6: **Optical Image of Graphene Flake.** Optical image showing the graphene flake encapsulated in hexagonal boron nitride (blue-green) and contacted by aluminum electrodes (light blue). Two ground wires span the entire length of the flake. The top contact is placed in close proximity to the ground wires to form gJJ. The bottom contact placed far from the ground electrodes and can be used to apply Joule heating via heater current (I_{heater}). The inset shows the partial cross-section across the gJJ. Encapsulated graphene is contacted at the edges to form the superconductor-graphene-superconductor (S-G-S) junction. The metallic contacts consist of superconducting Al and a thin (5 nm) adhesion layer of titanium (not shown). Tuning the global carrier density in the graphene flake is achieved by applying a DC voltage V_{BG} to a graphite backgate.

5.3 Transmission Line Resonator

Since transmission lines are key devices for routing microwave and RF signals, we briefly give a background discussion here (the interested reader is encouraged to consult Pozar's excellent text for further information [75]). Subsequently, we show how the patterened NbTiN realizes a transmission line resonator.

Transmission Line Background

Stated simply, a transmission line is a medium through which disturbances can propagate as waves. Good transmission lines allow waves to be routed from one location to another with minimal attenuation. The architecture of a transmission line can be thought of as a series of 'unit cells' strung one after another, where each unit cell is a simple resonant system. Thus, for each type of resonant system, e.g. a mass-on-a-spring or an LC circuit, there is a corresponding transmission line which carries the associated waves, e.g. a series of alternating masses and springs carrying compressive or transverse waves or a series of alternating inductors and capacitors carrying voltage and current waves.

To route waves from one place to another, a transmission line requires two properties: a *restoring force* and *inertia*. To illustrate the dependence of wave propagation on these two properties, imagine we have a transmission line composed of a series of alternating identical masses and identical springs and suppose we are interested in a transverse waves propagating through this medium, i.e. the deflection of the mass along the y-axis if the masses and springs at rest lie on the x-axis. When a given mass deviates from rest, i.e. is deflected up or down, the restoring force arising from the springs pulls it back toward the rest position. Further, the inertia of the mass allows it to maintain a velocity even in the absence of an applied force, which implies that the mass may move from positive deflection, through the zero-crossing, to negative deflection, and vice versa.

With these two properties, a disturbance can propagate as a wave, according to the standard wave equation

$$\frac{\partial^2 u}{\partial t^2} + c^2 \frac{\partial^2 u}{\partial x^2} = 0 \tag{5.1}$$

which describes a deflection u propagating along a transmission line with wave speed c. We show how the discussion in the previous paragraph is borne out by the wave equation. The equation tells us that the acceleration of a section of the

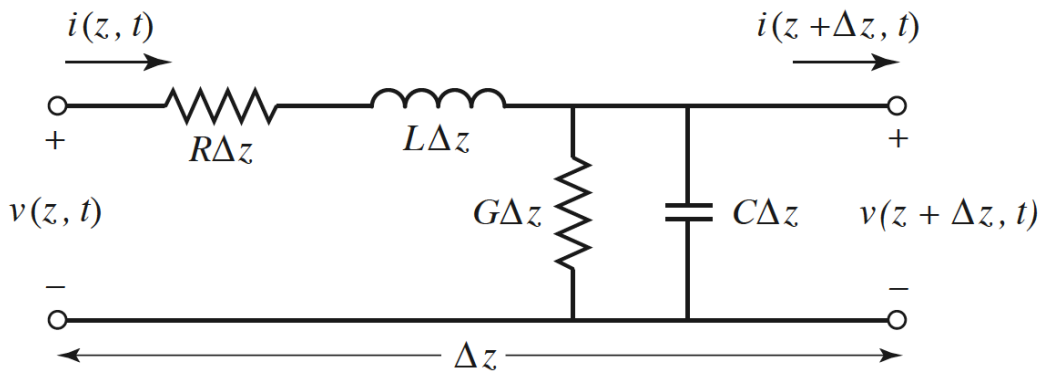

Figure 5.7: **Unit Cell of Transmission Line, from M. Pozar [75]**

transmission line ($\frac{\partial^2 u}{\partial t^2}$) is proportional to the curvature of the line at that section ($\frac{\partial^2 u}{\partial x^2}$). For a sinusoidal wave, this is in accordance with the fact that the restoring force is greatest at the peak of the sinusoid, where the curvature is greatest. Conversely, the restoring force vanishes at the zero-crossing of the sinusoid, where the curvature also vanishes. This latter case demonstrates the importance of the *inertia* of the transmission line, in the following sense: although the curvature and restoring force vanish at a zero crossing, the inertia of transmission line allows for a non-zero velocity ($\frac{\partial u}{\partial t}$ = const.) which allows the mass to move through the zero-crossing and deflect until it is stopped by the restoring force, at which point the process repeats. Thus, the potential energy stored in the curvature is converted to kinetic energy of the undeflected section, back to potential energy, and so on.

Since we are interested in routing waves of voltage and current in our device, we use a transmission line based on a series of alternating inductors and capacitors, with unit cell shown in Fig. 5.7. In the limit of a dissipationless transmission line, the per-length series resistance R vanishes, as does the per-length shunt conductance G. We can think of the primary purpose of the per-length inductor L and capacitor C as controlling the flow of free charge. When there is a non-zero charge on its plates, the capacitor produces a restoring force that pushes on the charge. Meanwhile, the inductor produces an inertia which keeps charge moving even when the capacitor is uncharged. In this way, we have an analogy to mass/spring transmission line. Since a non-zero charge on the capacitor produces a voltage drop across the capacitor and a non-zero charge flow through the inductor produces a current, the disturbances which propagate along this transmission line are voltage and current waves.

As mentioned above, a key parameter of the transmission line is the wave speed c, which is set solely by the per-length inductance L and the per-length capacitance C. Another interesting property of the propagating voltage and current waves is that their ratios are in a fixed proportion to each other when viewed in complex space, where the two waves are 90° out-of-phase with one another. This proportionality constant is known as the characteristic impedance Z_0 of the transmission line and it is also set entirely by the per-length inductance L and per-length capacitance C of the transmission line.

Although we omit a derivation here, the propagating voltage and current can be expressed as coupled variables in a linear 2D system, where the wave speed can be derived as the eigenvalue and the characteristic impedance can be derived from the eigenvector of this linear 2D system.

Once a transmission line can be engineered, it becomes straightforward to design a resonator. All that is required is an architecture which defines boundary conditions on either end of some length of the transmission line. If this is done, a series of resonant modes will exist in this system which respect the wave equation in the medium and the boundary conditions at the ends. For example, if one end of the length of transmission line is shorted such that the voltage $V(x = L) = 0$, while the other end is electrically open such that voltage $V(x = 0) = V_{max}$, then a series of modes will exist in this system with the lowest mode enforcing that the length of the resonator L equals one quarter-wavelength of the mode, i.e. $L = \frac{\lambda}{4}$. For obvious reasons, this is referred to as quarter-wavelength or $\frac{\lambda}{4}$ resonator. Thus, by engineering such a structure, we can engineer an electrical resonator with a resonant frequency convenient for our measurements.

NbTiN Transmission Line Resonator

We now discuss the architecture of the resonator/graphene device. As we will show, the coupling capacitor, transmission line, and termination realize a tunable $\lambda/4$ resonator. Refer to Fig. 5.8 for the following discussion.

The transmission line is of coplanar waveguide (CPW)-type and is loaded by a series of stubs to increase the specific capacitance C and lower the characteristic impedance Z_0 of the line. The interdigitated NbTiN coupling capacitor is co-fabricated with the transmission line in the same mask and etch step. The coupling capacitor exists on the probe port side of the resonator, where two wirebonds make contact with the on-chip pad to the external RF lines of the sample box and fridge. This allows

RF signals to be routed down to the device and transmitted out to the 4K CIT LN2 cryoamp for the S_{21} measurement. The high impedance of the coupling capacitor enforces the condition that $V = V_{max}$ on the port side.

On the opposite side, the transmission line is terminated by the low-impedance inductance of the S-G-S junction, which presents the Josephson inductance L_J to the transmission line. One side of the S-G-S junction contacts the NbTiN resonator, while the other side is grounded to the fridge. In the case of $L_J = 0$, the boundary condition is $V = 0$ and the device realizes a true $\lambda/4$ resonator. The additional small L_J lifts the voltage of the boundary condition to some $V > 0$, which has the result of increasing the effective wavelength (lowering the resonant frequency) of the resonant mode. Thus by varying L_J, which can be done by increasing the electron temperature or changing the carrier density of the flake, it is possible to shift the resonance and realize a mechanism for performing thermometry of the graphene electron temperature by measuring shifts in the resonant frequency of the device.

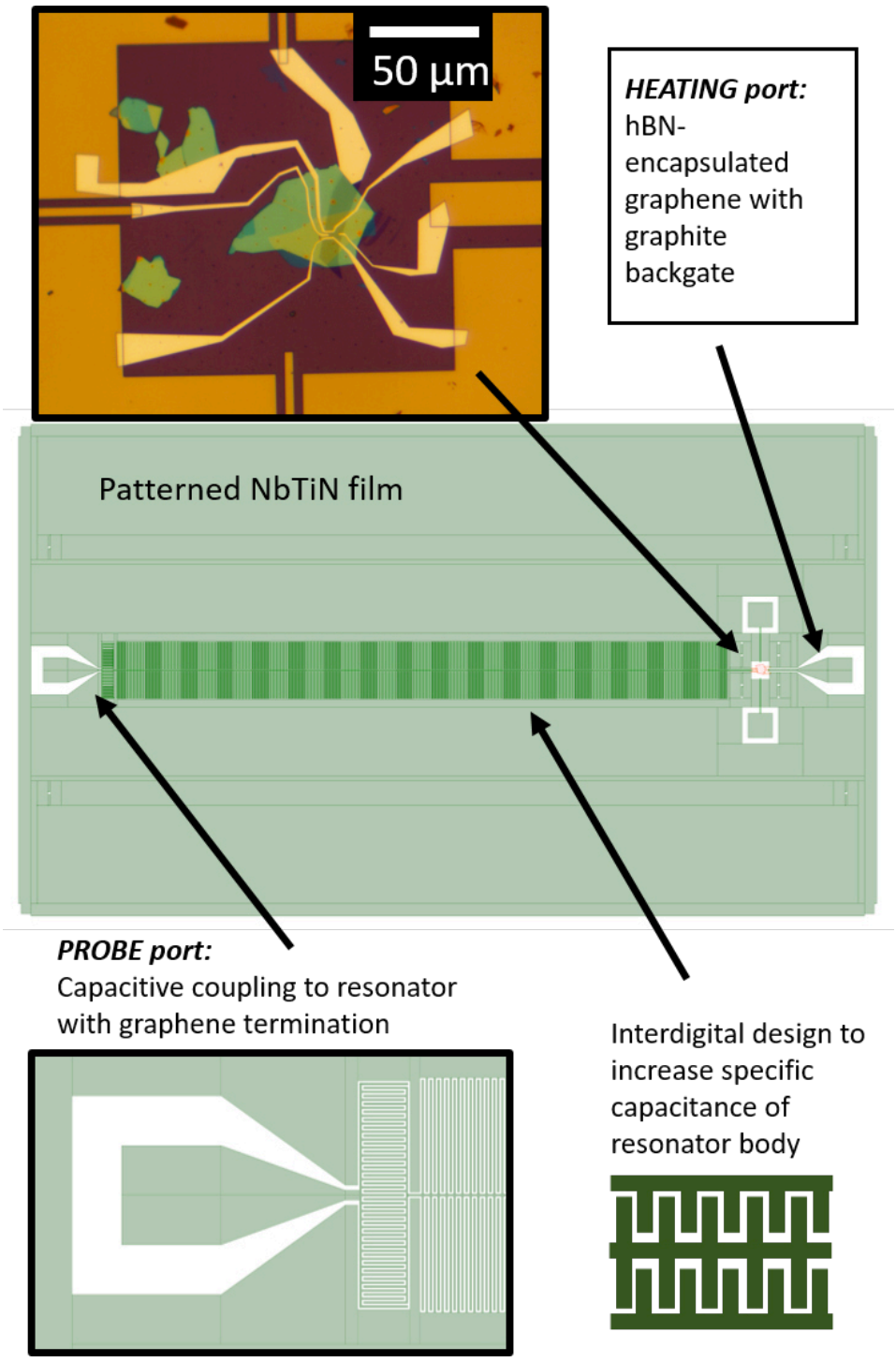

Figure 5.8: **Van-der-Waals Stack and NbTiN Resonator, borrowed with permission from Arora [4].**

Properties of the NbTiN Transmission Line

Sonnet® 15.53 is used to estimate the physical parameters of the NbTiN transmission line resonator [75] (See Table 5.1 and 5.9). The coupling capacitance C_C is estimated by fitting a set of resonances at $V_{BG} = -1.9\,\mathrm{V}$, numerically solving for C_C, and creating a histogram of extracted C_C values with mode $C_c = 0.243$ pF and standard deviation of approximately $\sigma_{C_c} = 0.02\,\mathrm{pF}$.

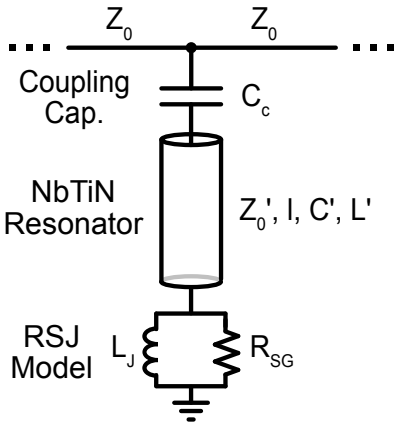

Figure 5.9: **Impedance Model** The electrical impedance model of the resonator-graphene device consists of the graphene Josephson junction in the RSJ model, a NbTiN transmission line resonator characterized by parameters in Table 5.1, a coupling capacitor C_c, and 50 Ω microwave ports.

C_C	Coupling capacitor	0.243 pF
l	TLR length	4989 μm
C'	TLR capacitance per length	3515 pF/m
L'	TLR inductance per length	1130 nH/m
Z'_0	TLR characteristic impedance	17.9 Ω
v_{ph}	TLR phase velocity	1.575×10^7 m/s
Z_0	Reference characteristic impedance	50 Ω
Z_{out}	Parallel two-port impedance	25 Ω

Table 5.1: **Coupling Capacitor, Transmission Line Resonator (TLR), and Microwave Port Parameters.**

5.4 Conclusion

In this chapter, we have done the following:

- First, we have discussed the nanofabrication procedure required to fabricate the NbTiN resonator, stamp the Van-der-Waals material stack, and deposit the aluminum electrodes.
- Second, we have reviewed transmission lines and transmission line resonators and shown how our device design implements a transmission line reasonator.

In the next section, we will discuss in great detail how the series combination of the NbTiN resonator and graphene-based Van-der-Waals stack yields a mechanism which can be used to track the temperature of the graphene flake via measured shifts in the resonant frequency of the resonator, i.e. dispersive thermometry.

Chapter 6

DEVICE CHARACTERIZATION

In graphene heterostructures, a common way of characterizing device physics is to track various measurable quantities as a function of the carrier density of the graphene flake. Since the carrier density of our device is controlled by a DC voltage applied to the backgate, we can vary the carrier density from hole-type (p-doped) through the charge neutrality point (CNP) to electron-type (n-doped). In this chapter, we perform the following:

- First, we discuss some of the benefits conferred by the graphene/resonator device architecture.
- Second, we discuss characterization of the device using a backgate voltage sweep, including the resonance fitting procedure, physics of the doping of the graphene by the aluminum contacts, Fabry-Perot-type oscillations on the hole-side, and the resistance of the heater port.
- Finally, we discuss how we can input extracted fit parameters from the resonance fits into an impedance model and extract physical parameters of the graphene Josephson junction.

Having completed this section, the reader will be well-prepared to understand the thermal characterization discussed in the next chapter.

6.1 Benefits of Resonantly-Coupled Graphene Device

The combined graphene-based Van-der-Waals stack and superconducting resonator architecture allows for straightforward frequency-domain multiplexed readout of the graphene detectors (see Fig. 6.1). As discussed in the caption of that figure, each resonator is associated with a non-overlapping portion of frequency-space, so a readout tone initialized to a single frequency will be loaded only by a single resonator. Advances in microwave electronics allow for generation of many tones in frequency space, to separately monitor each resonator. Using this scheme, readout can be performed on a single feedline using a single wideband cryogenic amplifier. The larger the bandwidth of the cryogenic amplifier, the larger the number of

multiplexable channels. For this reason, it will be useful to use a large-bandwidth, quantum noise-limited traveling wave parametric amplifier (TWPA) for readout. The novel kinetic inductance TWPA (KI-TWPA) fulfills these requirements and possesses a large dynamic range, rendering it ideal for detector applications. The interested reader is encouraged to consult the literature on these novel paramps [29], [128].

Additionally, the detection mechanism allows operation at the lowest temperatures available to a dilution refrigerator (<100mK), where graphene photodetectors are most sensitive, all the way up to 10K where liquid-He cryostats may be employed in place of expensive dilution refrigerators. Further, the readout mechanism is non-destructive, allowing the state of the photodetector to be continuously monitored with minimal backaction from the readout chain. Finally, the device architecture allows for in situ frequency tuning to compensate for non-idealities in device fabrication or to modify spectral bandwidth in real time. Taken together, the benefits of this device architecture present a significant step towards readout of arrays of graphene photodetectors for tackling the most difficult problems in radio astronomy, quantum information processing, and dark matter detection.

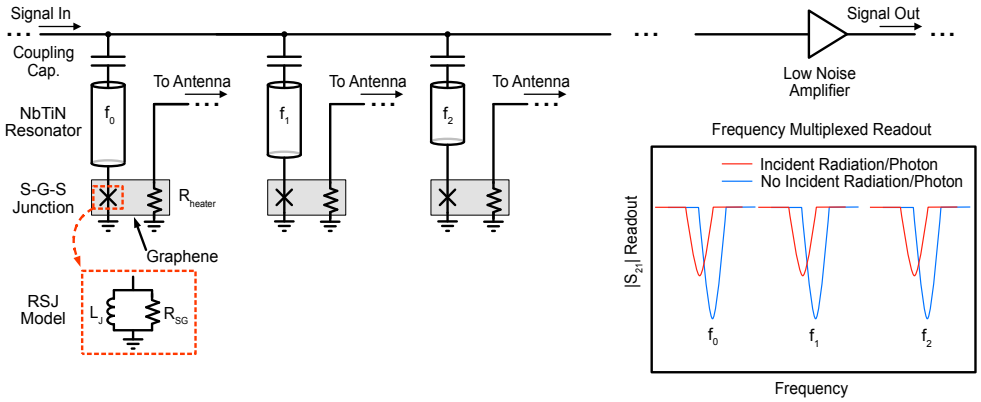

Figure 6.1: **Schematic of Frequency-Domain Multiplexed Graphene Detectors**. Here we show a schematic for frequency-domain multiplexed readout of graphene detectors. As indicated by the differing lengths of transmission line resonators, each resonator has a different resonant frequency, with a frequency profile indicated in the inset. Since the resonances are separated in frequency space by more than a linewidth, a tone sent down the feedline initialized within the linewidth of a given resonant frequency will be loaded only by that resonator and will pass by all others. Thus, an array of detectors can load the same feedline and be read out with a single, wideband cryogenic amplifier.

6.2 Resonance vs. Backgate Voltage

The resonator-coupled gJJ allows us to probe the response of the gJJ supercurrent to changes in electron density and temperature[101, 117]. Since the gJJ acts as an additional inductive element, it modifies the resonant frequency, which we monitor through microwave reflectometry. The parameters characterizing the gJJ, the Josephson inductance $L_J = \frac{\Phi_0}{2\pi I_c}$ and subgap resistance R_{SG}, depend strongly on electron density (see the next section). Accordingly, the resonant frequency and spectral width are both highly dependent on the back gate voltage V_{BG}[101].

The first set of characterization measurements performed on the device involve varying the backgate voltage, which serves as a proxy for the carrier density of the graphene flake, and observing the resulting dispersive shifts of the device. By fitting the resonance feature, we can extract resonance parameters and input them into an impedance model to numerically solve for the physical parameters of the S-G-S junction terminating the NbTiN resonator.

Backgate Voltage Sweep

In Fig. 6.2, we see the magnitude of the resonance feature, as measured by an S_{21} measurement, as the backgate voltage is swept from electron doping through charge neutrality to hole doping. As indicated by the arrows, the resonance feature starts at a large resonant frequency at large electron doping, reaches a minimum resonant frequency at charge neutrality, and increases again in frequency for large hole doping. A colormap of this backgate voltage sweep can be found in Fig. 6.3. As will be discussed in the subsequent sections, this behavior arises from the large critical current I_c found at large electron and hole doping and the minimal critical current I_c found at charge neutrality.

Figure 6.3 shows how the resonance changes as a function of V_{BG}. The maximal tuning of resonance frequency f_0 with V_{BG} occurs in the range $[V_{CNP}, V_{CNP} + 0.3\,\mathrm{V}]$, where the $\frac{\partial f_0}{\partial V_{BG}} \approx \frac{670\ \mathrm{MHz}}{1V}$. Assuming a parallel-plate capacitance of hBN ($\epsilon_r = 3$) and a separation $d = 30$ nm between the graphene flake and backgate, $\frac{\partial f_0}{\partial n_{carrier}} \approx \frac{1.21\ \mathrm{GHz}}{10^{12}/\,\mathrm{cm}^2}$. Since we estimate the area of our graphene flake to be $A = 25\mu m^2$, the maximum sensitivity of our device used as an electrometer is $\frac{\partial f_0}{\partial N_{carrier}} = \frac{4.84\ \mathrm{kHz}}{1\,\mathrm{e}^-}$.

Resonance Fit Function

Fitting of the resonance feature follows the procedure in Ref. [43]. Background-subtracted S_{21} transmission data is fit to a four-parameter fitting function

$$S_{21} = 1 - \frac{Q_0/Q_c - 2iQ_0\frac{\delta\omega}{\omega_0}}{1 + 2iQ_0\frac{\omega-\omega_0}{\omega_0}}$$

Extracted fit parameters include resonant frequency ω_0, internal quality factor Q_i, coupling quality factor Q_c, and asymmetry parameter $\delta\omega_0$. Total quality factor is defined as the parallel sum of the dissipation channels $\frac{1}{Q_0} = \frac{1}{Q_i} + \frac{1}{Q_c}$. Error bars in Fig. 2b-d correspond to the 95% (2σ) confidence level calculated from the covariance matrix of the fits. An asymmetry in the resonance circle can cause the diameter of the resonance circle to occur off of the real axis. Such an asymmetry may arise from a non-negligible line inductance or mismatched input/output impedance.

For each backgate voltage point in the sweep, the resonance can be fit to this function and the resonance parameters f_0, Q_i, and Q_c can be extracted. In the subsequent sections, we will see how these parameters can be fit to an impedance model to solve for the physical S-G-S junction parameters.

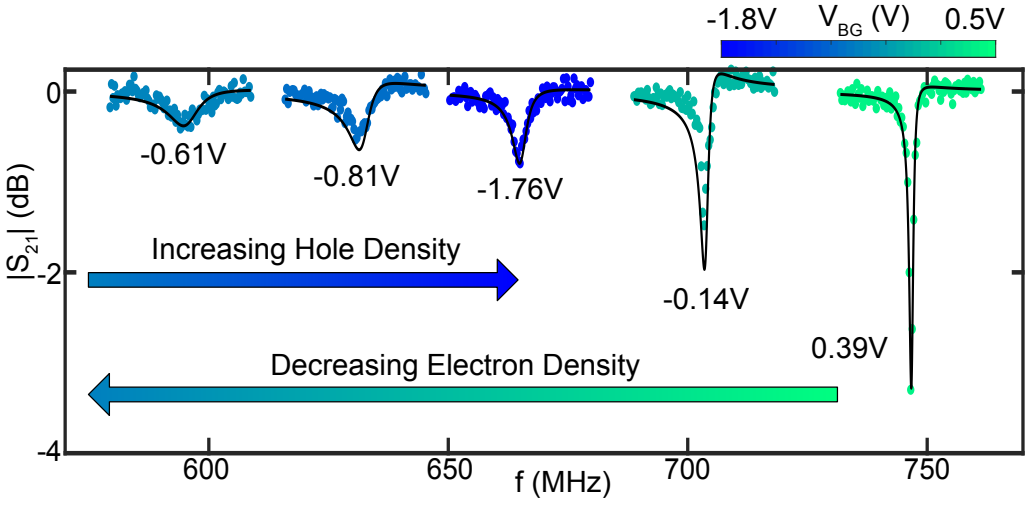

Figure 6.2: **a**, Representative $|S_{21}|$ data and fits for electron and hole doping. Color and labels denote backgate voltage V_{BG}. Arrows show the direction of resonant frequency shifts as V_{BG} is swept from positive voltage (electron doped) to negative voltage (hole doped) through charge-neutrality. Green arrow shows the resonant frequency approaching 500 MHz as electron-doping decreases to charge neutrality. Blue arrow shows that the resonant frequency increases away from 500 MHz as hole-doping increases.

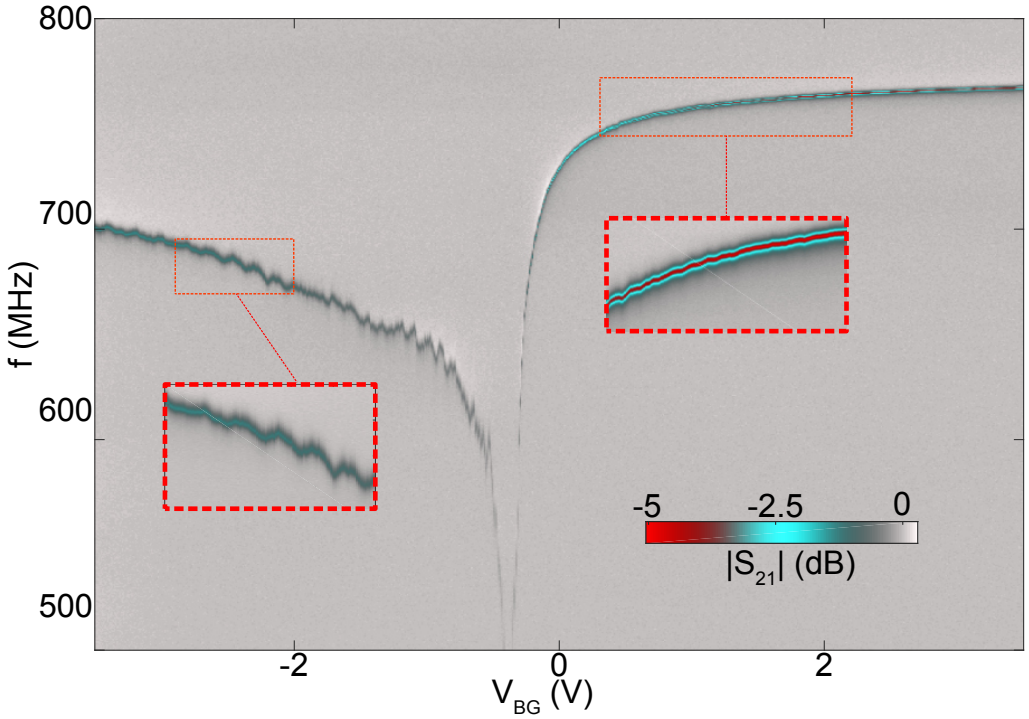

Figure 6.3: **c**, $|S_{21}|$ vs. V_{BG} shows the resonant frequency of the device as a function of electron density as tuned by the back gate. Near the charge neutrality point (CNP; $V_{CNP} = -0.3$ V), the gJJ maximally loads the resonator and consequently minimizes the value of resonant frequency. Far from the CNP, the gJJ acts as a low-inductance termination to the resonator and the resonant frequency approaches its maximum. On the hole-side ($V_{bg} < V_{CNP}$), Fabry-Perot type oscillations are visible due to formation of the regions of different doping in the graphene (hole doping; p-type) and in vicinity of contacts (electron doping n-type)[101].

6.3 Heater Port Resistance Measurement

While we cannot perform a 4-wire measurement directly on the S-G-S junction, we can do so on the heater port to determine the resistance of the port as a function of backgate voltage (see Fig. 6.5). Here, we observe features in agreement with the behavior of the resonance under a backgate voltage sweep. Since many of these features result from n-doping of the graphene in a boundary layer around the aluminum contacts, we make a brief aside to discuss doping of graphene by metallic contacts.

Metal-Graphene Doping

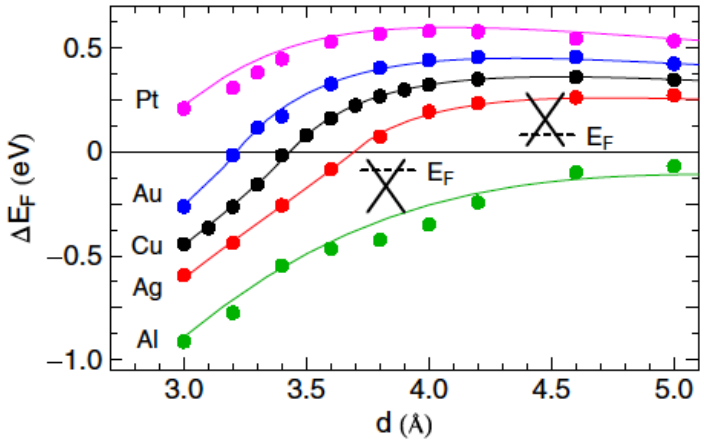

Figure 6.4: **Fermi Level Shift At Metal/Graphene Interface, from Giovannetti et al. [45]**. Plotted is the Fermi level shift as a function of displacement between surfaces for different graphene/metal interfaces. A negative Fermi level shift corresponds to n-doping of the graphene, and a positive Fermi level shift corresponds to p-doping of the graphene. For the entire range of displacements, aluminum is expected to n-dope the graphene flake. Figure taken from [45]

It has been found experimentally that aluminum leads consistently n-dope (electron-dope) the graphene around the leads. We now provide an argument why this is the case, according to reference [45]. From standard solid-state theory, the work function difference determines the doping when two dissimilar materials are brought into contact, e.g. a metal and a semiconductor brought into contact yield a Schottky diode. Briefly, the work function is the positive energy difference between the vacuum energy and the Fermi energy, $W = E_{vac} - E_F$, so the work function difference

of two dissimilar materials $\Delta W = -\Delta E_F$ is the negative of the difference between their Fermi energies. Due to the work function difference (analogously, the Fermi energy difference), charge will move to establish an equilibrium potential between the two materials brought into contact. Intuitively, we can think of the reason for this phenomenon as follows: if the Fermi energy E_{F1} of material 1, a metal, is larger than that of material 2, a semiconductor, then $E_{F1} > E_{F2}$ and electrons from the metal can fall into the semiconductor to lower their energy. This means the semiconductor becomes n-doped near the surface. Conversely, if $E_{F1} < E_{F2}$, then electrons from the semiconductor can fall into the metal to lower their energy, which p-dopes material 2 near the surface. We note that due to Poisson's equation, the presence of a non-zero charge yields a curvature in the potential which can be interpreted as a bending of the energy bands at the interface of the two materials.

We might now expect to apply this picture to graphene/metal contacts. However, when these two materials are brought into contact, DFT calculations suggest that the work function of graphene is approximately $W_G = 4.02$ eV and the work function of aluminum is approximately $W_{Al} = 4.2$ eV, which would suggest that graphene should be *p-doped* since the Fermi energy of graphene is larger than the Fermi energy of aluminum, i.e. $E_G > E_{Al}$. Why, then, is graphene actually n-doped? It turns out that the standard solid-state formalism can only be used when the electronic wavefunctions of two materials are well-separated. In graphene/metal contacts, the equilibrium spacing between the graphene and metal surfaces is $d \approx 3.3$Å, so we must account for wavefunction overlap.

We can now ask what the graphene doping looks like for different combinations of metal and graphene. It turns out that some metals, such as platinum, deform graphene's linear band structure substantially, so that there is no longer a well-defined conical point at which the linear electron and hole bands meet. However, many metals of interest, such as aluminum and silver, weakly deform graphene's band structure. Primarily, these metals have the effect of shifting the Fermi energy relative to the conical point, resulting in an electron or hole doping of graphene.

Armed with this simplified picture, DFT calculations show that an additional energy contribution due to the exchange repulsion between the electrons in graphene and the electrons in aluminum must be accounted for to determine proper doping of the graphene. This energy contribution must be overcome for the electrons of graphene to diffuse into the metal and yield p-doping of the graphene. For equilibrium spacing of the graphene and metal interface, this energy contribution is approximately 0.9 eV,

so that the work function of Al must be greater than 0.9 eV+W_G = 0.9 eV+4.02 eV = 4.92 eV in order to cross from n-doping to p-doping. As stated before, the work function Al is approximately 4.2 eV when in contact with graphene, so the graphene remains n-doped. In conclusion, due to its work function of Al *and* graphene/metal interactions, the graphene around an Al contact should be n-doped under equilibrium conditions.

Heater Resistance

We now look to explain the features of Fig. 6.5. At charge neutrality ($V_{BG} \approx -0.3$ V), the resistance experiences a large maximum as is expected from an absence of charge carriers. For large electron and hole doping, the resistance is small relative to charge neutrality. However, we note that the hole doping resistance is larger than the electron doping resistance, which we now discuss.

Due to the work function mismatch between the aluminum leads and the graphene flake, n-type carriers from the aluminum diffuse into the graphene, forming an n-type boundary layer around the aluminum leads. When the graphene bulk is doped n-type by the backgate, this typically yields an Ohmic, low-resistance contact. However, when the graphene flake is doped p-type, at least one of the contacts will be reverse biased when current flows from one aluminum lead to the other, resulting in a larger contact resistance. For this reason, the hole-doped ($V_{BG} < V_{CNP}$) region of Fig. 6.5 possesses a larger resistance than the corresponding doping level on the electron side ($V_{BG} > V_{CNP}$).

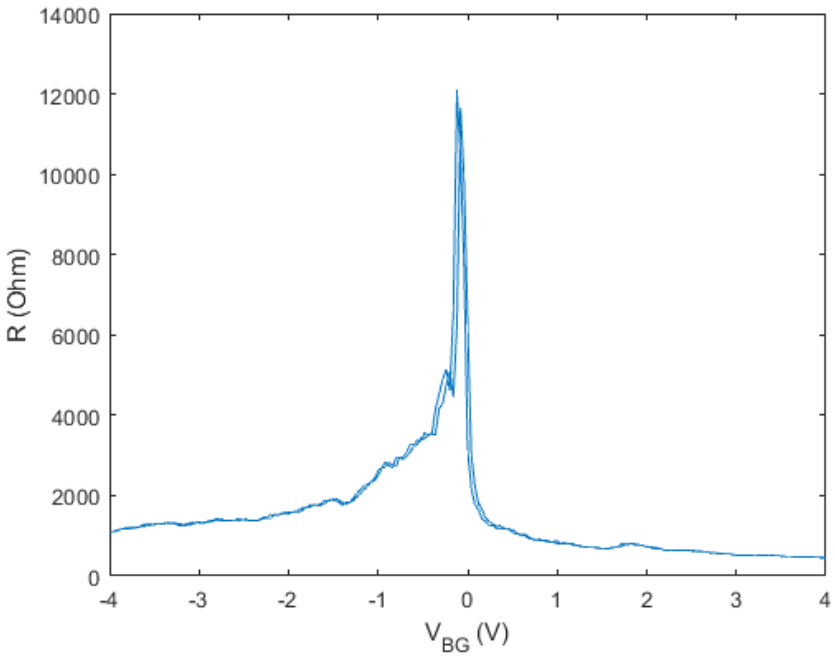

Figure 6.5: **Heater Port Resistance**. Measured resistance of the heater port (via the 4-wire measurement) is shown as a function of the backgate voltage (proxy for carrier density). The charge neutrality point exists at approximately $V_{BG} = 0.3$ V. The resistance of the hole side is larger than that of the electron side, in agreement with a non-negligible contact resistance resulting from p-n junctions on the hole-side.

Fabry-Perot Oscillations

An important observation of Fig. 6.3 is that the hole doping regime admits a series of 'oscillations' in the resonant frequency with varied backgate voltage. This is a known phenomenon arising from the coherent quantum phase of holes as they propagate through the graphene flake and reflect at the contacts [24, 22, 94, 103, 83].

In a two-dimensional electron/hole gas, the primary charge carriers are those at the Fermi surface, which propagate as plane waves with Fermi wavefector $k_F = \sqrt{\pi|n_{carrier}|}$. In ballistic graphene samples, these carriers propagate without collisions in the bulk of the graphene flake, which preserves the quantum phase evolution of the carrier. If this phase is also preserved after the carrier reflects with a contact, e.g. due to the increased resistance of a reverse-biased contact, it can interfere upon a round-trip propagation. Peaks (troughs) in the conductance, and therefore in the critical current and resonant frequency, appear when a round trip produces constructive (destructive) interference, which occurs when

$$k_F \times 2L^*_{cav} = n \times 2\pi \tag{6.1}$$

where L^*_{cav} is the effective cavity length, and n is an integer. Thus, by varying the carrier density $n_{carrier}$, and therefore k_F, it is possible to produce so-called Fabry-Perot oscillations which can be used to determine the effective cavity length L^*_{cav}.

In Fig. 6.6, modulation of the critical current $I_c(0)$ with V_{BG} on the hole side is consistent with *pnp*-type Fabry-Perot interference (we discuss how $I_c(0)$ is determined in the next sections). Following the standard method for determining Fabry-Perot cavity length in ballistic graphene, we subtract the slowly varying background with a fit to a 7^{th}-order polynomial (see Fig. 6.6 (left)) and take the power spectral density (see Fig. 6.6 (middle)). The large peak in the power spectral density is consistent with a Fabry-Perot cavity length of $L_{cav} = 361.51$ nm (see Fig. 6.6 (right)). This cavity length is consistent with the length scale of the electrode separation as patterned in the fabrication mask, where each electrode is surrounded by a n-doping layer of approximately 120 nm.

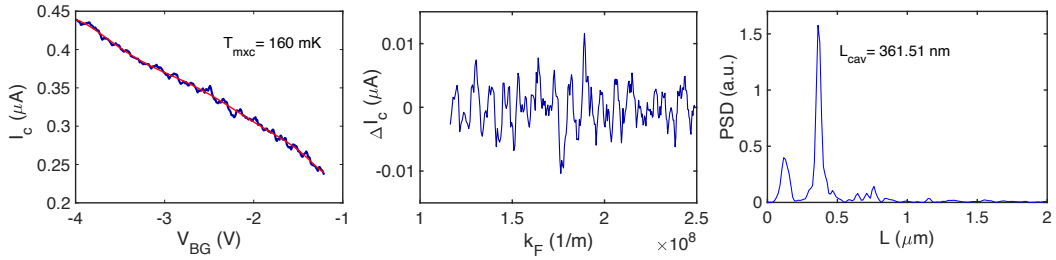

Figure 6.6: **(Left)** Hole side I_c vs. V_{BG}. Blue trace is hole side I_c data for T_{mxc} = 160 mK. Red trace is the slowly-varying background as fit to a 7^{th}-order polynomial. **(Middle)** Background-subtracted ΔI_c vs. k_F. ΔI_c is obtained by subtracting the two traces in 6.6(left). **(Right)** Power spectral density of ΔI_c. The large peak is consistent with an effective Fabry-Perot cavity length of L_{cav} = 361.51 nm.

6.4 Impedance Model

To deduce the physical parameters of the gJJ from the fit parameters of the S_{21} resonance feature, we employ an electrical impedance model of our device which takes the inputs (f_0, Q_i) and numerically solves for junction parameters (I_c, R_{SG}). *Sonnet*® 15.53 is used to estimate the physical parameters of the NbTiN transmission line resonator. The coupling capacitance C_C is estimated by fitting a set of resonances at $V_{BG} = -1.9\,\mathrm{V}$, numerically solving for C_C, and creating a histogram of extracted C_C values with mode $C_c = 0.243$ pF and standard deviation of approximately $\sigma_{C_c} = 0.02\,\mathrm{pF}$. We note that an estimate of microwave losses in the junction is not accessible from the switching current measurements that have typically been employed in gJJ threshold detection schemes.

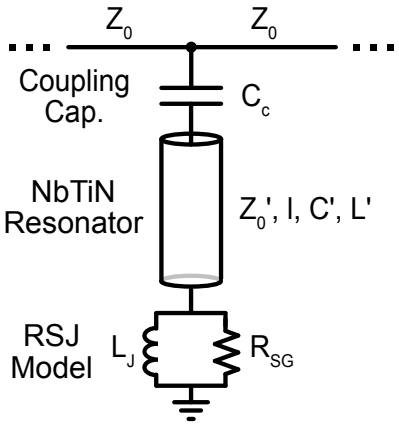

Figure 6.7: **Impedance Model** The electrical impedance model of the resonator-graphene device consists of the graphene Josephson junction in the RSJ model, a NbTiN transmission line resonator characterized by parameters in Table 5.1, a coupling capacitor C_c, and 50 Ω microwave ports.

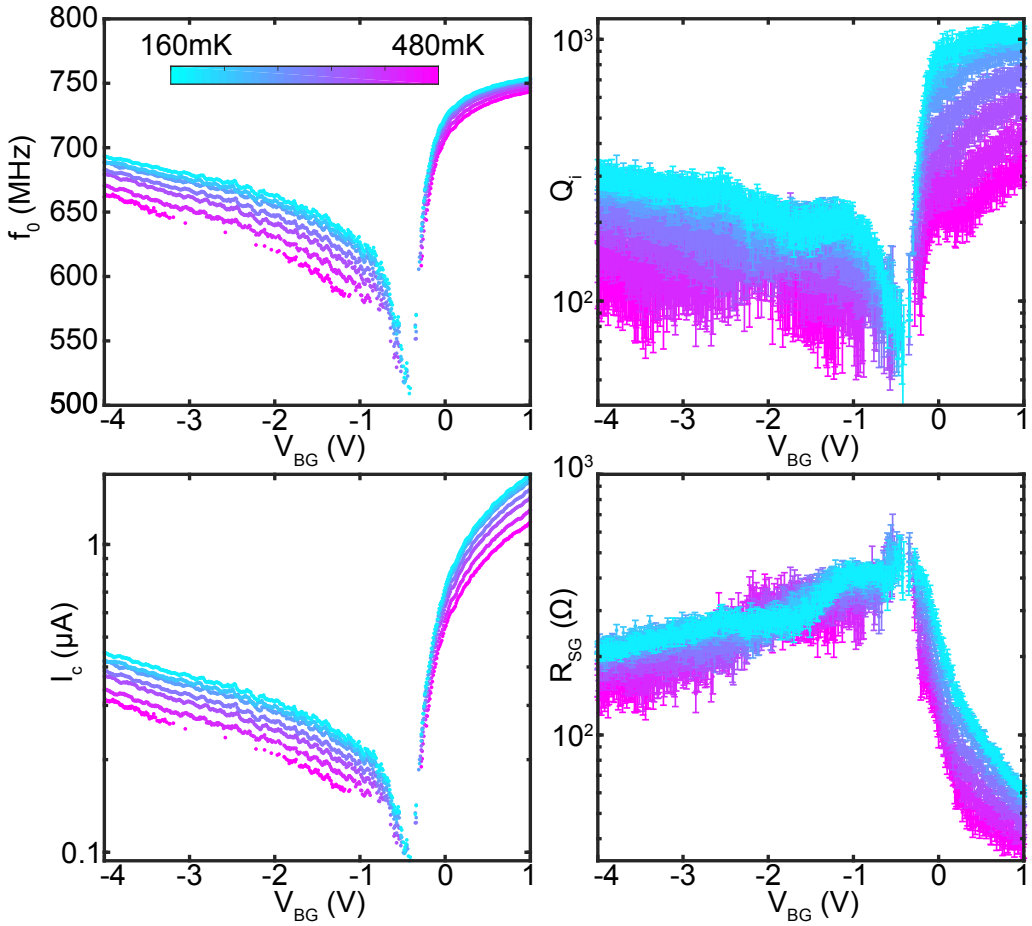

Figure 6.8: **Resonance Fits and Extracted Parameters. Top Left**, f_0 as a function of V_{BG} for representative T_{mxc} = 160, 210, 260, 310, 360, 410, 460 mK. Extracted resonant frequency f_0 as a function of V_{BG} shows a characteristic lineshape consistent with Fig 1c. As T_{mxc} increases, f_0 decreases for all backgate voltages. Near charge neutrality and for higher temperatures, the device becomes undercoupled to such an extent that fitting is unreliable. Fit parameters in these regions are not included in the plots. **Top Right**, Q_i as a function of V_{BG} and T_{mxc}. **Bottom Row**, RSJ model parameters I_c (**Bottom Left**), and R_{SG} (**Bottom Right**) as a function of V_{BG} and T_{mxc}. I_c and R_{SG} are determined using a numerical impedance model of the resonator/gJJ device with resonance parameters (f_0, Q_i) as inputs.

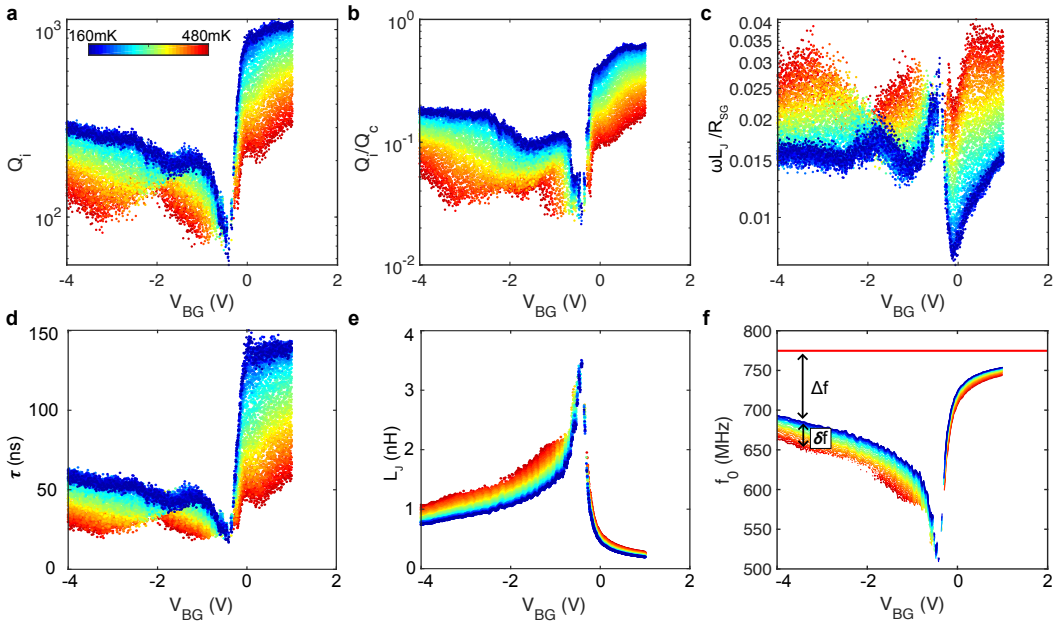

Figure 6.9: **Extracted Parameters from Resonance Fits and Impedance Model** **a.** Q_i vs. V_{BG}. The internal quality factor Q_i is extracted from the S_{21} fit function. **b.** Q_i/Q_c vs. V_{BG}. Ratio of internal quality factor Q_i and coupling quality factor Q_c (also extracted from the S_{21} fit function) shows that the device is in the undercoupled limit for all backgate voltages. **c.** $\omega L_J/R_{SG}$ vs. V_{BG}. Ratio of the inductive branch impedance to resistive branch impedance in the RSJ model. **d.** $\tau = Q_0/\omega_i$ vs. V_{BG}. The resonator time constant τ is expected to set the system time constant for all measured backgate voltages and temperatures. **e.** L_J vs. V_{BG}. The Josephson inductance $L_J = \frac{\Phi_0}{2\pi I_c}$. **f.** f_0 vs. V_{BG}. The red line corresponds to the projected unloaded ($L_J = 0\,\text{nH}$) resonance frequency. Δf corresponds to the loaded ($L_J \neq 0\,\text{nH}$) resonance frequency at $T_{mxc} = 160\,\text{mK}$. δf corresponds to further shift in the resonance frequency due to the increase in flake temperature.

6.5 Discussion of Extracted Parameters from Resonance Fits and RSJ Model

As shown in Fig. 6.8 and Fig. 6.9, our fitting and modeling procedure allows several fit and junction parameters to be plotted as a function of backgate voltage V_{BG} and flake temperature T_{mxc}.

6.9a shows a dip in Q_i at $V_{BG} = -2$V, which is propagated to the other plots 6.9b-d. This dip arises from an asymmetry in the S_{21} parameter which rotates the resonance circle off the real axis. Such rotations can arise from line impedance mismatches and parasitic couplings[43]. Since R_{SG} is determined primarily by Q_i, R_{SG} is sensitive to dissipation in the graphene flake as well as the electromagnetic environment of the flake/resonator assembly. By contrast, f_0 and I_c are largely insensitive to these effects, so our thermometry based upon the dispersive shifts of the resonance is also largely insensitive to these effects.

6.9b shows that our device for all backgate voltages is in the undercoupled limit ($Q_i < Q_c$), where dissipation occurs primarily within device instead of via the coupling to the microwave lines. The variation of the coupling quality factor Q_c is consistent with the circuit model and a constant coupling capacitor $C_c = 0.243$ pF.

The dispersive shifts of the resonance can be understood from the impedance model shown in 6.9, which consists of a transmission line resonator terminated by the junction impedance. This model predicts an unloaded ($L_J = 0$ nH) resonant frequency of $f_{unload} = 774.75$ MHz as indicated by the solid red line in 6.9f. When a finite inductance L_J loads the transmission line resonator, the resonant frequency decreases. As discussed in the previous chapter, this occurs because a change in the terminating impedance alters the boundary condition at the terminating end of the resonator. In the case of the unloaded resonator, i.e. a $\lambda/4$ resonator, the termination is a short-to-ground, which fixes the boundary voltage at $V = 0$. This enforces the resonance condition that the length of the resonator equals one quarter of the resonant wavelength, i.e. $\lambda/4 = l$. However, terminating the transmission line resonator in an inductance alters the boundary condition such that the boundary voltage amplitude is fixed at some $V = V_0 > 0$. This has the effect of enforcing the resonance condition that a quarter-wavelength is larger than the resonator length, i.e. $\lambda/4 > l$, or, analogously, that the resonant frequency is decreased relative to the unloaded case. The larger the terminating impedance, i.e. the larger L_J, the lower the resonant frequency[101, 75].

Due to higher contact transparency, electron doping should exhibit a larger supercurrent than hole doping. It follows that the electron side should exhibit a smaller L_J

than the hole side, and, correspondingly, the electron side should exhibit a smaller decrease in resonant frequency relative to f_{unload} than the hole side. This is consistent with 6.9f for electron and hole doping, i.e. $\Delta f_{electron} < \Delta f_{hole}$ where Δf is defined as the resonant frequency decrease at $T_{mxc} = 160\,\text{mK}$.

As shown in 6.9c, $\frac{\omega_0 L_J}{R_{SG}}$ is a common figure-of-merit for RF-driven Josephson junctions[112]. It compares the impedance of the dissipationless supercurrent branch to the dissipative resistive branch. A smaller value of $\frac{\omega_0 L_J}{R_{SG}}$ denotes a less dissipative device. At $T_{mxc} = 160\,\text{mK}$, $\frac{\omega_0 L_J}{R_{SG}} \approx 1.5\%$ within a factor of 2. As the temperature rises to $T_{mxc} = 400$ mK, $\frac{\omega_0 L_J}{R_{SG}}$ increases to 3%. This is consistent with decreases in I_c raising the impedance of the dissipationless branch and driving more current through the dissipative branch, as indicated by the degrading quality factor with increasing flake temperature (6.8c).

I_c vs. T Dependence and Extracted Superconducting Gap Δ

Since we cannot perform 4-wire measurements directly on the gJJ to estimate the induced superconducting gap Δ_0 via multiple Andreev reflection measurements, we perform a fitting procedure based upon the temperature dependence of the critical current $I_c(T)$.

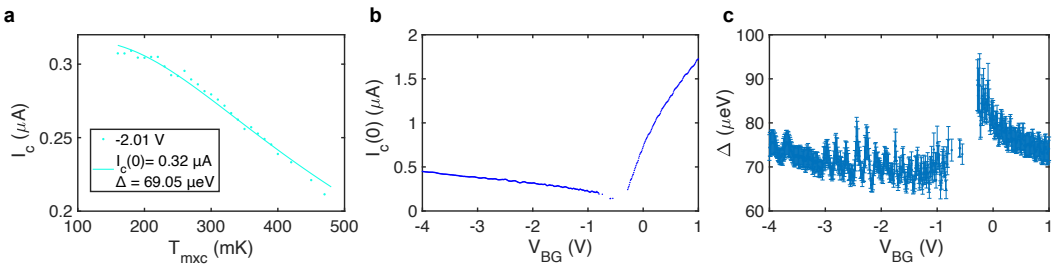

Figure 6.10: **(left)** I_c vs. T. An example fit of I_c vs. T for $V_{BG} = -2.01$ V with extracted fit parameters $I_c(0)$ and Δ. **(center)** Fit parameter $I_c(0)$ vs. V_{BG}. $I_c(0)$ fit parameter is shown for both electron and hole doping. **(right)** Fit parameter Δ vs. V_{BG}. A coarse estimate of induced gap $\Delta \approx 80\,\mu$V. Fine features are discussed in the text.

The $I_c(T)$ vs. V_{BG} data in Fig. 6.8 is fit to extract physical parameters. The fit function we employ describes the supercurrent that arises from thermally populating the Andreev bound states (ABS) in a ballistic junction[70].

$$I_c(T) = I_c(0) \tanh\left(\frac{\Delta}{2k_B T}\right)$$

The two fit parameters correspond to the physical parameters $I_c(0)$, the zero-temperature critical current, and Δ, the induced superconducting gap. An example fit is shown in 6.10a.

From 6.10c, we can make a coarse estimate of the induced superconducting gap $\Delta \approx 80\,\mu$V. However, further measurements are needed to determine whether the finer structure of 6.10c is due to the physics of the S-G-S junction or an artifact of the fitting procedure. Toward this end, it would be useful to perform simultaneous RF characterization and DC multiple-Andreev reflection measurements on a gJJ sample[101].

6.6 Conclusion

In this chapter, we have done the following:

- We have discussed benefits of resonant readout of graphene heterostructures.
- We have considered physical properties of the graphene device and related them to device measurements taken in a carrier density and stage temperature sweeps, including the Fabry-Perot-type oscillations resulting from ballistic transport in the presence of low contact transparency.
- We have discussed our implementation of an impedance model to extract gJJ parameters, as well as conclusions related to device performance resulting from these parameters.

Having characterized device performance and physics under a backgate voltage sweep, we now turn to understanding device performance and physics under heating measurements.

Chapter 7

HEATING MEASUREMENTS

7.1 Introduction

Thermal characterization of our device proceeds by applying DC Joule heat power to the monolayer graphene flake and measuring the resulting temperature shifts. To motivate and present these findings, we do the following in this chapter:

- We discuss electron-phonon scattering in the deformation potential approximation and present results for 3D scattering in a normal metal.
- We present discuss experimental verification by Roukes for the hot electron-effect in metals and similar measurements performed on monolayer graphene by Fong and Schwab.
- We discuss our heating and dispersive thermometry measurements of monolayer graphene, including the power law-dependence between applied power and electron temperature and possible interpretations based on thermalization mechanisms in ballistic graphene.

7.2 Electron-Phonon Coupling in Normal Metals

In solid-state devices at cryogenic temperatures, a key mechanism by which hot electrons thermally equilibrate with their environment is through electron-phonon scattering. To illustrate this important process, we will first discuss calculations of this rate based on the deformation potential approximation, followed by a discussion of experimental verification in metals by Roukes and similar measurements in graphene by Fong and Schwab.

Theory Background

We follow the treatment by Wellstood, Urbina, and Clarke [120]. As described by the Feynman diagrams in in Fig, 7.1, two scattering processes contribute to electron-phonon coupling. An electron can either emit a phonon and relax to a lower energy, or an electron can absorb a phonon and be excited to a higher energy. The rate at which these processes occur can be calculated using Fermi's Golden Rule [104]. For the scattering process in which an electron of wavevector k emits a phonon of

wavevector q and transitions to a lower energy state of wavevector $k' = k - q$, the rate of transition is given by

$$\frac{1}{\tau_{kk'}} = \frac{2\pi}{\hbar} M^2(q)\delta(E_{k'} - E_k - \epsilon_q)[1 - f(E_{k'})][n(q) + 1] \tag{7.1}$$

Here, we see that the transition rate is proportional to the square of the matrix element $M^2(q)$ between initial and final electron states. The delta function $\delta(...)$ enforces energy conservation for the electron and emitted phonon. The factor of $[1 - f(E_{k'})]$ gives the probability that the final electron state is unoccupied (and, thus, that scattering may proceed) where $f(E_{k'})$ is the Fermi-Dirac function, and the factor of $[n(q) + 1]$ gives the probability of phonon occupation upon emission of the phonon of wavevector q. An analogous expression holds for phonon absorption.

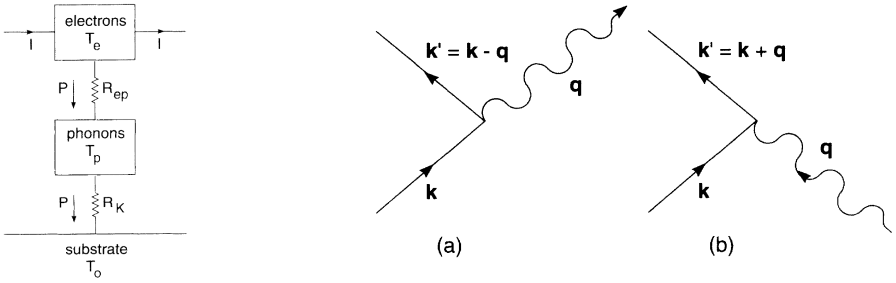

Figure 7.1: **Heat Transfer via Electron-Phonon Coupling, from Wellstood, Urbina, and Clarke [120].** (**Left**) In a standard model of thermal transport in solid-state systems, heat flow typically has two dominant sources of thermal resistance. Electron-phonon thermal resistance R_{ep} is typically limited by the slow rate of scattering between electrons and thermal phonons. The Kapitza boundary resistance R_K between thermal phonons of the solid-state system and the substrate arises from the acoustic impedance mismatch of the solid-state lattice and the environment [93]. At sub-500 mK temperatures, it is often the case that $R_{ep} > R_K$, which allows the electron temperature to rise above the phonon temperature and yield 'hot-electron' effects. (**Right**) Two key scattering processes occur between electrons and thermal phonons, as indicated by the two energy- and momentum-conserving Feynman diagrams. In one, an electron emits a thermal phonon and relaxes to lower energy. In the other, electrons can absorb a thermal phonon and be excited to a higher energy.

The physics of the electron-phonon scattering is contained primarily in the matrix element $M^2(q)$. A common approximation is that of the *deformation potential* model [125, 126]. In the following we will argue how the presence of long-wavelength

thermal phonons mediates electron scattering, and we will focus on the special case of a three-dimensional metal, though these arguments can be adapted to different solid state systems of different dimensions.

The presence of a low-energy (long-wavelength) thermal phonon serves to dilate the lattice as it passes, suppose by the dimensionless amount Δ. By virtue of this dilation, the local electron density n_0 will be diminished to $n_0(1-\Delta)$, locally shifting the Fermi energy by an amount

$$\delta V = \frac{2}{3} E_F \Delta \tag{7.2}$$

The local variation in the Fermi energy will allow charge to rearrange until the Fermi level is constant throughout the material. This means that a local region of charge will collect. By Poisson's equation, this local accumulation of charge produces an electrostatic potential of compensating energy δV. Invoking standard quantum mechanical scattering theory, this potential can mediate scattering of electrons of one state into another state. Thus, the presence of a phonon serves to mediate the scattering of electrons from one state (and energy) to another. This model yields the squared matrix element

$$M^2(q) = \frac{\hbar q}{2\rho v_s V} \left(\frac{2\varepsilon_F}{3} \right)^2 \tag{7.3}$$

We note that in a superconductor, the superconducting gap energy precludes low-energy scattering events such as these, since there exist no unpaired electronic states capable of absorbing or emitting low-energy phonons. Instead, in the case of standard *s-wave* superconductivity, electron-phonon coupling in the presence of filled Fermi sphere serves to produce an attractive interaction between two electrons [44]. Due to the presence of the Fermi sphere, this attractive interaction will yield a bound state between the electrons *no matter how small the attraction*, which will be separated by a finite energy from unpaired electronic states—this bound state is known as the *Cooper pair*. For this reason, it is said that a superconductor is 'gapped to excitations' and this property is responsible for much of the interesting physics of these materials.

Returning to the main line of argument and guided by this model of electron-phonon scattering, one can use the scattering rate to calculate the average loss of energy from the electron via phonon emission

$$\frac{dU}{dt} = -\frac{\varepsilon_q}{\tau_{kk'}} \tag{7.4}$$

To calculate the net power emitted by the electron gas, one can integrate over all phonon and electron contributions to the scattering process which produces the 3D collision integral

$$P = \frac{dU}{dt} = \int_0^\infty f(k) D_e(k) d^3k \int \frac{dU_{kk'}}{dt} D_p(q) d^3q \tag{7.5}$$

Evaluating this integral (and the analogous one for phonon absorption) gives the final expression for the net power emitted via electron-phonon scattering in a 3D metal

$$\Delta P = \Sigma V (T_e^5 - T_p^5) \tag{7.6}$$

where the electron-phonon coupling constant is given by

$$\Sigma = \frac{\hbar}{2\rho v_s} \left(\frac{2\varepsilon_F}{3} \right)^2 \frac{D(E_F) k_B^5 \Gamma(5) \zeta(5)}{2\pi \hbar^5 v_s^3 v_F V} \tag{7.7}$$

Experimental Verification of the Hot Electron Effect in Thin Metal Films

Roukes et al. [97] measured the hot electron effect in metal films, a phenomenon occurring at cryogenic temperatures in which the electron temperature of a metal rises above the temperature of the lattice phonons. This can be understood from the different timescales involved in heat transport through the system. The rate at which heat from the applied bias field is transferred to the electrons is set by the electron-impurity scattering rate, which is largely temperature independent and results from elastic scattering events. The rate at which hot electrons cool via phonon emission is set by the electron-phonon coupling rate. Since it is typically much slower than impurity scattering, it produces an effective thermal resistance R_{ep}. Finally, the rate at which lattice phonons transfer heat to the environment is typically limited by the Kapitza boundary resistance R_K between the lattice and the environment. A common model for the emergence of the Kapitza resistance is

based upon the difference between the speed-of-sound (and, therefore, the phonon momenta) of dissimilar materials which impedes the passage of thermal phonons from one material to another and which can yield a temperature difference between the two materials. In the thermal model of Fig [], when the thermal resistance of electron phonon coupling $R_{ep} > R_K$, a 'bottleneck' in heat flow can occur such that the electrons rise to a well-defined temperature in excess of the temperature of the lattice phonons.

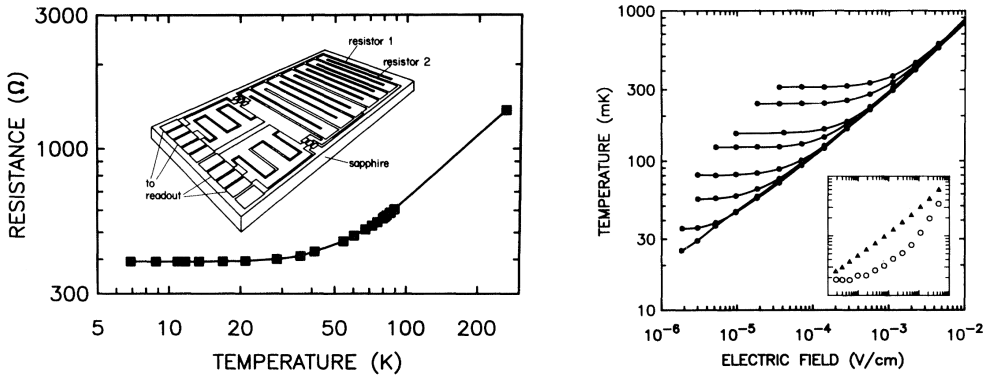

Figure 7.2: **Experimental Demonstration of the Hot Electron Effect, from Roukes et al. [97]. (Left)** Example of the dependence of copper film resistance on temperature, with resistance saturating below ~50 K. **(Right)** Electron Temperature vs. Applied Bias Voltage. The power law dependence is in agreement with electron-phonon scattering calculations for 3D electrons and phonons in metal films under the deformation potential approximation. Inset shows that the electron temperature is elevated relative to the phonon temperature up to approximately the $R_{ep} \sim R_K$ crossover.

In the experiment, noise thermometry was performed on two co-fabricated but galvanically-isolated metal films with a tight thermal coupling between them via the substrate. A bias was applied to one of the two films inducing a temperature rise of the electrons of that film, and the electronic and phononic temperatures were subsequently measured.

The films consisted of 100-nm-thick evaporated copper on a thin mono-crystalline sapphire substrate. Since the resistance of the copper films typically saturates at approximately 200 Ω from 15 mk-10 K, DC SQUID noise thermometry was performed to track the temperature of the two films down to 20 mK [57, 56]. Noise thermometry of the biased resistor yielded a measurement of the elevated electron temperature while noise thermometry of the unbiased resistor yielded measurement

of the lattice (phonon) temperature. The latter was possible since the spacing of the two resistors (40 μm) was much smaller than the phonon mean free path, so a negligible thermal gradient was expected. The DC SQUID amplifier had an effective measurement bandwidth of ~6 kHz, and coupled energy sensitivity of 30$\hbar$, and was impedance matched to the high-impedance films by a superconducting transformer.

The results demonstrated a difference in electronic and phononic temperatures from 20mK to 320mK (see 7.2, left panel inset), with the electron temperature being in excess of the phonon temperature until approximately $R_K \sim R_{ep}$. A power law dependence between applied power and temperature increase was in agreement with the standard model of electron-phonon coupling in metals $P \propto T_e^5 - T_{ph}^5$, as demonstrated by Wellstood's calculation in the previous section [120, 3, 41].

7.3 Electron-Phonon Coupling in Monolayer Graphene

Calculation of Electron-Phonon Coupling in Monolayer Graphene

In graphene, the 2D population of electrons is scattered by a 2D population of thermal phonons [113]. Due to the linear band structure of monolayer graphene, an electron of wavevector k has energy $E_k = \hbar v_F |k|$, for Fermi velocity v_F. The phonons involved in scattering are 2D longitudinal acoustic phonons, where a phonon of wavevector q has energy $E_q = \hbar v_s q$, for speed of sound v_s. In the low-temperature limit, we can make the approximation $q << 2k$. This allows expansion of the Dirac-Fermi function to first order in $\hbar\omega$, i.e. $f(E_k) - f(E_k + \hbar\omega) \approx \hbar\omega_q \delta(E_k - E_F)$. Under these conditions, the collision integral becomes proportional to the Riemann-Zeta function

$$P = F(T_e) - F(T_{ph}) \tag{7.8}$$

$$F(T) \propto \int_0^\infty dq q^3 N_q(T_{ph}) \tag{7.9}$$

where $N_q(T)$ is the Bose-Einstein occupation factor at temperature T. Performing the integration, the relation between applied heat power P and electron T_e and phonon T_{ph} temperature is

$$P = A\Sigma(T_e^4 - T_{ph}^4) \tag{7.10}$$

with electron-phonon coupling constant

$$\Sigma_{ep} = \frac{\pi^2 D^2 E_F k_B^4}{15\rho\hbar^5 v_s^3 v_F^3} \tag{7.11}$$

Experimental Verification

Fong et al. [40] and Fong and Schwab [39] performed Johnson noise thermometry on monolayer graphene and deduced several key thermal characteristics.

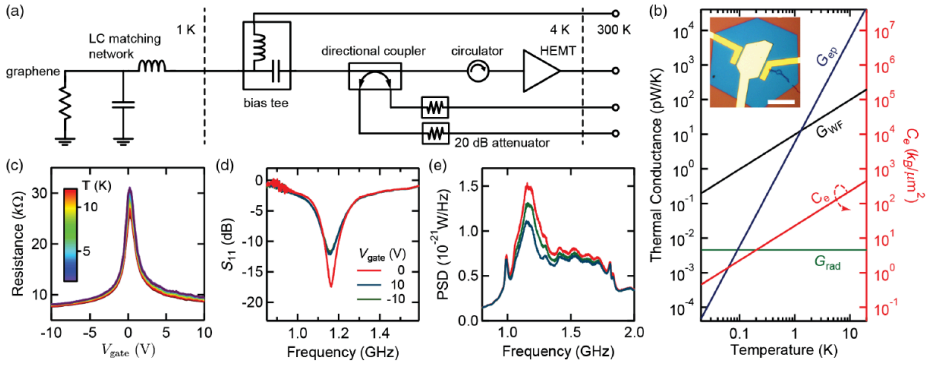

Figure 7.3: **Measurement Circuit for Johnson Noise Thermometry of Monolayer Graphene, from Fong and Schwab [39].** Circuit diagram shows the impedance matched ~ 30 kΩ to the 50Ω measurement circuit and HEMT via the LC-tank circuit. Additional plots show measurements of the circuit, including the noise PSD which peaks at approximately 1.16 GHz.

In their setup, a flake of monolayer graphene was stamped on SiO_2 and a resistive region of ~30 kOhm was contacted by metallic probes. To achieve an electrical impedance match between this high-resistance region of the graphene and the 50 Ohm measurement circuit, a superconducting NbTiN lumped-element LC tank circuit was employed, with resonant frequency of 1.16 GHz and an 80 MHz bandwidth. The first stage amplifier was a $T_N = 4K$ cryo-HEMT.

The Dicke radiometer formula [31] calculates the measurement precision of the temperature from the number of independent measurements of the noise, which yields the following relation between the electron temperature T_e, the system temperature T_s, the measurement bandwidth B, and the integration time t_m

$$\frac{\delta T_e}{T_e + T_s} = \frac{1}{\sqrt{B \times t_m}} \tag{7.12}$$

where in the experiment the measurement bandwidth was $B = 80$ MHz and the measured system noise was $T_s = 12$K. From the formula, at $T_e = 2$K the electron temperature noise density is $\sqrt{S_T} = 2mK/\sqrt{Hz}$. As shown in Fig. 7.4, the dependence of $\frac{\delta T_e}{T_e+T_s}$ upon B and t_m follows the Dicke radiometer formula to excellent precision.

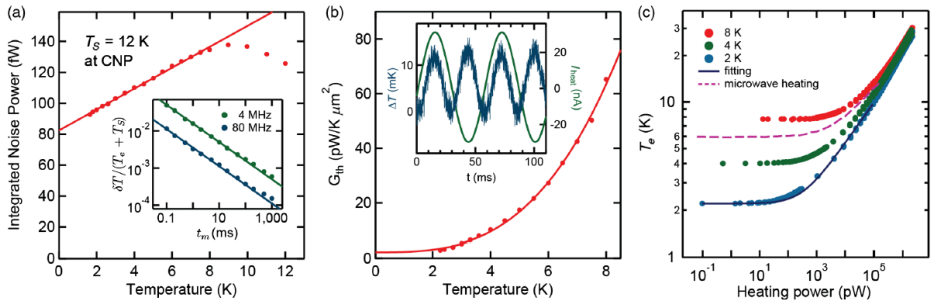

Figure 7.4: **Thermal Measurements of Monolayer Graphene, from Fong and Schwab [39]. (left)** Integrated Noise Power vs. Temperature. Dependence is agreement with the Johnson Noise Formula. The inset plot shows that the measured precision of the temperature is in agreement with the Dicke radiometer formula. **(center)** Thermal conductance G_{th} vs. Temperature exhibits a temperature dependence consistent with $P \propto T_e^4 - T_{ph}^4$. Inset shows that a heater current applied at ω yields a temperature modulation at 2ω. **(right)** Electron temperature vs. Applied Joule heat power.

With this measurement setup in place, it was possible to perform heating measurements in which Joule heat was applied to the graphene flake and the resulting electron temperature was measured. As seen in Fig. 7.4, applied AC heater current at ω generated the expected 2ω response in electron temperature. Further, a scaling law of $P \propto T_e^4 - T_{ph}^4$ was found, in agreement with standard electron-phonon coupling theory for monolayer graphene.

7.4 Heater Measurements

To characterize the thermal properties of the gJJ device, we employ a measurement configuration in which the graphene flake is heated by applying a DC current I_{heater} to a resistive heater port. The port electrode is placed sufficiently far from the ground electrodes to preclude supercurrent flow. This configuration allows us to accurately monitor the input power delivered to the graphene flake while simultaneously monitoring the resonance frequency. For different device temperatures and

doping, representative changes in the S_{21} resonance dip are shown in Fig. 7.5a-c and Fig. 7.5f-h. By increasing the stage temperature from 170 mK to 400 mK, we observe a decrease in the resonant frequency of 27 MHz for holes, compared to 6 MHz for electrons. This is consistent with greater inductive loading (lower I_c) in the hole regime. By applying a heater current I_{heater}, the internal flake temperature T is increased above T_{mxc}, decreasing the resonant frequency. Combined with the measurements taken at different temperatures for calibration (Fig. 7.5e,j) the power vs. temperature characterization and, consequently, the thermal conductivity G_{th} of the graphene flake can be determined. We use this approach to investigate thermal properties for both electron and hole doping regimes.

The data we have acquired is consistent with a power law $P_{heater} = \Sigma A(T^n - T_{mxc}^n)$, with electron temperature T, stage temperature T_{mxc}, scaling exponent n and the electron-phonon coupling prefactor ΣA. We plot $\partial P/\partial T = G_{th} = n\Sigma A T^{n-1}$ (7.6c) which shows that the scaling exponents for hole and electron doping are consistent with $n = 5$. We note that our fitting procedures produce only comparably small errors for each of the individual data points and, accordingly, the uncertainty of the extracted scaling exponent is much less than 1. This enables us to clearly distinguish that the exponent obtained here is *not* consistent with the $n = 3$ or $n = 4$ scaling predicted for bulk electron-phonon coupling in reduced dimensions[113, 25]. While an $n = 5$ scaling exponent is expected for the electron-phonon coupling of a 3D electron gas[97], these considerations do not apply for our graphene device in which the electron and phonon density-of-states are 2D.

In Fig. 7.5a-c and f-h, we note that the relative decrease in resonance frequency is greater on the hole side than the electron side. In the previous chapter, we observed $\Delta f_{electron} < \Delta f_{hole}$ where Δf is defined as the resonant frequency decrease at $T_{mxc} = 160\,\mathrm{mK}$ relative to the unloaded $L_J = 0$ case. This was due to the larger supercurrent (smaller L_J) on the electron side relative to the hole side. Increasing the flake temperature further increases L_J and decreases the resonant frequency. A rough estimate of the further decrease of the resonant frequency δf due to increased temperature is as follows:

$$\frac{|\delta f|}{|\Delta f|} \approx \frac{|\delta I_c|}{|\Delta I_c|}$$

I_c typically decreases by 20-30% as the flake temperature is increased from 160 mK to 400 mK. From Fig. 7.5, we find

Hole Side:

$$\frac{|\delta f_{hole}|}{|\Delta f_{hole}|} = \frac{26\ \text{MHz}}{110\ \text{MHz}} \approx 24\%$$

Electron Side:

$$\frac{|\delta f_{electron}|}{|\Delta f_{electron}|} = \frac{5.9\ \text{MHz}}{18.6\ \text{MHz}} \approx 32\%$$

The change in resonant frequency is therefore consistent with the typical change in $I_c(T)$. We conclude that the greater magnitude of frequency decrease on the hole side relative to the electron side follows as a straightforward result of the greater inductive loading of the transmission line resonator.

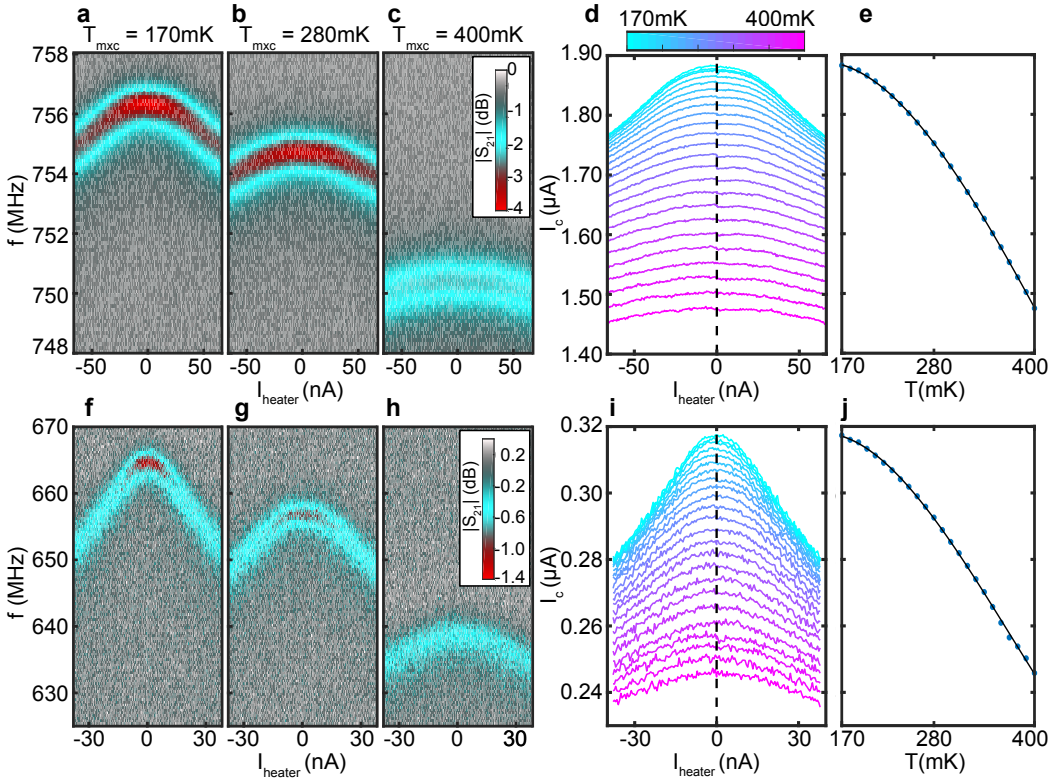

Figure 7.5: **Electron-side and Hole-side Heating and Calibration. a-c,** Electron-side ($V_{BG} = 1.1\,V$) and **f-h,** hole-side ($V_{BG} = -1.8\,V$) $|S_{21}(f)|$ vs. I_{heater} for three representative mixing stage temperatures **a, f)** $T_{mxc} = 170\,mK$ **b, g)** $T_{mxc} = 280\,mK$ **c, h)** $T_{mxc} = 400\,mK$. Applying a DC heater current I_{heater} to the designated heater port decreases the resonant frequency of the device. As expected, the shifts are symmetric with respect to the polarity of I_{heater}. **d,** Electron-side and **i,** hole-side I_c as a function of I_{heater}. Fitting **a-c** and **f-h** allows extraction of resonance parameters (f_0, Q_i) which are subsequently used to estimate the junction parameters (I_c, R_{SG}) via a numerical impedance model). I_c is plotted as a function of I_{heater} for several mixing chamber temperatures T_{mxc} (color). The dashed line at $I_{heater} = 0\,nA$ corresponds to the data cut plotted in **e** and **j**. **e,** Electron-side and **j,** hole-side calibration curve, the unheated I_c as a function of T_{mxc}. Since I_c monotonically decreases with increasing T_{mxc}, there is a one-to-one correspondence between I_c and T_{mxc}, so shifts in I_c can be transduced into shifts of graphene flake temperature.

7.5 Power/Temperature Scaling

Measurements of hBN-encapsulated graphene performed previously[32, 69] reveal that G_{th} (scaled by the area) is about three orders-of-magnitude larger than predictions by simple bulk electron-phonon coupling theory. The magnitude of $G_{th} \sim 5 - 300\, pW/K$ in our measurements is consistent with these observations. Due to enhanced mobility, hBN-encapsulated graphene is typically in the ballistic scattering limit, in which the carrier mean free path l_{mfp} is limited by the device dimension ($L_{device} \approx 5\, \mu m$ in our sample). This observation has led to the hypothesis that the enhanced G_{th} may arise from "resonant supercollisions" [64, 109] a scenario consistent with the spatially resolved measurements[48, 47]. In this scenario, defects located at edge of the graphene flake locally enhance electron-phonon interactions and open a thermalization pathway that dominates over electron-phonon coupling in the bulk. Spatially-resolved scanning SQUID measurements show an enhancement of surface phonon temperature at graphene edges and close to metal contacts. Theory formulated to explain these results[109] suggests that an $n = 5$ scaling exponent should hold down to milli-Kelvin temperatures ($T < T_{BG}$) in the limit of strong scattering ($\delta \sim 1$). In this context, our high precision measurements provide the first clear evidence that an $n = 5$ scaling exponent and thus resonant supercollisions can indeed dominate the thermalization in graphene at sub-Kelvin temperatures.

We note G_{th} exhibits a power law consistent with $n = 5$ for both electron and hole doping, indicating that this mechanism remains dominant in both regimes. Interestingly, the electron- and hole-side prefactors differ by a factor of approximately two (see 7.6c). A possible explanation for this difference arises from the energy distribution of resonant scattering centers[47]. In this scenario, different scattering centers are activated when the chemical potential of the flake is shifted by the back-gate. Therefore, it is possible that the difference in the prefactors can be attributed to different populations of activated scatterers. Additionally, we note that, in case of hole doping, the intrinsic p-n junction formed between the graphene region close to the Al contacts (which is always intrinsically n-doped) and the p-doped bulk may also play a role. In this regime, holes from the bulk must pass across the p-n junction in order to efficiently thermalize via resonant scattering centers. Since the p-n junction has a finite transmission probability, it may therefore reduce the overall thermalization rate. We note that attaining an accurate calculation of the thermalization prefactor from first principles is difficult due to effects outlined above and further theoretical work is needed for quantitive comparisons.

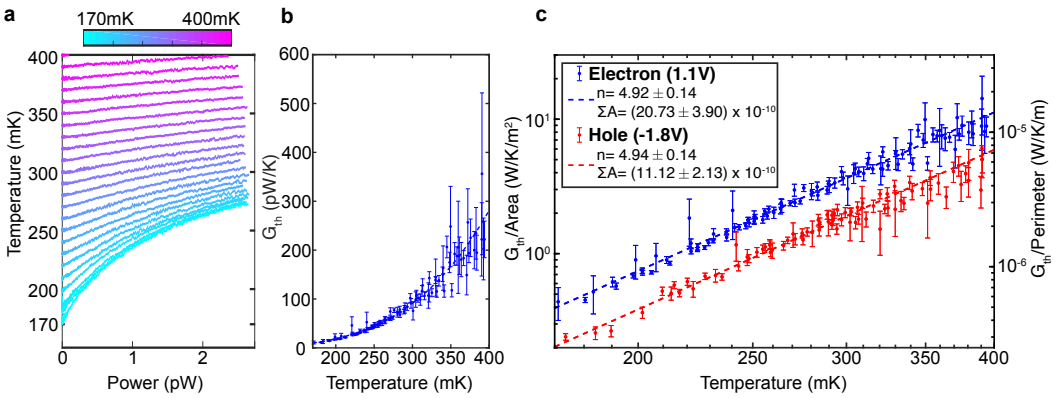

Figure 7.6: **Power-Temperature Curves.** **a,** Electron-side flake temperature as a function of heat power. From the injected DC current I_{heater} and measured voltage drop V across the heater port, the injected heater power can be determined $P_{heater} = I_{heater} \times V$. From the I_c vs. I_{heater} traces in Fig. 3d,i and the I_c vs. T_{mxc} calibration in Fig. 3e,j, flake temperature can be determined as a function of applied P_{heater}. Color corresponds to the mixing chamber stage temperature. **b,** G_{th} vs. T_{mxc}. Taking the numerical derivative $\frac{\partial P}{\partial T}$ of Fig. 4a allows the data to be plotted on a single line. Fit line is to the power law $G_{th} = \partial P/\partial T = n\Sigma A T^{n-1}$ where n is the scaling exponent and ΣA is the multiplicative factor. **c,** Electron and hole G_{th} vs. T_{mxc} (log-log scale). Hole and electron doping both show power law scaling with an $n = 5$ scaling exponent. The units of the ΣA electron-phonon coupling prefactor in the label are $\mathrm{W/K^5}$. The factor of ~ 2 difference between the electron and hole prefactors is discussed in the main text.

7.6 Conclusion

In this chapter, we have done the following:

- We have introduced the standard deformation potential approximation for electron-phonon scattering as well as expressions for electron-phonon coupling in metals and monolayer graphene.
- We have discussed experimental verification of the hot-electron effect in metals by Roukes and in monolayer graphene by Fong and Schwab.
- We have discussed our Joule heating measurements employing Josephson inductance thermometry performed on monolayer graphene, and we have discussed the origin of the measured power law-dependence between applied power and electron temperature.

In the next section, we will characterize the noise of our detector by measuring the noise equivalent power in an amplitude-modulation scheme.

Chapter 8

NOISE EQUIVALENT POWER

8.1 Introduction

To characterize the noise of our thermal detector, we measure the noise-equivalent power (NEP). In this chapter we will develop a discussion of the NEP measurement as follows

- First, we will discuss the calculation that will motivate the measurement scheme.
- Second, we will sketch the measurement setup and sketch a circuit diagram.
- Third, we will show key intermediate measurements to demonstrate that our measurement is well-behaved.
- Fourth, we will plot the measured NEP as a function of carrier frequency and applied carrier power (to be explained) in order to explore the parameter space.
- Finally, we will discuss detection limits implied by the measured NEP.

Having completed this chapter, the reader should have a strong grasp of the measurement procedure, experimental checks, and results, and should be able to repeat this method in order to characterize the NEP of any equivalent thermal detector.

8.2 Theory

A key figure-of-merit for linear power detectors is noise-equivalent power (NEP) [79, 85]. A power-to-voltage detector has a responsivity $\mathcal{R}$, such that

$$V_{out} = \mathcal{R}(P_{in})$$

In the linear-response regime, i.e. for small applied power, this expression simplifies to

$$\delta V_{out} \approx \left(\left. \frac{\partial V_{out}}{\partial P_{in}} \right|_{\delta P_{in}=0} \right) * \delta P_{in}$$

In this regime, the NEP of a power-to-voltage detector (in units of $\frac{W}{\sqrt{Hz}}$) can be defined as that power spectral density at the device input which produces the measured voltage spectral density $\sqrt{S_V}$ at the output:

$$NEP \equiv \frac{\sqrt{S_V}}{\partial V_{out}/\partial P_{heater}|_{\delta P_{heater}=0}}$$

The above expression suggests two immediate ways to measure the NEP. One is to measure the voltage spectral density $\sqrt{S_V}$ at the output and the device responsivity $\partial V_{out}/\partial P_{heater}$. Another is to measure the applied power at the input δP_{in}, and the SNR at the output as suggested by rearranging the above expression

$$NEP \equiv \frac{\sqrt{S_V}}{\delta V_{out}} * \delta P_{in} = \frac{\delta P_{in}}{SNR} = \frac{\delta P_{heater}}{4 \times SNR}$$

In the above equation, the SNR is in units of $\frac{V}{V/\sqrt{Hz}}$ and $P_{in} = P_{heater}/4$. The latter expression is true since we have implicitly assumed P_{in} is that input power which produces the measurable V_{out} signal. In our case, only one quarter of the heat power P_{heater} injected at the heater port produces the measured sideband signal.

8.3 Experimental Design

To measure the NEP, we use the measurement setup in Fig. 8.3a,b and perform the following procedure:

- We apply a carrier tone on the microwave line (Fig. 8.3a, first panel). The S_{21} parameter is the transfer function which determines the magnitude and phase of the signal at the output. Thus, a carrier tone at the resonant frequency, i.e. at the maximal dip of the S_{21} parameter, will have a smaller transmitted magnitude than a carrier tone placed off-resonance.

- Measurement of $P_{heater}(\omega) = I_{heater}(\omega) \times V_{heater}(\omega)$ is achieved by sourcing a current $I_{heater}(\omega)$ to the heater port and measuring the voltage drop $V_{heater}(\omega) = I_{heater}(\omega)R_{heater}$ over the heater port in a 4-wire lock-in measurement. Since we apply an AC heater current $I_{heater}(\omega) \propto \cos \omega t$, it follows that $P_{heater}(\omega) \propto \cos^2 \omega t = \frac{1}{2}(1 + \cos(2\omega t))$. Only the 2ω term in the final expression contributes to the V_{out} sideband signal.

- Applying an AC heat power P_{heater} to the heater port modulates the S_{21} parameter between unheated and heated states (Fig. 8.3a, second panel).

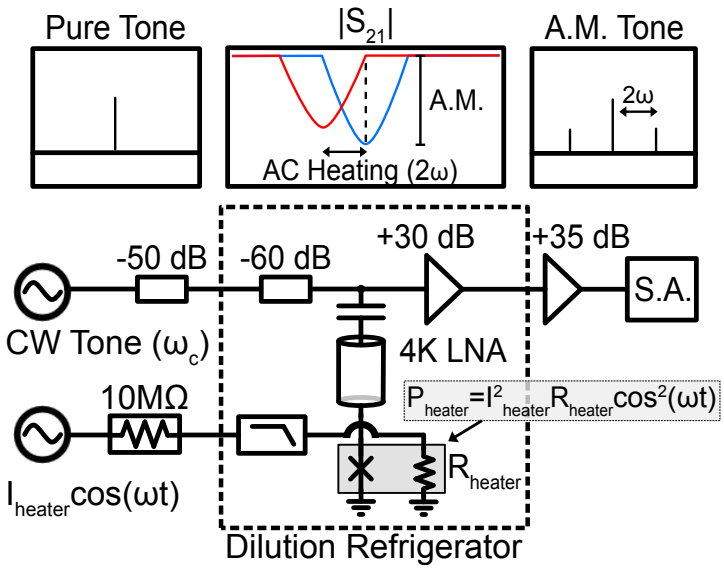

Figure 8.1: **Schematic of Measurement Chain** First panel shows a pure carrier tone sent down the microwave line. Second panel shows that an applied ω heater current and subsequent 2ω modulation of the heat power and temperature of the graphene flake yields a 2ω modulation of the transmission function (S_{21} parameter) between unheated (blue) and heated (red) states. The pure tone (dashed line) is placed within the bandwidth of the transmission function, such that it will be amplitude modulated at 2ω with a modulation index that depends on the magnitude of the S_{21} dip. Third panel shows the amplitude-modulated signal with sidebands at 2ω as readout on the spectrum analyzer. The measured signal-to-noise ratio of the sideband is used to determine the NEP. **b,** Circuit Diagram. A continuous-wave carrier tone at ω_c is sent down a microwave line to the graphene device, amplified, and read out by a spectrum analyzer. An AC heater current at frequency $\omega = 2\pi \times 337$ Hz injects a 2ω heat power P_{heater} in the graphene flake and produces 2ω amplitude modulation of the carrier tone, as discussed in **a**.

Consistent with the heating measurements performed in the main text, the heated state has a lower resonant frequency and lower quality factor than the unheated state. The 2ω component of the input power P_{heater} modulates the flake temperature at 2ω. Thus, modulation of the S_{21} resonance feature will occur at 2ω.

- Placing the frequency of the carrier tone within the bandwidth of the modulated S_{21} resonance feature will amplitude modulate the carrier, producing sidebands spaced at 2ω from the carrier (Fig. 8.3a, second and third panel). Provided that the device is in the linear-response regime, the voltage of the sidebands will increase in proportion to applied heat power, i.e. $V_{sb} \propto P_{heater}$.

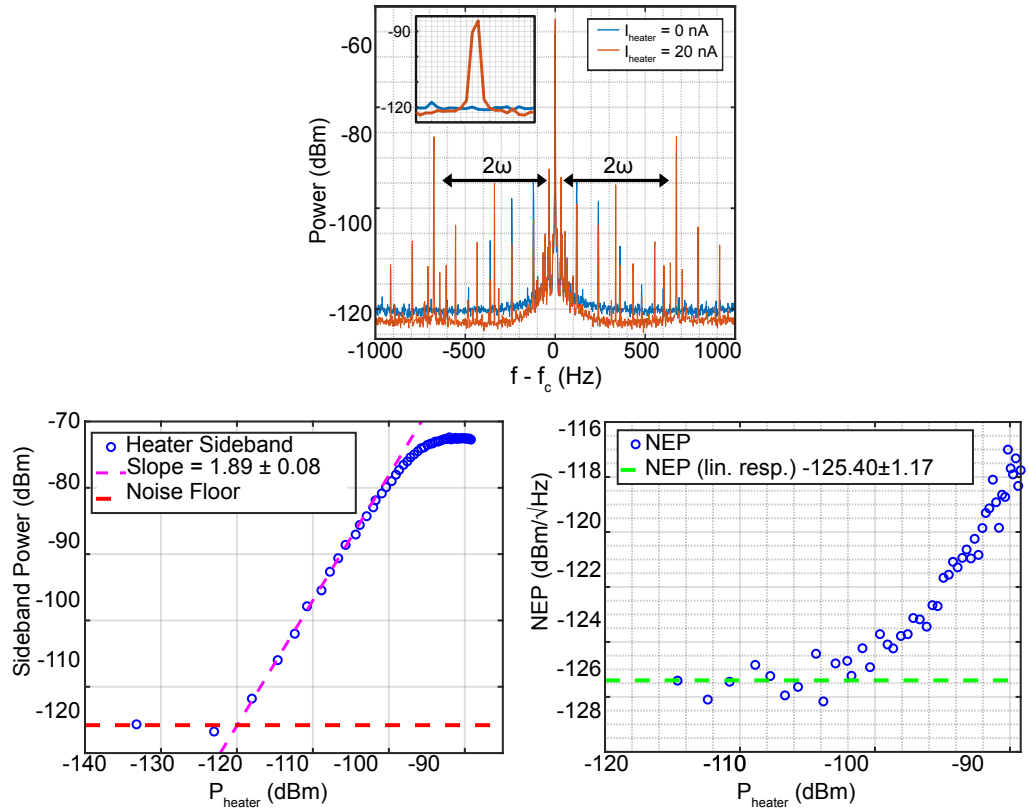

Figure 8.2: **NEP Measurement Procedure. Left Panel,** Representative spectrum at output of measurement chain. Spectrum as read out by spectrum analyzer (RBW = 1 Hz) for applied heat power off (blue) and on (red). The primary effect of the applied heat is to produce sidebands spaced at 2ω from the the carrier tone. Other peaks in the spectrum exist at multiples of the line frequency. A peak at ω is consistent with a DC offset in the applied heat power. Inset shows the 2ω sideband. **Center Panel,** Sideband Power vs. P_{heater}. In the low-P_{heater} linear-response regime, the sideband voltage $V_{sb} \propto P_{heater}$. Since the spectrum analyzer reads out the sideband power, $P_{sb} \propto P_{heater}^2$, which is consistent with the slope at low P_{heater}. **Right Panel,** NEP vs. P_{heater}. The linear-response regime is characterized by a regime of constant NEP, before rising as the amplitude modulation saturates to its maximal value. The NEP plotted in **g,f** corresponds to the linear response regime (green dashed line).

It follows that the power of the sidebands will increase as $P_{sb} \propto P_{heater}^2$.

- The amplitude-modulated carrier is read out by a spectrum analyzer (Fig. 8.3a, third panel). The signal-to-noise ratio of the sideband is used to calculate the NEP. We note that only one sideband is used in the NEP measurement.

8.4 Sideband Spectrum

In Fig. 8.3c, we see that application of an AC heater current of magnitude I_{heater} = 20 nA results in sidebands at 2ω offset from the carrier, where $\omega = 2\pi \times 337$ Hz. In addition to the 2ω sidebands, sidebands at multiples of the 60 Hz line frequency frequency are present. Additionally, there are sidebands at ω approximately 10 dB down from the 2ω sidebands. This can be explained by a small DC offset in the heater current.

With increasing heater power, the magnitude of the sidebands saturates at a value consistent with expectations. It is straightforward to show that a resonance dip of 3 dB generates a maximum amplitude modulation index $m = 17\%$, which should produce sidebands 21 dB lower than the carrier. This is in agreement with the measured sideband magnitude that is 23 dB lower than the carrier.

8.5 Sideband Scaling

In the linear response regime, $V_{sb} \propto \delta P_{heater}$. Therefore, the sideband signal as measured on the spectrum analyzer (in power units) should scale as $P_{sb} \propto P_{heater}^2$, or by 20 dB/decade. This is seen in Fig. 8.3d for applied heat P_{heater} in the range -120 dBm to -105 dBm, where the slope of fit at low-P_{heater} is consistent with a scaling exponent $n = 2$. This confirms that our measurement is in linear-response regime at low P_{heater}. For greater applied P_{heater}, the sideband power saturates as the amplitude modulation reaches the full maximum of the resonance dip.

8.6 NEP vs. P_{heater}

In the linear response regime, the NEP is constant with respect to P_{heater} since $V_{sb} \propto P_{heater}$. This is shown Fig. 8.3e for $P_{heater} < -105$ dBm. As stated above, the NEP rises for $P_{heater} > -105$ dBm as the SNR saturates while P_{heater} continues to increase.

8.7 NEP vs. Carrier Frequency and Carrier Power

To explore the NEP as a function of the carrier tone, we generate a heat map with swept carrier frequency f_c and carrier power P_c (Fig. 8.3f,g). For the lowest carrier powers, the NEP is minimized for carrier frequencies close to the resonance minimum, where the responsivity of the resonance to applied heater power is greatest and therefore the amplitude modulation of the carrier is greatest. As the carrier power P_c is increased, the junction is driven to nonlinearity, resulting in a resonance dip with a steep falling edge and a shallow rising edge. This has the effect of

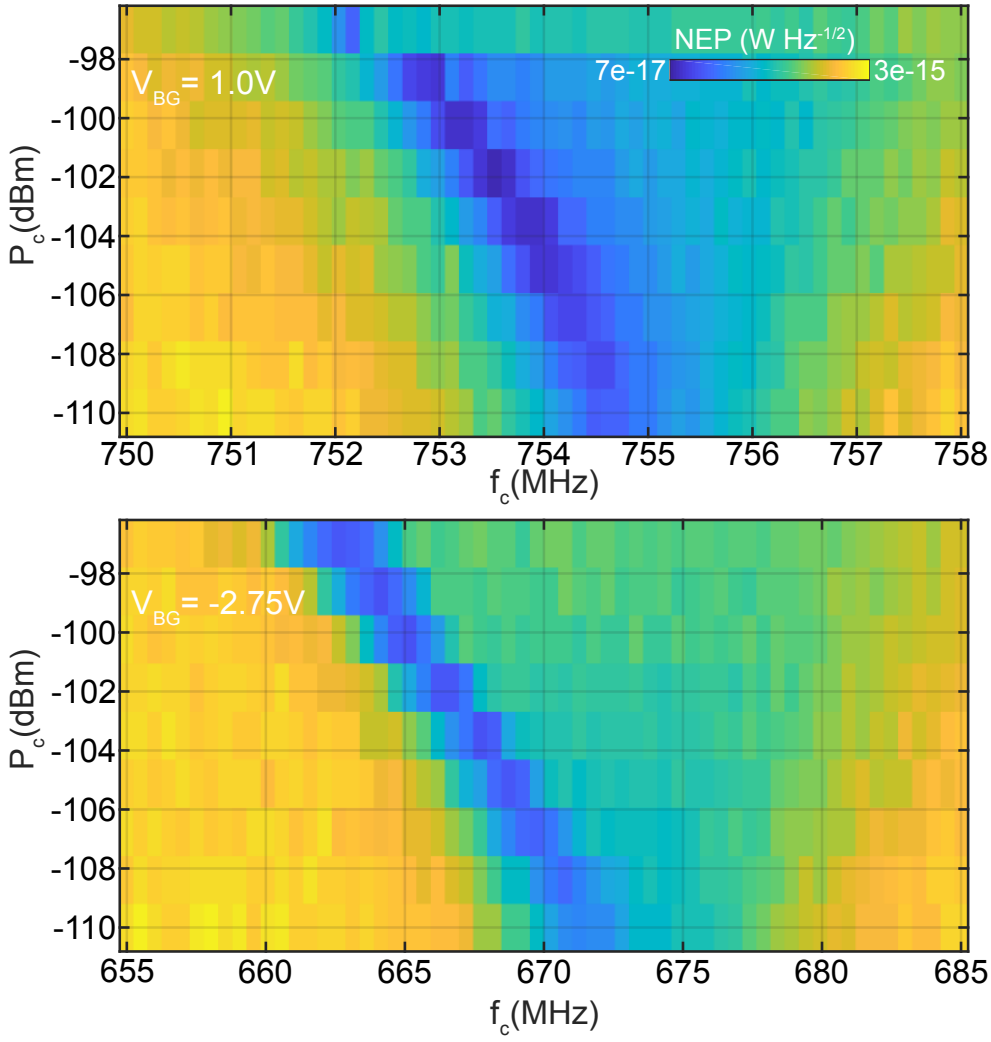

Figure 8.3: **Noise Equivalent Power (NEP) Measurement. e,** NEP vs. P_{heater}. The linear-response regime is characterized by a regime of constant NEP, before rising as the amplitude modulation saturates to its maximal value. The NEP plotted in **g,f** corresponds to the linear response regime (green dashed line). **f, g,** NEP vs. carrier power P_c and carrier frequency f_c for **f)** electron-side ($V_{BG} = 1.0\,\mathrm{V}$) and **g)** hole-side ($V_{BG} = -2.75\,\mathrm{V}$). Minimal NEP occurs near the resonance dip minimum where amplitude modulation is largest. As carrier power P_c is increased, the resonance dip downshifts to lower frequencies and is driven into nonlinearity, as characterized by an asymmetric resonance lineshape with steep falling edge and shallow rising edge. The minimum NEP tracks the steep falling edge where amplitude modulation is greatest.

enhancing the NEP on the falling edge and reducing it on the rising edge. For carrier powers $P_c > -98$ dBm, the quality factor of the resonance feature is degraded to such an extent that the amplitude modulation of sideband is reduced and the NEP increases. The NEP reaches a minimum value of $7 \times 10^{-17}\,\mathrm{W}/\sqrt{\mathrm{Hz}}$ for a carrier power $P_{carrier} = -102$ dBm and carrier frequency $f_{carrier} = 753.5$ MHz.

8.8 Detection Limits

The measured minimum noise-equivalent power $NEP_{min} \approx 7 \times 10^{-17}\,\mathrm{W}/\sqrt{\mathrm{Hz}}$. It is limited by the noise of the 4K cryoamp and is $\sim 20\times$ larger than the thermal fluctuation-limited $NEP = \sqrt{4k_B T^2 G_{th}}$ at $T_{mxc} = 200\,\mathrm{mK}$. At $T_{mxc} = 58\,\mathrm{mK}$, the projected thermal fluctuation-limited $NEP_{proj} \approx 1 \times 10^{-19}\,\mathrm{W}/\sqrt{Hz}$, assuming that the T^4 dependence of G_{th} holds down to these temperatures [79, 85]. The corresponding thermal fluctuation-limited energy resolution $\delta E = NEP_{proj}\sqrt{\tau_{th}} \approx h \times 65\,\mathrm{GHz}$, assuming the projected thermal time constant $\tau_{th} = \frac{C_{th}}{G_{th}} \approx 170\,\mathrm{ns}$, $n_{carrier} = \frac{10^{12}}{cm^2}$, $A = 25\,\mu m^2$.

8.9 Conclusion

In this chapter, we have done the following:

- We have motivated the amplitude-modulation scheme of the NEP measurement and related it to physical measurables of our setup.
- We have shown intermediate measurements to demonstrate close agreement of each step of the measurement with predictions.
- We have explored the measured NEP as a function of carrier frequency and applied carrier power.
- We have discussed the detection limits implied by the measured NEP.

This completes the characterization measurements of our device.

Chapter 9

SUMMARY

In this thesis, we have presented a method of thermometry convenient for integration with low-heat capacity Van-der-Waals materials. In this method, increases of the graphene flake temperature manifest as decreases of the temperature-dependent supercurrent of an SNS-type Josephson element. In turn, this produces dispersive shifts of the resonant frequency of a superconducting resonator, which can be monitored with standard microwave reflectometry. This technique is amenable to frequency-domain multiplexed readout of detector arrays akin to the readout mechanism of microwave kinetic inductance detectors (MKID) arrays [28]; to operation at dilution refrigerator temperatures where graphene thermal properties yield greatest detector sensitivities; and to enhanced measurement bandwidths for tracking single-shot photon arrivals.

We have discussed the relevant details for a researcher interested in pushing the limits of single-shot thermal detectors, beginning with a thorough discussion of the relevant physical models and fundamental limits of a thermal detector and continuing with key superconducting phenomena exploited in this device scheme.

Subsequently, we discussed fabrication details, device architecture, and cryogenic measurement setup for application of Joule heat and microwave readout of the device. Using this setup, we have characterized the physical properties of this device with sweeps of carrier density and Joule heat. The former revealed the ballistic nature of charge carriers in this device, while the latter revealed an unexpected $P \propto T^5$ dependence for which we have discussed possible explanations. Finally, we measured the noise of our detector to be at the level of $NEP_{min} \approx 7 \times 10^{-17}$ W/$\sqrt{\text{Hz}}$ using a amplitude-modulation scheme amenable to measuring the noise-equivalent power of resonantly-coupled linear detectors.

If the benefits of this readout scheme can be combined with reliable fabrication of low-G_{th} and low-C_{th} Van-der-Waals materials, resonantly-coupled Van-der-Waals heterostructures will remain an exciting research avenue for pushing the limits of calorimetric detection.

BIBLIOGRAPHY

[1] AF Andreev. “The thermal conductivity of the intermediate state in superconductors”. In: 46.5 (1964), pp. 1823–1828.

[2] James F Annett. “Superconductivity, superfluids, and condensates /”. In: (2004), xi, 186 p. : URL: http://caltech.tind.io/record/667497.

[3] Makoto R Arai. “A fundamental noise limit for biased resistors at low temperatures”. In: *Applied physics letters* 42.10 (1983), pp. 906–908.

[4] Harpreet Singh Arora. “Superconductivity in Graphene Hetero-Structures: From Fundamental Physics to Functional Devices”. en. PhD thesis. 2020. DOI: 10.7907/NC05-GR15. URL: https://resolver.caltech.edu/CaltechTHESIS:06052020-175219708.

[5] Harpreet Singh Arora et al. “Superconductivity in metallic twisted bilayer graphene stabilized by WSe 2”. In: *Nature* 583.7816 (2020), pp. 379–384.

[6] Neil W Ashcroft and N. David Mermin. “Solid state physics /”. In: (1976), xxi, 826 p. : URL: http://caltech.tind.io/record/461846.

[7] E. Baracchini et al. “PTOLEMY: A Proposal for Thermal Relic Detection of Massive Neutrinos and Directional Detection of MeV Dark Matter”. In: *arXiv:1808.01892 [astro-ph, physics:hep-ex, physics:physics]* (Aug. 2018). arXiv: 1808.01892 [astro-ph, physics:hep-ex, physics:physics].

[8] John Bardeen, Leon N Cooper, and John Robert Schrieffer. “Theory of superconductivity”. In: *Physical review* 108.5 (1957), p. 1175.

[9] Carlo Beenakker and Henk van Houten. “Superconducting Quantum Point Contacts and Other Mesoscopic Josephson Junctions”. In: *Science and Technology of Mesoscopic Structures*. Springer, 1992, pp. 232–234.

[10] Charles H Bennett. “Logical reversibility of computation”. In: *IBM journal of Research and Development* 17.6 (1973), pp. 525–532.

[11] Charles H Bennett. “Notes on Landauer’s principle, reversible computation, and Maxwell’s Demon”. In: *Studies In History and Philosophy of Science Part B: Studies In History and Philosophy of Modern Physics* 34.3 (2003), pp. 501–510.

[12] Antoine Bérut, Artyom Petrosyan, and Sergio Ciliberto. “Information and thermodynamics: experimental verification of Landauer’s Erasure principle”. In: *Journal of Statistical Mechanics: Theory and Experiment* 2015.6 (2015), P06015.

[13] Antoine Bérut et al. “Experimental verification of Landauer’s principle linking information and thermodynamics”. In: *Nature* 483.7388 (2012), pp. 187–189.

[14] K Bladh et al. “Comparison of cryogenic filters for use in single electronics experiments”. In: *Review of Scientific Instruments* 74.3 (2003), pp. 1323–1327.

[15] GE Blonder, m M Tinkham, and k TM Klapwijk. “Transition from metallic to tunneling regimes in superconducting microconstrictions: Excess current, charge imbalance, and supercurrent conversion”. In: *Physical Review B* 25.7 (1982), p. 4515.

[16] I. V. Borzenets et al. “Ballistic Graphene Josephson Junctions from the Short to the Long Junction Regimes”. In: *Physical Review Letters* 117.23 (Dec. 2016), p. 237002. DOI: 10.1103/PhysRevLett.117.237002.

[17] I. V. Borzenets et al. “Phonon Bottleneck in Graphene-Based Josephson Junctions at Millikelvin Temperatures”. In: *Physical Review Letters* 111.2 (July 2013), p. 027001. DOI: 10.1103/PhysRevLett.111.027001.

[18] Alexander B Boyd and James P Crutchfield. “Maxwell demon dynamics: Deterministic chaos, the Szilard map, and the intelligence of thermodynamic systems”. In: *Physical review letters* 116.19 (2016), p. 190601.

[19] Alexander B Boyd, Dibyendu Mandal, and James P Crutchfield. “Identifying functional thermodynamics in autonomous Maxwellian ratchets”. In: *New Journal of Physics* 18.2 (2016), p. 023049.

[20] Alexander B Boyd et al. “Shortcuts to thermodynamic computing: The cost of fast and faithful erasure”. In: *arXiv preprint arXiv:1812.11241* (2018).

[21] Leon Brillouin. “Maxwell’s demon cannot operate: Information and entropy. I”. In: *Journal of Applied Physics* 22.3 (1951), pp. 334–337.

[22] V. E. Calado et al. “Ballistic Josephson Junctions in Edge-Contacted Graphene”. en. In: *Nature Nanotechnology* 10.9 (Sept. 2015), pp. 761–764. ISSN: 1748-3395. DOI: 10.1038/nnano.2015.156.

[23] Herbert B Callen and Theodore A Welton. “Irreversibility and generalized noise”. In: *Physical Review* 83.1 (1951), p. 34.

[24] LC Campos et al. “Quantum and classical confinement of resonant states in a trilayer graphene Fabry-Pérot interferometer”. In: *Nature communications* 3.1 (2012), pp. 1–6.

[25] Wei Chen and Aashish A. Clerk. “Electron-Phonon Mediated Heat Flow in Disordered Graphene”. In: *Physical Review B* 86.12 (Sept. 2012), p. 125443. DOI: 10.1103/PhysRevB.86.125443.

[26] TCP Chui et al. “Temperature fluctuations in the canonical ensemble”. In: *Physical review letters* 69.21 (1992), p. 3005.

[27] Gavin E Crooks. “Entropy production fluctuation theorem and the nonequilibrium work relation for free energy differences”. In: *Physical Review E* 60.3 (1999), p. 2721.

[28] Peter K. Day et al. “A Broadband Superconducting Detector Suitable for Use in Large Arrays”. en. In: *Nature* 425.6960 (Oct. 2003), pp. 817–821. ISSN: 1476-4687. DOI: 10.1038/nature02037.

[29] Peter K Day et al. “Wideband paramps for the millimeter and submillimeter bands”. In: *2014 39th International Conference on Infrared, Millimeter, and Terahertz waves (IRMMW-THz)*. IEEE. 2014, pp. 1–2.

[30] Peter Day et al. “The fluctuation-imposed limit for temperature measurement”. In: *Journal of low temperature physics* 107.3 (1997), pp. 359–370.

[31] Robert Henry Dicke. “The measurement of thermal radiation at microwave frequencies”. In: *Classics in Radio Astronomy*. Springer, 1946, pp. 106–113.

[32] Anne W. Draelos et al. “Supercurrent Flow in Multiterminal Graphene Josephson Junctions”. In: *Nano Letters* 19.2 (Feb. 2019), pp. 1039–1043. ISSN: 1530-6984. DOI: 10.1021/acs.nanolett.8b04330.

[33] Xu Du, Ivan Skachko, and Eva Y Andrei. “Josephson current and multiple Andreev reflections in graphene SNS junctions”. In: *Physical Review B* 77.18 (2008), p. 184507.

[34] Xu Du et al. “Graphene-based bolometers”. In: *arXiv preprint arXiv:1308.4065* (2013).

[35] P Dubos et al. “Josephson critical current in a long mesoscopic SNS junction”. In: *Physical Review B* 63.6 (2001), p. 064502.

[36] Dmitri K. Efetov et al. “Fast Thermal Relaxation in Cavity-Coupled Graphene Bolometers with a Johnson Noise Read-Out”. en. In: *Nature Nanotechnology* 13.9 (Sept. 2018), pp. 797–801. ISSN: 1748-3395. DOI: 10.1038/s41565-018-0169-0.

[37] CD English et al. “Observation of nonsinusoidal current-phase relation in graphene Josephson junctions”. In: *Physical Review B* 94.11 (2016), p. 115435.

[38] Byeong Ho Eom et al. “A wideband, low-noise superconducting amplifier with high dynamic range”. In: *Nature Physics* 8.8 (2012), pp. 623–627.

[39] Kin Chung Fong and K. C. Schwab. “Ultrasensitive and Wide-Bandwidth Thermal Measurements of Graphene at Low Temperatures”. In: *Physical Review X* 2.3 (July 2012), p. 031006. DOI: 10.1103/PhysRevX.2.031006.

[40] Kin Chung Fong et al. “Measurement of the Electronic Thermal Conductance Channels and Heat Capacity of Graphene at Low Temperature”. In: *Physical Review X* 3.4 (Oct. 2013), p. 041008. DOI: 10.1103/PhysRevX.3.041008.

[41] VF Gantmakher. “The experimental study of electron-phonon scattering in metals”. In: *Reports on Progress in Physics* 37.3 (1974), p. 317.

[42] Jiansong Gao. *The physics of superconducting microwave resonators*. California Institute of Technology, 2008.

[43] K. Geerlings et al. "Improving the Quality Factor of Microwave Compact Resonators by Optimizing Their Geometrical Parameters". In: *Applied Physics Letters* 100.19 (May 2012), p. 192601. ISSN: 0003-6951. DOI: 10.1063/1.4710520.

[44] Pierre-Gilles de Gennes. "Superconductivity of metals and alloys". In: (). Lecture notes from a course given in the Faculté des sciences, Orsay, France, 1962-63, xiv, 274p. URL: http://caltech.tind.io/record/481460.

[45] G. Giovannetti et al. "Doping Graphene with Metal Contacts". In: *Phys. Rev. Lett.* 101 (2 July 2008), p. 026803. DOI: 10.1103/PhysRevLett.101.026803. URL: https://link.aps.org/doi/10.1103/PhysRevLett.101.026803.

[46] Alexandre Avraamovitch Golubov, M Yu Kupriyanov, and E Il'Ichev. "The current-phase relation in Josephson junctions". In: *Reviews of modern physics* 76.2 (2004), p. 411.

[47] Dorri Halbertal et al. "Imaging Resonant Dissipation from Individual Atomic Defects in Graphene". en. In: *Science* 358.6368 (Dec. 2017), pp. 1303–1306. ISSN: 0036-8075, 1095-9203. DOI: 10.1126/science.aan0877.

[48] D. Halbertal et al. "Nanoscale Thermal Imaging of Dissipation in Quantum Systems". en. In: *Nature* 539.7629 (Nov. 2016), pp. 407–410. ISSN: 1476-4687. DOI: 10.1038/nature19843.

[49] Tero T Heikkilä. *The physics of nanoelectronics: transport and fluctuation phenomena at low temperatures*. Vol. 21. Oxford University Press, 2013.

[50] Yonit Hochberg et al. "Directional Detection of Dark Matter with Two-Dimensional Targets". en. In: *Physics Letters B* 772 (Sept. 2017), pp. 239–246. ISSN: 0370-2693. DOI: 10.1016/j.physletb.2017.06.051.

[51] Jeongmin Hong et al. "Experimental test of Landauer's principle in single-bit operations on nanomagnetic memory bits". In: *Science advances* 2.3 (2016), e1501492.

[52] Dongchan Jeong et al. "Observation of supercurrent in PbIn-graphene-PbIn Josephson junction". In: *Physical Review B* 83.9 (2011), p. 094503.

[53] J. B. Johnson. "Thermal Agitation of Electricity in Conductors". In: *Phys. Rev.* 32 (1 July 1928), pp. 97–109. DOI: 10.1103/PhysRev.32.97. URL: https://link.aps.org/doi/10.1103/PhysRev.32.97.

[54] Yonggun Jun, Momčilo Gavrilov, and John Bechhoefer. "High-precision test of Landauer's principle in a feedback trap". In: *Physical review letters* 113.19 (2014), p. 190601.

[55] Chung Ting Ke et al. “Critical current scaling in long diffusive graphene-based Josephson junctions”. In: *Nano letters* 16.8 (2016), pp. 4788–4791.

[56] M Ketchen. “DC SQUIDs 1980: The state of the art”. In: *IEEE Transactions on Magnetics* 17.1 (1981), pp. 387–394.

[57] MB Ketchen and JM Jaycox. “Ultra-low-noise tunnel junction dc SQUID with a tightly coupled planar input coil”. In: *Applied Physics Letters* 40.8 (1982), pp. 736–738.

[58] Doojin Kim et al. “Detecting keV-Range Super-Light Dark Matter Using Graphene Josephson Junction”. In: *arXiv:2002.07821 [cond-mat, physics:hep-ex, physics:hep-ph]* (Sept. 2020). arXiv: 2002.07821 [cond-mat, physics:hep-ex, physics:hep-ph].

[59] Minsoo Kim et al. “Strong proximity Josephson coupling in vertically stacked NbSe2–graphene–NbSe2 van der Waals junctions”. In: *Nano letters* 17.10 (2017), pp. 6125–6130.

[60] Charles Kittel. “Introduction to solid state physics /”. In: (1996), xi, 673 p. : URL: http://caltech.tind.io/record/608960.

[61] Charles Kittel and Herbert Kroemer. *Thermal physics*. 1998.

[62] Jan Klaers et al. “Squeezed thermal reservoirs as a resource for a nanomechanical engine beyond the carnot limit”. In: *Physical Review X* 7.3 (2017), p. 031044.

[63] R. Kokkoniemi et al. “Bolometer Operating at the Threshold for Circuit Quantum Electrodynamics”. en. In: *Nature* 586.7827 (Oct. 2020), pp. 47–51. ISSN: 1476-4687. DOI: 10.1038/s41586-020-2753-3.

[64] Jian Feng Kong et al. “Resonant Electron-Lattice Cooling in Graphene”. In: *Physical Review B* 97.24 (June 2018), p. 245416. DOI: 10.1103/PhysRevB.97.245416.

[65] Sebastian Krinner et al. “Engineering cryogenic setups for 100-qubit scale superconducting circuit systems”. In: *EPJ Quantum Technology* 6.1 (2019), p. 2.

[66] Piranavan Kumaravadivel and Xu Du. “Signatures of evanescent transport in ballistic suspended graphene-superconductor junctions”. In: *Scientific reports* 6.1 (2016), pp. 1–8.

[67] L. D. Landau, E. M. Lifshits, and L. P. Pitaevskiĭ. “Statistical physics /”. In: (). Pt.2 is a reprinted with corrections 1999, 2 v. : URL: http://caltech.tind.io/record/615094.

[68] Rolf Landauer. “Irreversibility and heat generation in the computing process”. In: *IBM journal of research and development* 5.3 (1961), pp. 183–191.

[69] Gil-Ho Lee et al. “Graphene-Based Josephson Junction Microwave Bolometer”. en. In: *Nature* 586.7827 (Oct. 2020), pp. 42–46. ISSN: 1476-4687. DOI: 10.1038/s41586-020-2752-4.

[70] Gil-Ho Lee et al. “Ultimately Short Ballistic Vertical Graphene Josephson Junctions”. en. In: *Nature Communications* 6.1 (Jan. 2015), p. 6181. ISSN: 2041-1723. DOI: 10.1038/ncomms7181.

[71] Chuan Li et al. “Full range of proximity effect probed with superconductor/graphene/superconductor junctions”. In: *Physical Review B* 94.11 (2016), p. 115405.

[72] *Lock-In Amplifier Basics*. Tech. rep. Stanford Research Systems, 2020.

[73] Miquel Lopez-Suarez, Igor Neri, and Luca Gammaitoni. “Sub-k BT microelectromechanical irreversible logic gate”. In: *Nature communications* 7.1 (2016), pp. 1–6.

[74] A Lukashenko and AV Ustinov. “Improved powder filters for qubit measurements”. In: *Review of Scientific Instruments* 79.1 (2008), p. 014701.

[75] David M. Pozar. *Microwave Engineering, 4th Edition | Wiley*. en-us. https://www.wiley.com/en-us/Microwave+Engineering%2C+4th+Edition-p-9780470631553.

[76] C. Macklin et al. “A near-quantum-limited Josephson traveling-wave parametric amplifier”. In: *Science* 350.6258 (Oct. 2015), pp. 307–310. DOI: 10.1126/science.aaa8525.

[77] John M Martinis, Michel H Devoret, and John Clarke. “Experimental tests for the quantum behavior of a macroscopic degree of freedom: The phase difference across a Josephson junction”. In: *Physical Review B* 35.10 (1987), p. 4682.

[78] John M Martinis and Kevin Osborne. “Superconducting qubits and the physics of Josephson junctions”. In: *arXiv preprint cond-mat/0402415* (2004).

[79] John C. Mather. “Bolometer Noise: Nonequilibrium Theory”. EN. In: *Applied Optics* 21.6 (Mar. 1982), pp. 1125–1129. ISSN: 2155-3165. DOI: 10.1364/AO.21.001125.

[80] PD Mauskopf. “Transition edge sensors and kinetic inductance detectors in astronomical instruments”. In: *Publications of the Astronomical Society of the Pacific* 130.990 (2018), p. 082001.

[81] Ben T. McAllister et al. “The ORGAN Experiment: An Axion Haloscope above 15 GHz”. en. In: *Physics of the Dark Universe* 18 (Dec. 2017), pp. 67–72. ISSN: 2212-6864. DOI: 10.1016/j.dark.2017.09.010.

[82] Dan McCammon. “Thermal equilibrium calorimeters–an introduction”. In: *Cryogenic particle detection* (2005), pp. 1–34.

[83] Naomi Mizuno, Bent Nielsen, and Xu Du. "Ballistic-like supercurrent in suspended graphene Josephson weak links". In: *Nature communications* 4.1 (2013), pp. 1–6.

[84] DC Moore et al. "Position and energy-resolved particle detection using phonon-mediated microwave kinetic inductance detectors". In: *Applied Physics Letters* 100.23 (2012), p. 232601.

[85] S. H. Moseley, J. C. Mather, and D. McCammon. "Thermal Detectors as X-ray Spectrometers". In: *Journal of Applied Physics* 56.5 (Sept. 1984), pp. 1257–1262. ISSN: 0021-8979. DOI: 10.1063/1.334129.

[86] Chandra M Natarajan, Michael G Tanner, and Robert H Hadfield. "Superconducting nanowire single-photon detectors: physics and applications". In: *Superconductor science and technology* 25.6 (2012), p. 063001.

[87] John D Norton. "The worst thought experiment". In: *The Routledge companion to thought experiments*. Routledge, 2017, pp. 454–468.

[88] John D Norton. "Waiting for landauer". In: *Studies in History and Philosophy of Science Part B: Studies in History and Philosophy of Modern Physics* 42.3 (2011), pp. 184–198.

[89] H. Nyquist. "Thermal Agitation of Electric Charge in Conductors". In: *Phys. Rev.* 32 (1 July 1928), pp. 110–113. DOI: 10.1103/PhysRev.32.110. URL: https://link.aps.org/doi/10.1103/PhysRev.32.110.

[90] Jinho Park et al. "Short ballistic Josephson coupling in planar graphene junctions with inhomogeneous carrier doping". In: *Physical review letters* 120.7 (2018), p. 077701.

[91] Jukka P Pekola. "Towards quantum thermodynamics in electronic circuits". In: *Nature Physics* 11.2 (2015), pp. 118–123.

[92] Frank Pobell. *Matter and methods at low temperatures*. Vol. 2. Springer, 2007.

[93] Gerald L Pollack. "Kapitza resistance". In: *Reviews of Modern Physics* 41.1 (1969), p. 48.

[94] Peter Rickhaus et al. "Ballistic interferences in suspended graphene". In: *Nature communications* 4.1 (2013), pp. 1–6.

[95] A Rogalski. "Graphene-based materials in the infrared and terahertz detector families: a tutorial". In: *Advances in Optics and Photonics* 11.2 (2019), pp. 314–379.

[96] M. L. Roukes. "Yoctocalorimetry: Phonon Counting in Nanostructures". en. In: *Physica B: Condensed Matter* 263-264 (Mar. 1999), pp. 1–15. ISSN: 0921-4526. DOI: 10.1016/S0921-4526(98)01482-3.

[97] M. L. Roukes et al. “Hot Electrons and Energy Transport in Metals at Millikelvin Temperatures”. In: *Physical Review Letters* 55.4 (July 1985), pp. 422–425. DOI: 10.1103/PhysRevLett.55.422.

[98] Olli-Pentti Saira et al. “Modification of electron-phonon coupling by micromachining and suspension”. In: *Journal of Applied Physics* 127.2 (2020), p. 024307.

[99] Olli-Pentti Saira et al. “Nonequilibrium thermodynamics of erasure with superconducting flux logic”. In: *Phys. Rev. Research* 2 (1 Mar. 2020). [*R.M.K. assisted in measurement and physical characterization.*], p. 013249. URL: https://link.aps.org/doi/10.1103/PhysRevResearch.2.013249.

[100] JA Sauls. *Andreev bound states and their signatures*. 2018.

[101] Felix E. Schmidt et al. “A Ballistic Graphene Superconducting Microwave Circuit”. en. In: *Nature Communications* 9.1 (Oct. 2018), p. 4069. ISSN: 2041-1723. DOI: 10.1038/s41467-018-06595-2.

[102] Keith Schwab et al. “Measurement of the quantum of thermal conductance”. In: *Nature* 404.6781 (2000), pp. 974–977.

[103] M Ben Shalom et al. “Quantum oscillations of the critical current and high-field superconducting proximity in ballistic graphene”. In: *Nature Physics* 12.4 (2016), pp. 318–322.

[104] Ramamurti Shankar. *Principles of quantum mechanics*. Springer Science & Business Media, 2012.

[105] Claude Elwood Shannon. “A mathematical theory of communication”. In: *The Bell system technical journal* 27.3 (1948), pp. 379–423.

[106] S. Shu et al. “Nonlinearity and wide-band parametric amplification in a (Nb,Ti)N microstrip transmission line”. In: *Phys. Rev. Research* 3 (2 June 2021), p. 023184. DOI: 10.1103/PhysRevResearch.3.023184. URL: https://link.aps.org/doi/10.1103/PhysRevResearch.3.023184.

[107] Leo Szilard. “On the decrease of entropy in a thermodynamic system by the intervention of intelligent beings”. In: *Behavioral Science* 9.4 (1964), pp. 301–310.

[108] Yositake Takane and Ken-Ichiro Imura. “Quasiclassical theory of the Josephson effect in ballistic graphene junctions”. In: *Journal of the Physical Society of Japan* 81.9 (2012), p. 094707.

[109] K. S. Tikhonov et al. “Resonant Supercollisions and Electron-Phonon Heat Transfer in Graphene”. In: *Physical Review B* 97.8 (Feb. 2018), p. 085415. DOI: 10.1103/PhysRevB.97.085415.

[110] Michael Tinkham. *Introduction to Superconductivity*. en. Publisher: Dover Publications, 2004. ISBN: 978-0-486-43503-9.

[111] M Titov and Carlo WJ Beenakker. "Josephson effect in ballistic graphene". In: *Physical Review B* 74.4 (2006), p. 041401.

[112] Theodore Van Duzer and Charles W Turner. *Principles of Superconductive Devices and Circuits*. Pearson, Dec. 1998. ISBN: 978-0-13-262742-9.

[113] J. K. Viljas and T. T. Heikkilä. "Electron-Phonon Heat Transfer in Monolayer and Bilayer Graphene". In: *Physical Review B* 81.24 (June 2010), p. 245404. DOI: 10.1103/PhysRevB.81.245404.

[114] Juha Voutilainen et al. "Energy relaxation in graphene and its measurement with supercurrent". In: *Physical Review B* 84.4 (2011), p. 045419.

[115] Evan D. Walsh et al. "Graphene-Based Josephson-Junction Single-Photon Detector". In: *Physical Review Applied* 8.2 (Aug. 2017), p. 024022. DOI: 10.1103/PhysRevApplied.8.024022.

[116] Albert Wandui et al. "Thermal Kinetic Inductance Detectors for Millimeter-Wave Detection". In: *Journal of Applied Physics* 128.4 (July 2020), p. 044508. ISSN: 0021-8979. DOI: 10.1063/5.0002413.

[117] Joel I.-Jan Wang et al. "Coherent Control of a Hybrid Superconducting Circuit Made with Graphene-Based van Der Waals Heterostructures". en. In: *Nature Nanotechnology* 14.2 (Feb. 2019), pp. 120–125. ISSN: 1748-3395. DOI: 10.1038/s41565-018-0329-2.

[118] Lei Wang et al. "One-dimensional electrical contact to a two-dimensional material". In: *Science* 342.6158 (2013), pp. 614–617.

[119] Xinran Wang and Yi Shi. "Fabrication techniques of graphene nanostructures". In: (2014).

[120] F. C. Wellstood, C. Urbina, and John Clarke. "Hot-Electron Effects in Metals". In: *Physical Review B* 49.9 (Mar. 1994), pp. 5942–5955. DOI: 10.1103/PhysRevB.49.5942.

[121] Gregory Wimsatt et al. "Harnessing fluctuations in thermodynamic computing via time-reversal symmetries". In: *Physical Review Research* 3.3 (2021), p. 033115.

[122] Jiamin Xue et al. "Scanning tunnelling microscopy and spectroscopy of ultra-flat graphene on hexagonal boron nitride". In: *Nature materials* 10.4 (2011), pp. 282–285.

[123] Jun Yan et al. "Dual-gated bilayer graphene hot-electron bolometer". In: *Nature nanotechnology* 7.7 (2012), pp. 472–478.

[124] Mengjian Zhu et al. "Supercurrent and multiple Andreev reflections in micrometer-long ballistic graphene Josephson junctions". In: *Nanoscale* 10.6 (2018), pp. 3020–3025.

[125] J. M. Ziman. “Principles of the theory of solids,” in: (), xiii, 435p. URL: http://caltech.tind.io/record/449619.

[126] John M Ziman. *Electrons and phonons: the theory of transport phenomena in solids*. Oxford university press, 2001.

[127] Jonas Zmuidzinas. “Superconducting microresonators: Physics and applications”. In: *Annu. Rev. Condens. Matter Phys.* 3.1 (2012), pp. 169–214.

[128] Nicholas Zobrist et al. “Wide-band parametric amplifier readout and resolution of optical microwave kinetic inductance detectors”. In: *Applied Physics Letters* 115.4 (2019), p. 042601.